Predicting the Strength of Planetary Surfaces

Thesis by
John M. Harmon

In Partial Fulfillment of the Requirements for the
Degree of
Doctor of Philosophy

CALIFORNIA INSTITUTE OF TECHNOLOGY
Pasadena, California

2022
Defended September, 13 2021

John M. Harmon
ORCID: 0000-0002-8323-3488

ACKNOWLEDGEMENTS

First, I would like to thank my professor, Prof. José Andrade for his wisdom and support throughout my time at Caltech. His direction and advice were invaluable every step of the way. He taught me many lessons academically, professionally, and philosophically that I will never forget.

A great thanks to Prof. Ares Rosakis, Prof. Ravichandran, and Prof. Chiara Daraio for serving on my committee.

I would also like to thank my adviser to my fellowship, Dr. Scott Moreland for his guidance. Beyond the help he provided, he introduced me to many people at NASA who have been critical to this work. One of those people was Dr. Morgan Cable who I would also like to thank for advising me during my internship at NASA during the summer of 2021. NASA as a whole also gets my thanks for providing me with the NSTRF fellowship that has supported me through the second half of my graduate studies.

I greatly appreciate everyone who I have been able to work closely with at Caltech (Dr. Konstantinos Karapiperis, Dr. Reid Kawamoto, Dr. Liuchi Li, Dr. Jason Marshall and Mr. Rob de Macedo), at Northwestern (Ms. Dawa Seo and Prof. Giuseppe Buscarnera), at Rio Tinto (Dr. Daniel Arthur), at JPL (Dr. Eloïse Marteau), and at PSI (Dr. Jamie Molaro) for not only making this work possible, but but also much more enjoyable.

I would like to give special thanks to Energy Vault, Inc. and specifically Dr. Andrea Pedretti and Mr. Bill Gross for providing a fascinating project that went alongside this work. Of course I'd further like to thank the team I worked with on this project beyond Prof. Andrade (Dr. Vahe Gabuchian, Prof. Ares Rosakis, Prof. Jose Restrepo, Prof. Joel Conte, Mr. Andres Rodriguez, and Dr. Arpit Nema), and specifically Vahe and Ares for our great discussions and valuable collaboration.

Prof. Kenneth Liechti and Prof. Rui Huang at UT Austin and Prof. Gabriel Candia at Universidad del Desarollo have my deep appreciation for their mentorship during my undergraduate studies and for recommending me to Caltech.

Thank you to all the MCE staff and specifically Jenni Campbell for all their help and support.

I am extremely grateful to all the friends I was and am so lucky to have through all the stages of my life. From the late night gaming with my friends from Lake Forest, to the Thursday evenings at T-Boyles, the reunions in Austin, the barbecues at the house on Sierra Bonita, the flights to Catalina, and so much more, all those great times and people have kept me at my best through this time.

Lastly, I am dedicating this work to my loving family who has shaped me as a person and have always remained close despite being so scattered across this country. Their pride and support in what I do has thoroughly motivated me in my studies.

ABSTRACT

Our curiosity and spirit for exploration has fueled advancements towards visiting Earth's neighbors in the solar system. Environments outside of Earth are extreme, however, and it is far from guaranteed that landing and operating on the surface of these bodies is an easy task. Conditions such as reduced gravity, extreme temperatures and sparse atmospheres play a role in the compressive, shear, and tensile strength of a surface. These environmental factors make experiments that work to inform design decisions for spacecraft-surface interaction difficult and expensive. In order to better ensure successful mission operations in the future, this thesis focuses on the development of a platform of numerical modeling for planetary surface interaction.

Dry regolith and water ice are two surface materials that are pervasive in the solar system. For each, the mechanical properties are heavily reliant on features at the microscale that are insufficiently modeled. The first part of the thesis will focus on crushable dry regolith. There will be two chapters on this topic, the first of which discusses the development of the modeling capability to capture both the highly irregular particle shapes and the brittle nature of regolith. The second chapter on regolith will focus on the validation of this method on a crushable sand sample experiment. This model demonstrates excellent predictive capability for the constituitive relationship, the evolution of particle sizes, and the evolution of particle shape in the sample. Further, evidence from the forces between the particles shows that despite larger particles being weaker on average, many survive due to two reasons. One, the surviving particles are generally on the stronger side of the particle strength distribution, and second, that larger particles have a higher coordination number producing a more isotropic stress state in the particle.

Unlike dry regolith, distinct neighboring water ice particles will sinter together over time at varying rates depending on their environment. This leads to a large amount of the water ice surfaces that are of interest to future missions, having a highly varied and many times unknown levels of strength. The contact interaction between water ice particles at the microscale will be handled the same as regolith, however a modification was added to account for sintering. The strong cohesiveness sintering generates is modeled by placing massless bonds where sinters would form. The cross-sectional area of the bond represents the amount of sintering that has taken place and can be thought of as a representation of the neck geometry that early

stage sintering is described as. The bonds used are linear elastic and breakable in order to capture the crushable nature of porous ice. Three chapters are dedicated to ice modeling. First, the model development will be shown with verification examples for its use. Second, the model will be used to predict cone penetration tests on ice that were previously conducted in experiment. Comparisons show that the model can produce similar stresses and qualitative features observed in the experiment. A sensitivity analysis is conducted and shows that the most important controlling parameters are the ice's critical strength and the sinter's neck thickness. The relation of the bond characteristics to the sintering process is discussed. In the third chapter on water ice, the landing of a footpad on the surface of Enceladus is modeled. The model predicts that a lack of sintering could result in catastrophic sinkage, however even moderate sintering provides enough strength to support a lander. Also the model predicts landing on inclined surfaces and shows that landing could be possible at angles as high as 20 degrees.

PUBLISHED CONTENT AND CONTRIBUTIONS

Harmon, J.M. et al. (n.d.). "Predicting the lander-surface interaction when landing on Enceladus". In: *(in preparation)*.
This work was a collaborative effort to which each author made substantial contributions in all aspects.

Harmon, J.M. et al. (2021a). "Modeling breakage mechanics of granular ice analogs for icy body spacecraft interactions". In: *Journal of Terramechanics (submitted)*.
This work was a collaborative effort to which each author made substantial contributions in all aspects.

Harmon, J.M. et al. (2021b). "Modeling connected granular media: Particle bonding within the level set discrete element method". In: *Computer Methods in Applied Mechanics and Engineering* 373, p. 113486. ISSN: 0045-7825. DOI: https://doi.org/10.1016/j.cma.2020.113486. URL: https://www.sciencedirect.com/science/article/pii/S004578252030671X.
This work was a collaborative effort to which each author made substantial contributions in all aspects.

Harmon, J.M. et al. (2021c). "Predicting contact forces and particle stresses in crushable sand". In: *Geotechnique (submitted)*.
This work was a collaborative effort to which each author made substantial contributions in all aspects.

Harmon, J.M., D. Arthur, and J.E. Andrade (2020). "Level set splitting in DEM for modeling breakage mechanics". In: *Computer Methods in Applied Mechanics and Engineering* 365, p. 112961. DOI: https://doi.org/10.1016/j.cma.2020.112961. URL: https://www.sciencedirect.com/science/article/pii/S0045782520301444.
This work was a collaborative effort to which each author made substantial contributions in all aspects.

TABLE OF CONTENTS

LIST OF ILLUSTRATIONS

LIST OF TABLES

Chapter 1

INTRODUCTION

1.1 Planetary Bearing Capacity: A Historic Problem

Up to the very moment when Apollo 11 landed on the moon, there remained a serious question about whether or not the bearing capacity of the Moon's surface could hold the Eagle lander or an astronaut. As Buzz Aldrin wrote in his memoir, "widely held was the suspicion that the Moon's surface was covered with dust so thick it would swallow a man or a spaceship like quicksand" (Aldrin et al., 1973). Many may remember that much of the transmission from Neil Armstrong when he first set foot on the Moon was focused on the surface properties, such as how deep the lander sunk, the depth and geometry of his footprint, and what the particles looked like up close (Armstrong, 1969). The worry came from the reduced gravity and dry conditions on the Moon limiting the strength and cohesiveness of the loose particles on the surface. When samples of the Moon's surface returned to Earth, we later learned that it was the unique particle size distribution and particle shapes found on the Moon that gave it much greater bearing capacity than anticipated (Heiken et al., 1991). Indeed, it was the microscale features that made the difference, but it was not for another 10 years after the landing that the most popular method, the discrete element method (DEM), for investigating the microscale of granular materials was introduced (Cundall et al., 1979), and it could still not model variable particle shape. While much has been learned over the decades since the landing, questions still remain not just for the Moon, but also for the many other bodies in the Solar System we wish to visit.

1.2 Planetary Strength Issues in the Modern Age

Although we now know that the Moon's surface is one we can safely land and walk on, similar questions plague many missions today. This includes future missions to the Moon where there are goals of larger construction projects that may test the limits of the Moon's bearing capacity (Gelino et al., n.d.). It is known that the surface particles on the Moon are quite brittle, which complicates the predictability of surface strength because the microstructure undergoes severe evolution during breakage (Heiken et al., 1991). On Mars, unknowns about the surface strength have caused recent failures, such as Insight's mole being unable to meet depth

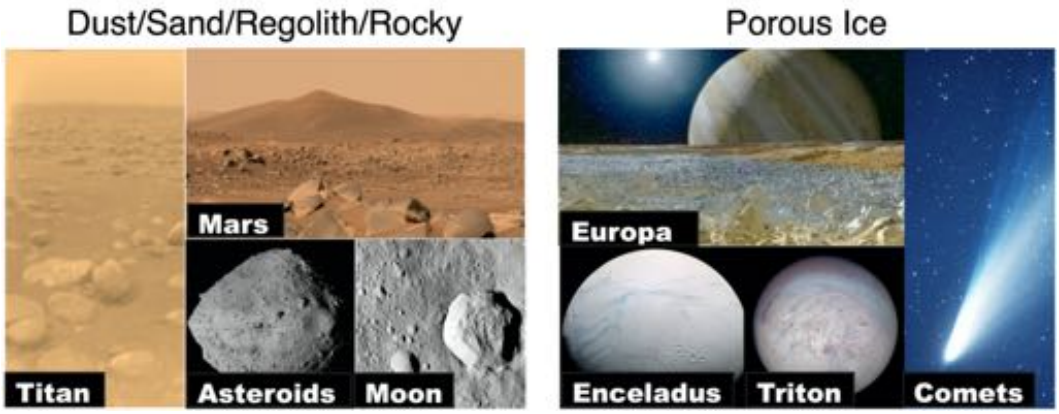

Figure 1.1: Planetary surfaces with dry, brittle granular material or porous ice are abundant in the Solar System and are frequent targets for recent and future missions. For all images credit goes to NASA/JPL.

requirements due to the surface being stronger and providing less friction than anticipated (Good et al., 2021). Also, the first rock core on Mars pulverized due to the rock being weaker than anticipated (Witze, 2021). Micro-gravity environments on smaller bodies, such as on moons and comets, have spurred research on both surface strength and sample acquisition testing to ensure sample sizes meet requirements (Riccobono et al., 2021).

Enceladus and Europa are particularly interesting targets due to their water-ice surface and geologically active core producing a relatively high likelihood for life (Chyba, 2000). The surface of icy bodies presents a unique challenge when the ice is porous due to the ability of ice particles to sinter over time, creating large changes in strength (Choukroun et al., 2020). The ice on these bodies can be thought of as a connected granular material where individual ice particles are connected through sintering (Molaro et al., 2019). This type of ice is far from uncommon in the solar system. For example, on Enceladus the plumes on the south pole eject ice particles that deposit on the surface and sinter over time (Verbiscer et al., 2018). A highly porous but cohesive granular microstructure exists due to the low sintering rates. On Europa and Triton, recent image analysis points to a high probability of porous granular ice (Eluszkiewicz, 1991; Carlson et al., 2009). Many smaller bodies have a mixture of ice and regolith, which can result in similar densification to pure ice (Campins et al., 2010). Without understanding how the strength of the ice surface changes with sintering, designing missions to these bodies appropriately will be exceedingly difficult.

The common thread between all of the mentioned surfaces is that at the micro-scale, the morphology is complex and significant breakage is a possibility. Key to the design and understanding of these surfaces for the purposes of interaction will be in predictions that capture these strength changing properties of the micro-scale effectively.

1.3 Research Objectives

The objective of this thesis is to further the state of the art of granular modeling in order to capture the unique features found on planetary surfaces. There will be two types of surfaces that will be focused on: first, a dry regolith surface and second, a porous ice surface, which, between the two, compose a large majority of the scientific targets of interest. Dry regolith surfaces require a model to take into account irregular shaped particles that are brittle. While it is already possible to model particles of arbitrary shape, in this thesis this method will be extended to enable those particles to be breakable. For surfaces composed of porous ice, the model will instead be extended to take into account the stiff sinters that grow in between ice particles. We will utilize an assumption that at a critical load the sinters will be first to break because they are generally thin sections of the microstructure. Due to this assumption, the sinters modeled will be breakable instead of the particles themselves.

1.4 Approach

Grain-scale Modeling

The study of granular materials occurs at many scales that are often categorized as the macro-scale, meso-scale, and the micro/grain-scale. At the macro-scale, granular materials act like a continuum that can generally be seen as a single solid object, but can also be seen as a fluid such as in the case of landslides. At the meso-scale, groups of particles form representative volume elements (RVE) that are meant to be large enough to still satisfy the continuum assumption. However at this scale, some ideas of the state of the grain-scale come into play to be able to bridge the two scales in between. The fundamental science of granular materials, however, occurs at the grain scale where individual grains can be identified. At this scale, macroscopic stresses result in interparticle forces that unevenly divide into force chains. The number, magnitude, orientation, and evolution of these force chains dictate the constitutive behavior of a granular material, making granular materials inherently non-local (Celigueta et al., 2017). Factors such as particle shape, size,

and strength play a critical role in the nature of force chains and, therefore, must be captured in modeling at this scale in order to correctly inform the larger scales.

DEM is extremely popular for modeling the grain scale because it provides an efficient way of calculating the forces and kinematics of individual particles. Originally, DEM was designed with only circles and spheres for particle shapes (Cundall et al., 1979). However, over time many innovations have allowed for more complex shapes to be captured (Mollon et al., 2014; Zhu et al., 2019). The level set variant (LSDEM) is the only one of these that can capture any arbitrary shape, therefore it is the one that will be utilized throughout this thesis (Kawamoto et al., 2016).

Level Set Discrete Element Method

Summaries of LSDEM are given repeatedly throughout this thesis, specifically in one of the upcoming sections, 2.3, and later, in greater detail, in 4.3 therefore it will not be given here as well. For the purpose of introduction, it is important to understand the intent behind the method. LSDEM provides the ability to geometrically describe any particle shape through an implicit definition, which enables full functionality for studying the effects of particle shape (Kawamoto et al., 2018a), in addition to the micro mechanics that the other DEM methods provide. Any shape can be fully described, and it also can be naturally paired with x-ray imaging, which provides the shapes and locations of a granular specimen. In this way, the method can be directly validated, and individual properties can be properly investigated. Because the model is considered predictive, there is confidence in the statistics of the interparticle forces that are calculated in the model. These can be utilized to learn about the kinetics (Karapiperis et al., 2020b). This is very important because experiments on natural granular materials cannot measure the forces between particles. Therefore we must rely on methods like LSDEM to study the key mechanism behind granular mechanics.

XRCT Imaging and Level Set Conversion

On the experimental side of grain scale science, granular assemblies often are imaged using X-ray computed tomographic (XRCT) scans (Andò et al., 2012; Karatza et al., 2019). These scans construct 3D images from thousands of x-ray images taken of a specimen on a rotating platform. The resulting image is required to have voxel sizes on the order of geometric features of the particles, usually on the order of micrometers for commonly used sands, such as Hostun and Ottawa sand. For any given loading, scans are taken at multiple steps to properly capture the full process.

However for the purposes of level set production for computation, only the initial image is used.

Once images are taken, some type of watershedding procedure is performed in order to distinguish and label particles. In the case of studying breakage, particles must be also tracked from parent particles to child particles by comparing successive images (Seo et al., 2020). Level sets can then be made using LS-imaging from the watershed and edge markers defined from the image gradient. LS-imaging uses an energy functional that minimizes when the distance of the discrete level set function to the edge markers are zero (Vlahinić et al., 2014). When the LS-imaging process is finished, the surface of the discrete level set and the surface on the image coincide. The final step is to produce a surface discretization of each particle to enable the leader-follower algorithm for the method. Figure 1.2 visualizes the process from raw image to watershed to level sets.

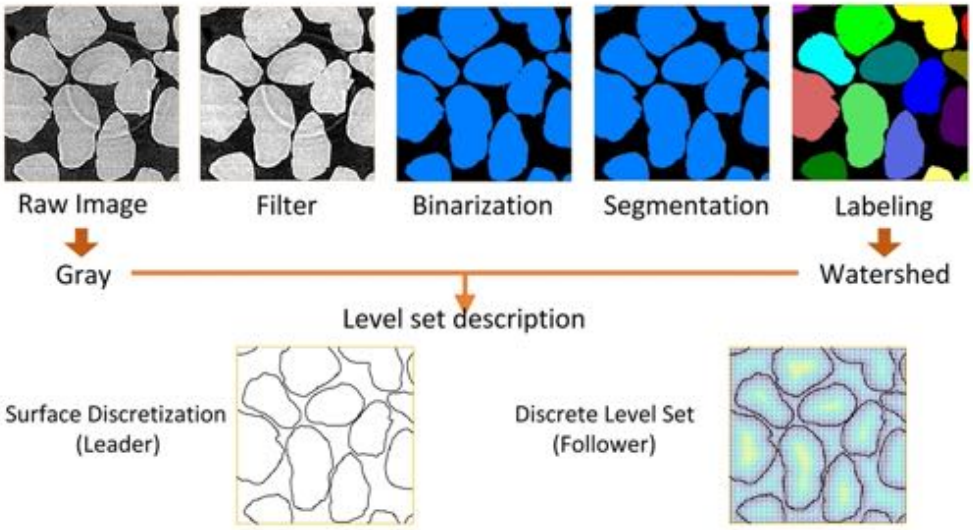

Figure 1.2: XRCT images are processed into a watershed to distinguish individual particles. From here, level sets can be made from creating an energy potential that minimizes at the surface. The level set evolution algorithm becomes stationary at the minimum energy contour.

1.5 Organization

This thesis will be organized by first addressing the modeling of brittle, arbitrarily shaped material. Then, there will be a chapter on the validation of many features of the model through direct comparison to experiment with further investigation into the science of breakage. The focus will then shift in Chapter 4 towards porous ice

modeling. Similarly to the regolith modeling, first the model will be introduced, then in the next chapter, the model will be compared to an experiment. In Chapter 6, we will then go beyond validation and model the landing process on the Enceladus surface investigating the limitations of landing selection. Finally, there is a conclusion chapter where a summary of results and discussion for future work can be found.

Chapter 2

LEVEL SET SPLITTING IN DEM FOR MODELING BREAKAGE MECHANICS

Harmon, J.M., D. Arthur, and J.E. Andrade (2020). "Level set splitting in DEM for modeling breakage mechanics". In: *Computer Methods in Applied Mechanics and Engineering* 365, p. 112961. DOI: https://doi.org/10.1016/j.cma.2020.112961. URL: https://www.sciencedirect.com/science/article/pii/S0045782520301444.

2.1 Abstract

Brittle breakage of particles in granular materials has often been modeled using the discrete element method (DEM). DEM is often limited however in its ability to capture particle shape, particularly when used for breakage. This paper presents the first brittle breakage technique where level set functions will allow for the description of the arbitrary shape for both particles and fracture surfaces. The breakage model to be described here uses fracture surfaces defined by level sets to take advantage of simple intersection and difference set operations to split particles in both two and three dimensions. We show how this method is implemented and how we can use it to define and apply arbitrary fracture surface shapes. We then give qualitative examples of using the method in both simple and exotic ways. Finally, we model oedometric tests and rock crushing, both very common uses for previous DEM breakage techniques, to present a validation that the method captures the physics of the problem.

2.2 Introduction

Understanding the mechanics and effects of particle breakage is important in many applications. In geomechanics, particle breakage produces a new particle size distribution (PSD) which will affect strength and dilantancy among other properties (Minh et al., 2013; Holtz et al., 1981). Fault zones in earthquakes are home to a large amount of fractured rocks in which the PSD has large effects on the physical attributes on the fault core (Billi, 2005). Recent continuum models will include breakage as a parameter, which opens the possiblity of bridging the grain scale and continuum scale if a grain scale method can reasonably simulate enough grains

(Einav, 2007). Also instead of looking at how particle breakage affects larger scales, one could also look at how a single particle fully comminutes. This has applications in mining, where crushing iron ore is necessary in the process to extract iron (Evans, 1993). This also has applications in lithotripsy, where the goal is to comminute a single kidney stone as much as possible(Sapozhnikov et al., 2007).

Discrete Element Modeling (DEM) has been a popular numerical method for studying breakage. DEM is a method first developed by Cundall & Strack (Cundall et al., 1979) which has been widely used to study granular materials. Implementing particle breakage in the classical DEM, where each particle is a sphere, has been done in two ways. The first is by having each particle made of many smaller particles bonded together (Cil et al., 2014; Cheng et al., 2003; Wang et al., 2013; Potyondy et al., 2004). When the forces acting between two smaller particles exceed the strength of the bond, then the bond is considered fractured and therefore removed. The benefits of this method is that an initial clump of particles can be arranged to take a non-spherical shape and the fracture will preserve mass. The drawbacks are that the increased amount of particles increases computation time and even with an extremely large amount of smaller particles, the larger particle will always differ from a physical one. The other method replaces a particle when it reaches a certain stress level with many smaller particles (Ben-Nun et al., 2010; McDowell et al., 2013). This method is much quicker computationally, but has issues with mass conservation, replicating a realistic fracture pattern, and choosing how many particles to replace a larger one with. Both sphere-based methods mainly suffer from an inability to model particle shape correctly, which in recent literature has shown to have an impact on which grains carry the deviatoric stresses (Kawamoto et al., 2018a). Since it is the stresses on the particle that drive when and how particles break, it is critical to have a method that describes particle shape exactly.

This has been approached by creating and solving a finite element mesh for every particle (Imseeh et al., 2018; Iliev et al., 2019), a good solution for granular systems with small numbers of particles. For larger systems, polyhedral elements have been used. Originally done by Potapov and Campbell (Potapov et al., 1996), this was originally quite slow so this method was modified to be suitable for large scale simulations (Herbst et al., 2004). The improved method has not been able to fit both single particle breakage and particle size distributions though due to an energy-based approach instead of a stress-based one (Jiménez-Herrera et al., 2018). More recent developments have moved to a stress based approach and increased efficiency using

ideas such as implementing a hybrid peridynamcis and physics engine approach(Zhu et al., 2019). Despite these advancements, polyhedral methods still have difficulty working with geometrical concavity in particles. Since it should always be expected that particles will have local concave features, these methods are not fully ideal.

A version of DEM that can handle non-convex particles uses Fourier descriptors to describe shape (Mollon et al., 2014). Fourier descriptors can effectively describe any particle of a "star" shape, which is suitable for most granular materials. As far as we have seen, there is no breakage method for this DEM version yet.

In this paper, we will build a breakage model from the level set DEM (LS-DEM) (Kawamoto et al., 2016). This method has the powerful capability to capture exact shape without limitations while maintaining reasonable computational efficiency. LS-DEM has the profound advantage of capturing morphology from X-Ray Computed Tomography (XRCT) (Vlahinić et al., 2014) and has been shown to be able to make one-to-one predictions at the micro-scale (Kawamoto et al., 2018b). So in the following sections we will describe the first LS-DEM breakage method. We will first show how splitting level sets can be done in both two and three dimensions. Then we will show an industrial example of how level set splitting in LS-DEM can predict the performance of crushing machines. Finally, we will show an example of the method's capability in geomechanics from comparisons with oedometric experiments on a granular specimen,with a small study of breakage criteria.

2.3 LS-DEM

LS-DEM, originally introduced in (Kawamoto et al., 2016), is a DEM variant that fully captures the shape of every particle unlike the classical DEM where only spheres are used. LS-DEM utilizes level set functions for defining each particle geometry. Level set functions define a surface implicitly by having the function value at every point be equal to the signed distance to the object surface; a negative level set value means the point is inside the object, a positive value is for outside the object, and a zero value is for locations on the surface.

In implementation, particles of dimension D are geometrically defined by using both a discrete level set, ϕ,

$$\phi(\mathbf{x}) = \pm d \tag{2.1}$$

where d is the signed distance from the surface of the particle, and a set of surface points, P,

$$P = \{\mathbf{p} \in \mathbb{R}^D | \phi(\mathbf{p}) = 0\} \tag{2.2}$$

as shown in Figure 2.1. This method of contact results in efficiency being largely based on surface point discretization density since each point must be checked with either the level set of each other particle or the radius of its bounding sphere. The discretization of the level set has no effect on efficiency outside of a finer grid taking more memory to store.

To find contact, for instance between particle g_1 and particle g_2, we take the surface points of g_1 and check the level set value on g_2 of each surface point. If the following inequality holds for any surface point, $\mathbf{p}_i \in P_1$, on the first particle,

$$\phi_2(\mathbf{p}_i) < 0 \tag{2.3}$$

then contact is established and the overlap is known from the evaluation of $\phi_2(\mathbf{p}_i)$. Furthermore, the contact normal is calculated easily from the gradient of the level set,

$$\hat{\mathbf{n}} = \nabla\phi_2(\mathbf{p}_i) \tag{2.4}$$

With the overlap and contact normal, contact forces and moments can be determined from a contact law. No contact law is specific to LS-DEM; in this study, a linear model is used. The Hertzian contact law could also be used (Johnson et al., 1987). The frictional forces are computed using Coulomb friction. These forces and moments are then integrated to get displacements and rotations for each time step. Either contact dynamics, (Jean, 1999) or an explicit scheme, (Walton et al., 1993; Lim et al., 2014) could be used for integration, and in this paper, the explicit scheme is chosen. The displacements and rotations are then applied to the surfaces points, and the process iterates.

2.4 Description of Breakage Model

The breakage model described here is composed of two parts. The first part is the fracture criterion, which determines when a particle will break. This part is not specific to the method and can easily be changed as will be discussed. The second part is the level set splitting method, which determines how a particle will break. This method was built with the assumption that the particles which compose the granular material are brittle. Namely, that the speed of crack propagation is on a much smaller time scale than the loading. With this assumption in mind, it is sensible to build a method that breaks a particle into two or more pieces instantly, or in implementation, a single time step. This can save a significant amount of computation time that would otherwise be used for crack tracking, determining

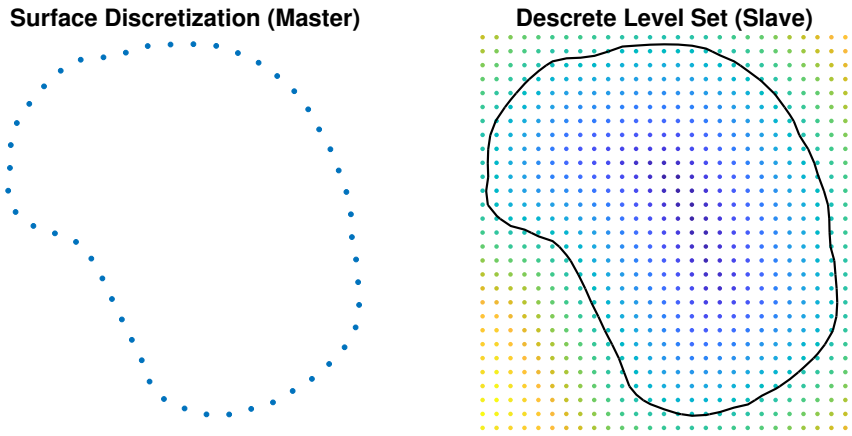

Figure 2.1: Particle geometrical description. Left: A set of points that all lie on the particle surface. Right: A discrete color map where cooler colors are negative and warmer colors are positive. The black line is the zero contour line found with interpolation. The surface points of the master particle are mapped to the slave particle's level set to determine contact.

crack speed or resolving stress around a crack tip, allowing a user to model systems with very large numbers of breakages.

Breakage Criterion

A natural way to determine when a particle should break is by evaluating the stress inside the particle. This can be done by solving the distribution of stresses in a particle (Imseeh et al., 2018) however this method can be very inefficient. Alternatively, the average stress inside the particle, $\bar{\boldsymbol{\sigma}}^p$ can be calculated from knowledge of the contact forces, $\mathbf{F}_c$, and branch vectors, $\mathbf{x}_c$, over a certain number of contacts on the particle, N,

$$\bar{\boldsymbol{\sigma}}^p = \frac{1}{V_p} \sum_{c=1}^{N} \boldsymbol{x}_c \otimes \boldsymbol{F}_c \tag{2.5}$$

where V_p is the volume of the particle. From here, it is very convenient to find the principal stresses, σ_p, by finding the eigenvalues of $\bar{\boldsymbol{\sigma}}^p$.

$$(\bar{\boldsymbol{\sigma}}^p - \sigma_p \mathbf{I})\hat{\mathbf{n}} = 0 \tag{2.6}$$

Using the principal stresses, we can then choose a stress-based yield criterion. As mentioned before, the yield criterion is a flexible choice, therefore in this paper three separate yield criterions will be used. Here we will use the maximum pricipal

stress, von Mises criterion, and the Tresca criterion for breakage, however other DEM breakage models have also used a shifted Tresca criterion (Iliev et al., 2019) which could certainly be substituted given considerations for the material being modeled.

The maximum principal stress criterion assumes that the particle will break when the principal stresses reach a critical value. For this criterion, we will assume this could be in either compression or tension. Since most granular materials are much stronger in compression than tension, there will be two critical values for this criterion.

$$\sigma_C^{max} > \sigma_C = min(\sigma_{p1}, \sigma_{p2}, \sigma_{p3}) \tag{2.7}$$

$$\sigma_T^{max} > \sigma_T = max(\sigma_{p1}, \sigma_{p2}, \sigma_{p3}) \tag{2.8}$$

where σ_C and σ_T are the maximum compressive and tensile stresses, respectively.

The von Mises yield criterion is expressed as follows,

$$\sigma_{Vmax} > \sigma_V = \sqrt{\frac{1}{2}[(\sigma_1 - \sigma_2)^2 + (\sigma_2 - \sigma_3)^2 + (\sigma_3 - \sigma_1)^2} \tag{2.9}$$

where σ_{Vmax} is the maximum allowed value of the average von Mises stress inside a particle, σ_V.

The Tresca yield criterion is based on the shear stresses in the material

$$\frac{1}{2}\sigma_C^{max} > \tau = \frac{1}{2}max(|\sigma_1 - \sigma_2|, |\sigma_2 - \sigma_3|, |\sigma_3 - \sigma_1|) \tag{2.10}$$

where τ is the maximum shear stress at any one stress state. Figure 2.2 shows a graphical depiction of the yield surfaces from these criterions. The units are set to be the stress values for the oedometer test in section 5 of this paper.

When the average critical stress of any particle exceeds the threshold set by the chosen criterion, then the particle will be broken. The value of the critical stress is determined by both the material and the size of the particle, as according to Weibull's theory (Weibull, 1939), the probability of failure is given by

$$P_f(\sigma^c \geq \sigma^{max}) = 1 - exp\left\{-\left(\frac{d}{d_0}\right)^3 \left(\frac{\sigma^c}{\sigma_0}\right)^m\right\} \tag{2.11}$$

where d and σ^c are the diameter and the chosen breakage criterion's characteristic stress for any given particle, and d_0 and σ_0 are a reference diameter and strength.

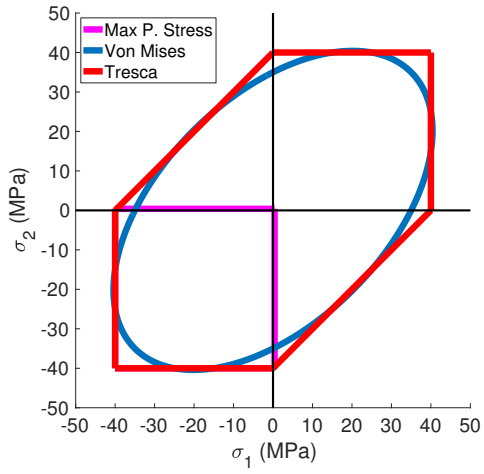

Figure 2.2: Yield surfaces used in this paper.

The variable m is Weibull's modulus which is a material parameter. In this paper, a typical Weibull's modulus of 3 was used throughout (McDowell, 2002). To be able to seed true critical stress values, we need to invert and solve for σ^c.

$$\sigma^c = \sigma_0 \left\{ -\left(\frac{d_0}{d}\right)^3 ln(1 - P_f) \right\}^{m^{-1}} \tag{2.12}$$

Now by using inverse transform sampling, we can seed critical stress values by taking values of P_f from a uniform distribution, $U(0, 1)$.

As particles break into smaller fragments, breakages tend to be along the largest flaws in a given particle. Therefore as particles comminute, they will become stronger which is an effect that must be represented in modeling. To continue to account for particle size in our breakage criterion, we refer to Weibull statistics and experiments performed by Nakata et al. (F. L. Nakata et al., 1999) that show the following relation between a child particle, a, and a parent particle, b,

$$\frac{\sigma_a^{max}}{\sigma_b^{max}} = \left(\frac{d_a}{d_b}\right)^{-3/m} \tag{2.13}$$

Level Set Splitting

Splitting particles in LS-DEM can be done in either two or three dimensions, and have a similar process for each. To split a level set, ϕ_1, we first must make a separate level set object that defines the fracture surface we want to apply, ϕ_2. The fracture level set surface must extend to the boundary at all end points, allowing one side of the surface to have negative values and the other to have positive values. These

fracture surface level sets can be made in a wide variety of ways. Some methods of creation could be: level set imaging from XRCT just like grains of sand in previous uses of LS-DEM (Vlahinić et al., 2014), utilizing stress distribution information that could be solved on the particle (Jiang et al., 2019), or from assumptions on what the fracture might look like based on contact forces and/or particle shape.

The two new grains will be created by doing the intersection and difference set operations between ϕ_1 and ϕ_2.

$$\phi_3 = \phi_1 \setminus \phi_2 = max(\phi_1, -\phi_2) \tag{2.14}$$

$$\phi_4 = \phi_1 \cap \phi_2 = max(\phi_1, \phi_2) \tag{2.15}$$

This process is depicted in Figure 2.3 for both a 2D and 3D grains. Note that both surfaces can have large numbers of convexities and concavities and that every feature that intersects the particle is shown in the fragments. The part of fracture surfaces that extend past $\phi_1(\mathbf{x}) = 0$ can be arbitrary.

Since the new particle surfaces defined by ϕ_3 and ϕ_4 are made by set operations, the union operator could also be used to bring back the original particle,

$$\phi_3 \cup \phi_4 = min(\phi_3, \phi_4) = \phi_1 \tag{2.16}$$

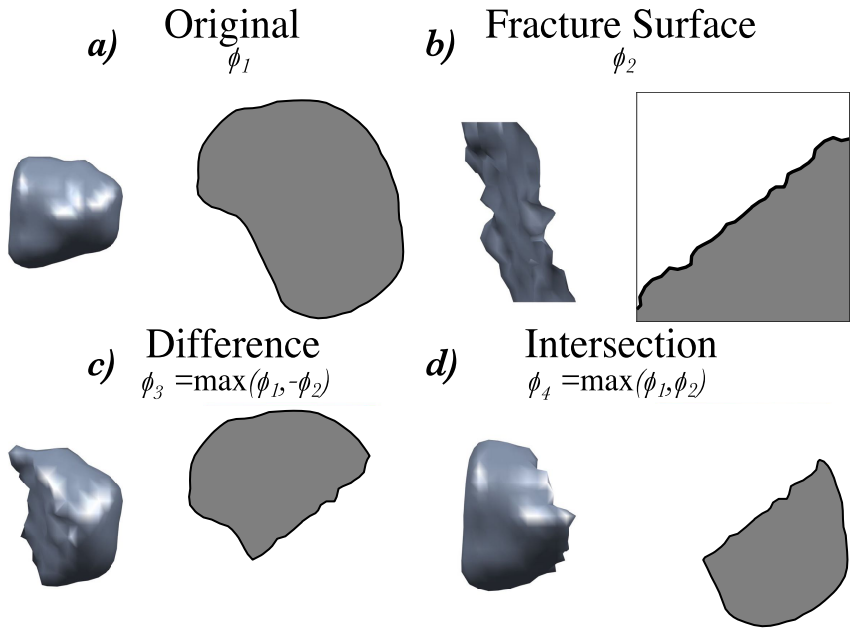

Figure 2.3: Level set surfaces in 2D and 3D for a pre-split sand grain (top left), breakage surface (top right), and two fragments (bottom left and right).

The intersection and difference set operations can produce error on the outside region of each fragments' level set, or specifically where $\phi > 0$. These errors come from the set of kept distance values that refer to a surface that was removed during the set operation. Due to LS-DEM only being interested in the level set values inside the particle, this issue can be safely ignored for most cases. The accuracy of the outer portions could be important if we wanted to add cohesion or a bonding method though. In this case, these errors can be removed with a couple time steps of the reinialization equation which was first described in (Sussman et al., 1994),

$$\phi_t = sign(\phi_0)(1 - |\nabla\phi|) \tag{2.17}$$

The reinitialization equation keeps the object surface stationary and converges when the level set returns to being a signed distance function at all points. After reinitialization, the particle is ready for use for all purposes. In Figure 2.4, a heat map of the errors is shown for ϕ_1 after being split by a straight line. The error is calculated from the difference in the discrete level set values from the broken particle before and after reinitialization. The dots on the figure depict the discrete border where the set operation stops taking values from the original particle (red dots) and starts taking values from the fracture surface (white dots). It can be easily seen that errors are localized to areas outside of the resulting particle. Since no cohesion was necessary for any application in this paper, Equation (2.17) is not used.

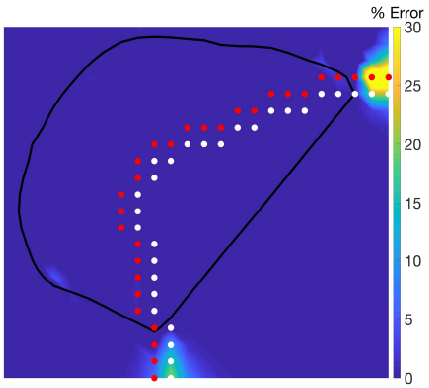

Figure 2.4: Heat map of the error produced from set operations. Dots on figure show the discrete border between the max function picking particle values (red) or fracture surface values (white).

Determining Fracture Path

While it is possible to use any arbitrary fracture surface that could be derived from either experiment or statistical methods, the simplest way to implement level

set splitting into LS-DEM and the way it will be done in this paper is to only use flat breakages such as lines in 2D and planes in 3D. These breakages can be oriented in any way by defining the line or plane by two or three points, respectively. Experiments have shown that granular fracture surfaces are highly likely to connect between the contact forces acting on a grain (Cil et al., 2012; Hurley et al., 2018). So for the case of 2D, we choose the two points to complete the line by taking the location of the two highest contact forces. From here, the level set can be easily built from the well known point to line distance formula,

$$\phi(x, y) = \frac{(y_2 - y_1)x - (x_2 - x_1)y + x_2 y_1 - y_2 x_1}{\sqrt{(y_2 - y_1)^2 + (x_2 - x_1)^2}} \tag{2.18}$$

where the locations of the contact points are given as (x_1, y_1) and (x_2, y_2).

Similarly in 3D, we choose the locations of the three highest contact forces to determine the breakage plane. With these locations determined from contact, the resulting level sets can be calculated from,

$$\phi(\mathbf{x}) = \frac{\mathbf{n} \cdot \mathbf{x} - \mathbf{n} \cdot \mathbf{p}_1}{||\mathbf{n}||} \tag{2.19}$$

where

$$\mathbf{n} = (\mathbf{p}_2 - \mathbf{p}_1) \times (\mathbf{p}_3 - \mathbf{p}_1) \tag{2.20}$$

and $\mathbf{p}_1$, $\mathbf{p}_2$, and $\mathbf{p}_3$ are the three points that define the plane. For both two or three dimensions, there are occasionally cases where only one or two forces cause enough stress to break a particle which would not create enough contact points to complete a line or plane. For these cases, the particle centroid was used as another point for breakage. In the case that there is only one contact point for a 3D particle, breakage was held off until a second contact point was encountered. If there are multiple points of contact for a single contact pair, such as right after a breakage with line-to-line and plane-to-plane contact, only the point of contact contributing the highest force will be used for fracture path determination.

To build the surface points, generally a marching squares method or an energy minimization method is used. In the case of building flat fracture surfaces, this can be greatly simplified by utilizing the known vectors that define the line or plane and placing points at equidistant values along the tangent vector directions. From here, we determine what surface points from the original particle and the fracture surface go to which fragment. This is done by comparing surface points to the level sets. For example, if the locations of surface points on the fracture surface are in the

negative region of the original particle's level set, then we keep those points since these will be on the surface of both fragments. Similarly, we check the location of each surface point on the original particle against the fracture path level set to determine which fragment that surface point should be assigned to.

During fragmentation, the physical properties of the new particles must also be determined, namely the mass, moment of inertia, and center of mass. This is done using just the level set matrix in the same way as when producing particles from tomography. A full explanation for how to calculate these properties are both in (Kawamoto et al., 2016) and in the Appendix.

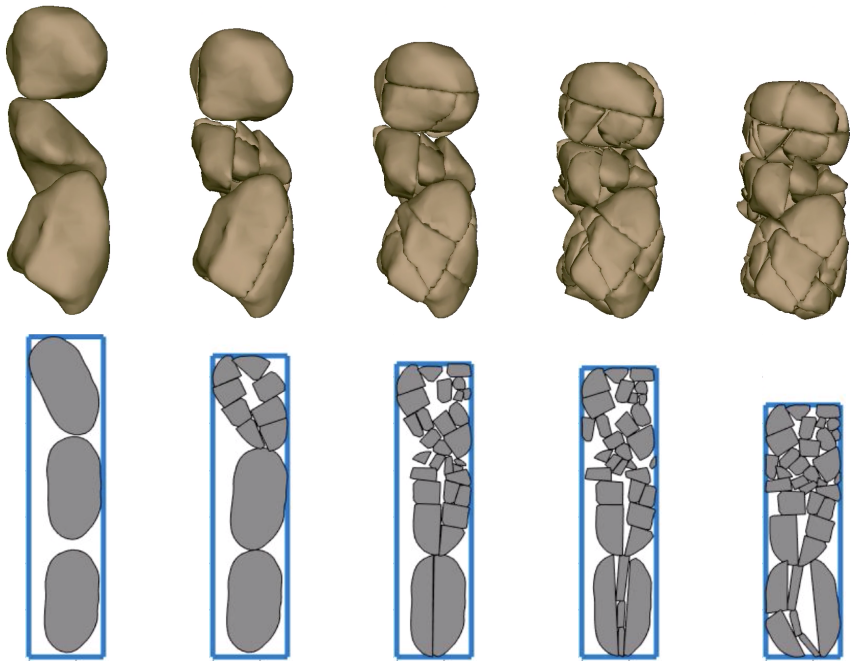

Figure 2.5: A simple three particle example for level set splitting for both 3D (top) and 2D (bottom).

Qualitative Testing

Before applying the model to applications for validation, we first went through a round of qualitative testing. The first of these was producing the breakage of three grains vertically aligned in compression shown in Figure 2.5. This was conducted both in 2D and 3D on particles of Hostun sand taken from 3D XRCT. The DEM parameters were set to produce breakages easily in order to test the stability of small particles. It was here that it was found that when particles become small enough to be of similar size to the surface point discretization, then they can be a source of significant instability. We had three methods to address this issue. First method

is to halt breakage when particles reach a minimum size. The second method is to adaptively increase discretization of the particles throughout comminution. The final method was to remove particles that were small enough to be problematic. All three of these methods were tested in the two quantitative studies described in the following sections. The first method was unable to produce good results against experiment for predicting PSD since the smaller sizes were unreachable by definition. It is likely that this method would be a good one if the particles were given a finer discretization since the limiting factor was often the surface point discretization density. The later two methods both produced similar results, so the final method was used throughout due to its added efficiency. Removed particles were stored in output and were counted in producing the PSD data. For all simulations, it was ensured that the total mass of the filtered particles were $< 1\%$ of the total mass of the specimen.

It is also of note that after some qualitative analysis of this method, it was found that occasionally a seemingly unrealistic amount of thin grains were produced, particularly in 2D. To remedy thi,s we also added what was termed a "buckling" breakage mode. The buckling mode occurs if the volume of the circumscribed circle or sphere around the particle is much larger than the volume of the particle itself. If a calibrated ratio between the circumscribed sphere's volume to the particle volume was reached, then the particle would be cut along its closest surface. So in this case, the breakage line would be determined from the centroid and the closest surface point, p_{min}, from the set of surface points for each particle, P_p,

$$p_{min} = min(P_p) \tag{2.21}$$

which would define the fracture line in 2D. In 3D, we took a random point to complete the plane with the centroid and p_{min}. This was not used in later testing with experiment since it did not produce good results, an explanation for this will be given in Section 5.1. So while this was used during qualitative tests, it was not used in any other part of the paper.

For the next qualitative test, we wanted to look at a more dynamic setting that clearly demonstrates an ability that no other DEM breakage model could produce in a practical way. For this, we took the fact that the ability of level sets to take arbitrary shape is a unique and powerful ability within the context of DEM. There are many applications, particularly in breakage mechanics, where extremely complex shapes may need to be used. A good example of this is in building demolition, where

both the wall and the demolition machine have shapes that are very different than any granular particle. We take advantage of the geometrical versatility of using a level set based method to show an example of how this method could be used for demolition.

The setup consisted of creating both a wall and excavator buckets in AutoCAD and then converting each into level sets through a point-to-triangulation distance function. The bucket trajectories were then defined so that there would be two instances of crushing the wall. For each instance of wall crushing, the first break was manually determined in order for the breakage method to not choose the centroid of the wall as a point on the breakage plane. All subsequent breakages were done by using the flat level set splitting breakage method described earlier. The final product of this is a video where five representative frames at different phases of the demotion are shown in Figure 2.6. This simulation demonstrates that level set splitting in DEM can be used in many applications beyond the typical uses for DEM in granular mechanics.

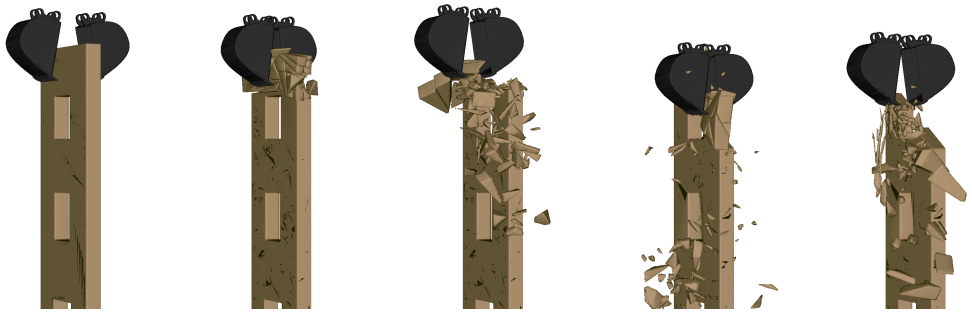

Figure 2.6: Visualization of wall demolition using two excavator buckets. Simulation time runs from left to right.

2.5 Jaw Crusher Simulations

Jaw Crusher Setup

DEM has been a popular method for simulating rock crushing for mining applications (Weerasekara et al., 2013). One of the simplest crushers is the jaw crusher which will be used as an example in this section. The jaw crusher uses two plates to comminute rocks by compressing the plates together repeatedly. As shown in Figure 2.7a, these plates are either vertical or near vertical and taper to create a much smaller opening at the bottom than at the top. In all jaw crushers, there is a stationary plate and a swing plate. The swing plate can be set to have specific opening sizes, RPMs, and other adjustable settings depending on how it is manufactured.

(a) TST Jaw crusher made by FLSmidth.

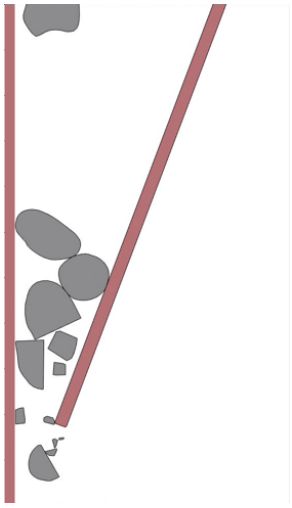

(b) Visualization of a 2D jaw crusher in operation.

Figure 2.7: Jaw crushers.

The jaw crusher simulations were built to mimic the jaw crusher used in a study by Johansson et al. Johansson et al., 2017. The table below shows the three crusher-specific settings that we looked to mimic. The first is the rotational speed of the wheel that drives the compression of the plates. One rotation of the wheel corresponds to one cycle of compression and extension. The second is the average angle between the stationary plate and swing plate which is called the nip angle. The swing plate will tilt slightly during operation. In our simulations, the angle varied $\approx \pm 1.7$ degrees each rotation. The third is the eccentric throw, which is the distance between the open side setting (OSS) and the closed side setting (CSS), the OSS being the widest opening between the bottom of the plates and the CSS being the smallest opening over a cycle.

This jaw crusher simulation will be done in 2D with two rectangles defined by level sets representing the jaw crusher. The rock shapes used were cross sections of Hostun sand from XRCT images scaled to the size of rock. A total of 25 unique particle shapes were used and dropped in order so that the twenty-sixth particle that was dropped was the same as the first particle. The feed for the jaw crusher was done by dropping rocks into the crusher from a specified position once the last rock had completely cleared the space. Figure 2.7b shows a visualization of the jaw crusher during a simulation. The particle on the upper left shows where the particles are spawned, and particles were sent to output once they left the frame of the image. Simulation parameters were set to resemble typical values for rock and shown in

Parameter	Value	Units	Jaw Crusher Setting	Value	Units
k_n	$3*10^7$	N/m	RPM	300	rot/min
k_s	$0.8*k_n$	N/m	Nip Angle	22	deg
μ	0.6	none	Nip Angle Change	± 1.7	deg
ρ	2650	kg/m^3	Eccentric Throw	50	mm
Δt	$1.8*10^{-6}$	sec	k_n	$3*10^7$	N/m
Global Damping (C_g)	0	$(\text{sec})^{-1}$	k_s	$0.8*k_n$	N/m
Contact Damping (C_{res})	0.4	none	μ	0.6	none
Level Set Resolution	7	mm/pix			
Weibull's Modulus (m)	3	none			
Critical Strength	56.5	MPa			
Characteristic Diameter	0.21	m			
Surface Point Discretization Density	2	pts/pix			

Table 2.1: Parameters for jaw crusher testing.

Table 2.1. For these simulations, only the von Mises criterion was used. Studying the effect of using this criterion versus the Tresca and Maximum Principal Stress will be done in the next section on oedometer testing.

Jaw Crusher Results

There were three total simulations analyzed for comparison. The closed side setting (CSS) was varied from 50 mm, to 80 mm, and then to 100 mm while all other parameters, including calibrated material parameters, were kept constant. Each simulation was run over forty jaw crusher cycles. The total amount of particles analyzed as output were 336, 397, and 233 for the 50mm, 80mm, and the 100mm CSS test, respectively. At the end of each simulation, the PSD was determined for the collection of particles that had completely passed through the crusher. Sieve size was determined through an approximation of the minor axis of the particle. We calculated this by finding the diameter along the line connecting the centroid and the closest surface point, p_{min}, from Equation (2.21). We then took manufacturer results for output PSD given in (Johansson et al., 2017) and compared them to our simulation in Figure 2.8. Results match well for all three comparisons across sieve sizes, which means this modeling strategy can be predictive for applications where output PSD is a key factor.

Although not done here, other important predictions for jaw crushers can be performed using this strategy such as capacity, flow rate, power draw, and effects of different jaw crusher settings. Other crushers besides the jaw crusher could also be

modeled easily since level sets can be built from the CAD models used to design crushers.

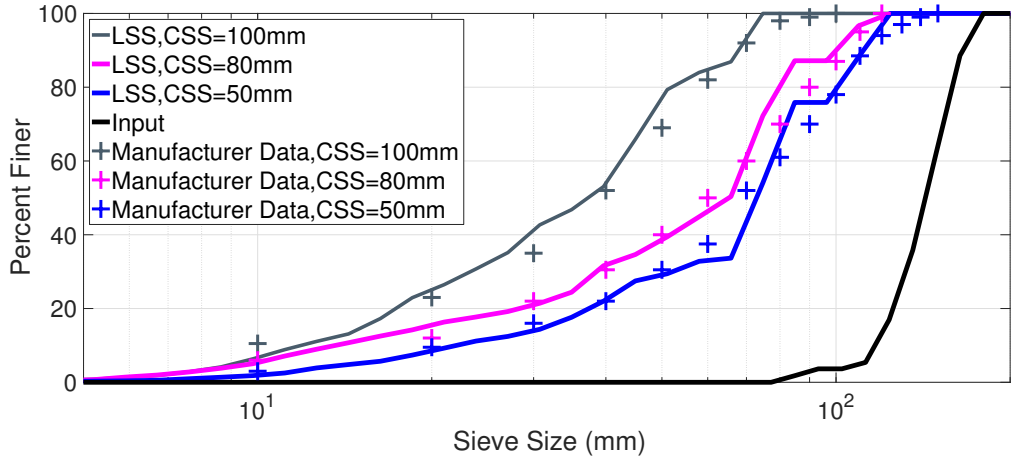

Figure 2.8: PSD of the jaw crusher output from both the level set splitting method as well as from experiment. Manufacturer data adapted from (Johansson et al., 2017).

2.6 Oedometric Testing

Oedometer tests have been a common way to investigate the effect of crushing in a granular sample (Atkinson, 2007). These tests are conducted by compressing the specimen from the top, usually in displacement control, while maintaining rigid walls around the specimen. Due to the rigidity of the boundaries, the specimen must have breakages to better fill the constantly decreasing void space. To further validate our model quantitatively, we conducted an oedometric test on a set of grains in 2D and compared the results to experimental testing in the literature.

Parameter	Value	Units	Parameter	Value	Units
k_n	$4*10^7$	N/m	Weibull's Modulus (m)	3	none
k_s	$0.6*k_n$	N/m	Max Compressive Stress	40	MPa
μ	0.4	none	Max Tensile Stress	0.4	MPa
ρ	2450	kg/m^3	Max Von Mises Stress	35	MPa
Δt	$2.2*10^{-7}$	sec	Max Shear Stress	40	MPa
Global Damping (C_g)	$0.01/\Delta t$	(sec)$^{-1}$	Minimum Area	0.05	mm^2
Contact Damping (C_{res})	0.4	none	Characteristic Diameter (d_c)	2	mm
Level Set Resolution	0.07	mm/pix	Wall Strain Rate	0.08	mm/sec
Surface Point Discretization Density	2	pts/pix			

Table 2.2: Parameters for Oedometric Testing.

Specimen Setup

The specimen setup described in this section is intended to simulate a cross section of a cylindrical oedometer test specimen. The grains that were utilized for this were the same shapes as from the crushing example and again were picked from a pool of 25 total grains. The material properties were set the same as the silica sand from oedometric experiments done by Nakata et al. (Nakata et al., 2001) in an attempt to compare our simulation to their experimental results, and are shown in Table 2.2. This was done by calibrating the stiffness so the simulation matches the experiment constitutively in the regime where there is no breakage. The yield stress for the particles were then set so grains would start breaking at the same time as when breakage initiated in the experiment. This resulted in slightly different critical stress values for each criterion. The graphical depiction of these values were presented in Section 3.1 in Figure 2.2, and a discussion on this will be left to the next section.

There was no consideration for particular particle shape properties since the actual shapes from the experiment are not known, therefore the accuracy of these tests will be more focused on the physics rather than a one-to-one matching that has been done in previous studies with LSDEM (Kawamoto et al., 2018b). The initial PSDs were nearly uniform between 1.4 and 1.7 mm for both the simulation and experiment as shown in Figure 2.13. Matching the initial PSD is critical since it has been shown in experiment that a more graded sample will affect both constituitive properties and final PSD (Nakata et al., 2001; F. L. Nakata et al., 1999). As discussed earlier, initially there was a consideration to have a buckling breakage mode to avoid unnaturally thin particles. While this mode seems intuitive, in application it causes an un-physical kinking in the PSD. We believe this is due to the particles that reach this criterion are set to cut in half, which eliminates certain particle sizes from being achievable. An example of this phenomenon is shown in Figure 2.9.

The numerical specimen was set to have the same height (10mm) as the experiment and set to have the same width as the diameter of the experiment (50mm). Porosity was matched by using an equation suggested by (Wang et al., 2014),

$$\phi_{2D} = 0.42 * \phi_{3D}^2 + 0.25 * \phi_{3D} \tag{2.22}$$

which resulted in our simulation having an initial void ratio of 0.18 which corresponds to a three dimensional void ratio of 0.6. With a fixed specimen dimension, the PSD and void ratio targets were achieved by placing in grains that were scaled to match the PSD requirement until the allowable volume of solids in the specimen was reached. This resulted in the final specimen having 144 grains before loading.

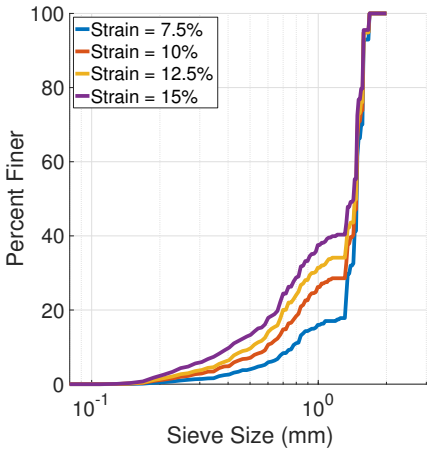

Figure 2.9: PSD using the von Mises criterion and the buckling breakage mode. Kinking in the curve can be observed due to the inability of the buckling breakage to achieve a wide range of breakage sizes.

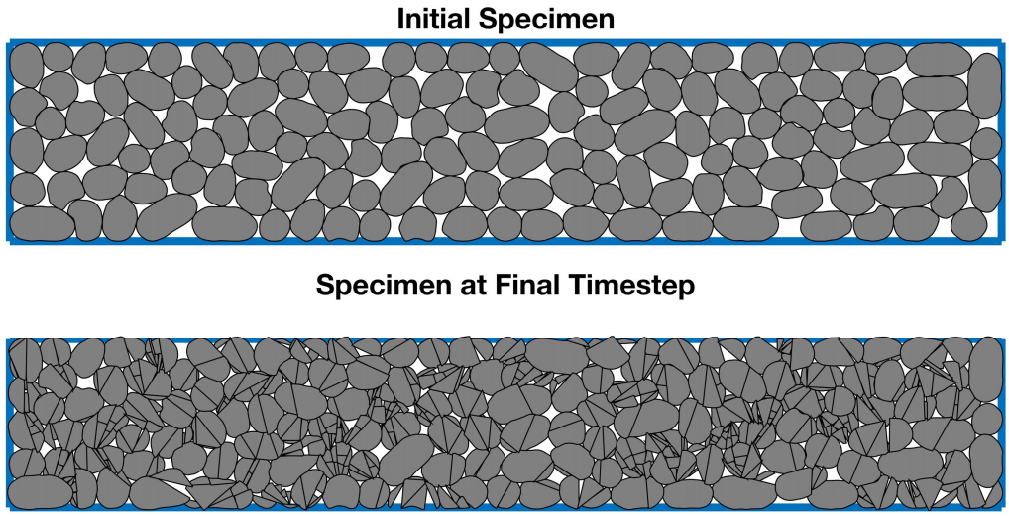

Figure 2.10: Visualization of the oedometric test at the initial and final timestep.

Results

The results discussed here are from a set of DEM simulations from the specimen described before. While intended to completely mimic the experiment, only half of the total imposed displacement from experiment was done in simulation. This is because of limits in void space in two dimensions so that the simulation could only reach strains of around 15%. Despite this, many useful comparisons can be made at these lower strain levels.

The results for the model and its comparison to experiment will first be looked at for the constitutive relation. Figure 2.11 plots the stress vs strain and void ratio for both

the model and experiment. Since LS-DEM without breakage has been validated in previous papers, matching the first three data points was expected as little or no breakage had occurred yet. The comparisons for the breakage model start at around a strain of 5% where the model and data still align quite closely. Some lack of smoothness can be observed during the breakage region for the model which we believe would be greatly minimized from having a larger sample so that individual breakages do not affect the macroscopic properties as heavily. We also observe that all three breakage criterions can achieve the same macroscopic response, the main difference being that they must be calibrated to a different value. While the Tresca and maximum principal stress criterions correspond to a compression strength of 40 MPa, the von Mises correspond to a compression strength of 35 MPa. The fact that the Tresca and maximum principal stress criterions predict higher breakage stresses is expected since these are more conservative criterion measures. Considering the very similar constituitive response and the shape of the three yield surfaces, it seems that the most important part of the yield surfaces are the compressive regions where all three yield surfaces overlap.

The PSD was also compared at both the initial and final stages of the test and shown in Figure 2.13. Again each criterion produce very similar results and match closely with experiment. In Figure 2.12, the evolution of the PSD is shown with similar results across all three criterions at high strains. Some differences can be seen for the principal stress criterion at low strain rates, which is likely due to each simulation having a different seed for initial strength values. Once more breakage has occured, the curves more closely align showing that the true strength distribution is seen by the material response.

While the level of breakage seems to be consistent with experiment, the model predicts slightly more large particles and slightly less small particles. These limitations would likely come from either using only straight cracks on a small specimen or differences in definition of sieve size between two- and three-dimensional granular materials. Investigating this effect on larger specimens in three dimensions may eliminate this issue, where there would be less statistical variance and the sieve size would be better identified as the three dimensional intermediate axis length instead of the two dimensional minor axis length. Another way that this could be improved is by defining fracture surfaces with more data-intensive methods such as either intra-particle stress distribution methods such as the boundary element

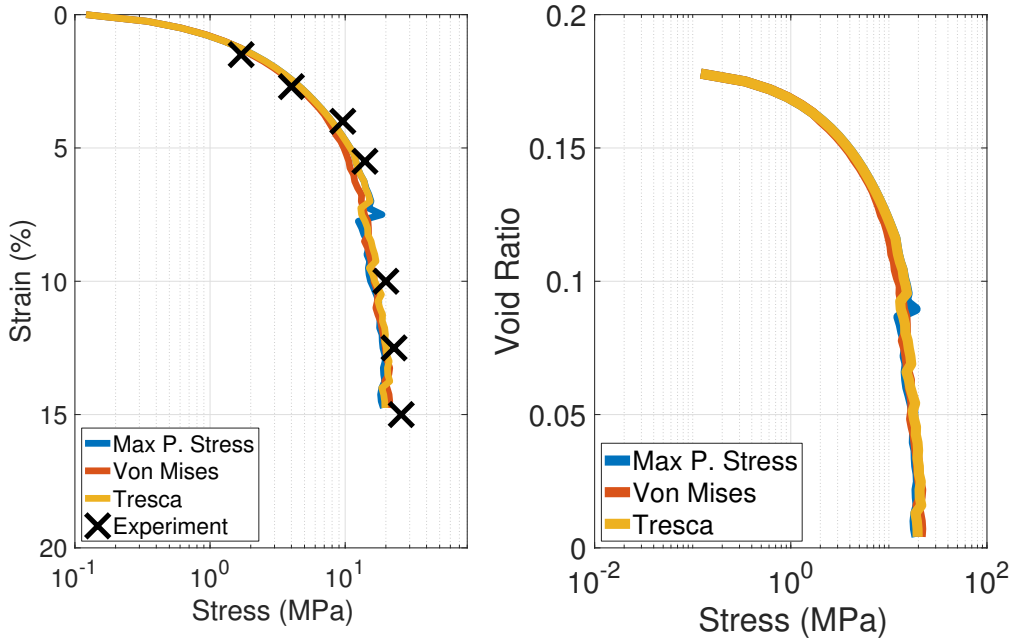

Figure 2.11: Stress curves for each stress criterion calibrated to experiment.

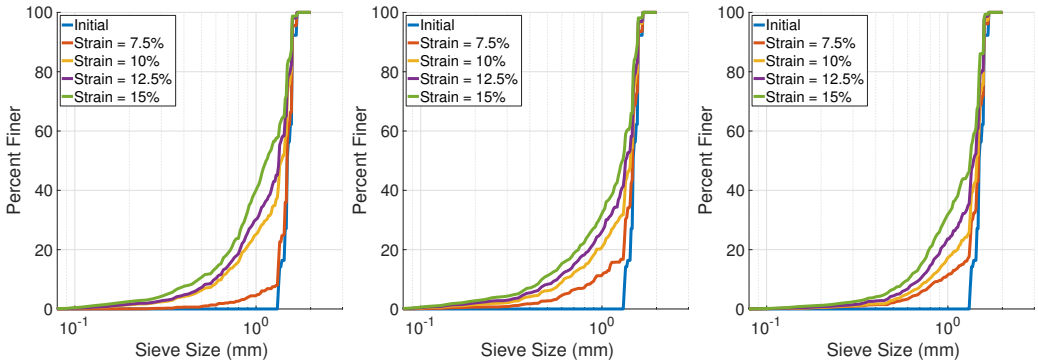

(a) Principal Stress Criterion (b) von Mises Criterion (c) Tresca Criterion

Figure 2.12: Growth of PSD for each criterion studied.

method (Jiang et al., 2019) and the ghost-point finite difference methods (Coco et al., 2013), or from XRCT images of breakage.

Another interesting trend was found by taking a closer look at the grain scale. Since the level set splitting method can capture exact shape, it is an ideal model for investigating changes in grain shape which we will do for the von Mises criterion simulation. Here we will look at the development of shape by looking at the true circularity, the two dimensional analog to true sphericity, and the aspect ratio (AR) for each particle. The true circularity is measured as the ratio between the circumference of a circle with the particles volume and the perimeter, ρ, of the

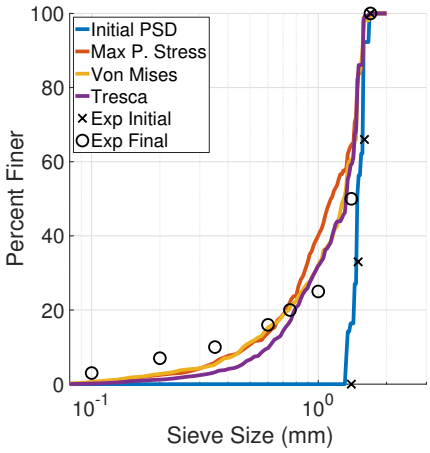

Figure 2.13: Particle size distributions at initial and final state for experiment and simulation using each of the three breakage criterions.

particle, the calculation for which can be simplified to

$$Circularity = \frac{4\pi V_p}{\rho^2} \tag{2.23}$$

For comparison, true sphericity of a particle is defined as the ratio between the surface area of a sphere with the same volume and the surface area (Wadell, 1932). AR here is defined by the ratio between the short axis and the long axis of a best fit ellipse on the particle.

Figure 2.14 shows the trend of the average circularity and average AR as a function of the macroscopic vertical strain applied to the specimen. Both true circularity and AR drop as particle sizes get smaller. This is consistent with trends of both AR (Afshar et al., 2017; Altuhafi et al., 2011; Sun et al., 2014; Zhao et al., 2015; Takei et al., 2001), and sphericity (Sun et al., 2014; Zhao et al., 2015) in experiments. Some experiments however have reported that sphericity can increase during light breakage before sphericity drops during heavy breakage (Afshar et al., 2017). We believe this is not seen in our results for two reasons. First is that our particles are already very circular at the beginning of the test, so an increase in sphericity would be difficult. The second reason is that this model as of now does not attempt to replicate chipping, which has been experimentally shown to be the dominant breakage phenomenon at lower stress levels, while splitting is dominant at high stress levels (Karatza et al., 2019). Chipping is the effect of very small breakages focused around a single contact point on a particle. Chipping would likely have a large chance for shaving off sharp corners that would contribute to an initial particle's lack of sphericity, thereby increasing the sphericity after breakage. While chipping

is a possible effect to model using level set splitting assuming a certain chipping criterion, it was not attempted in this paper.

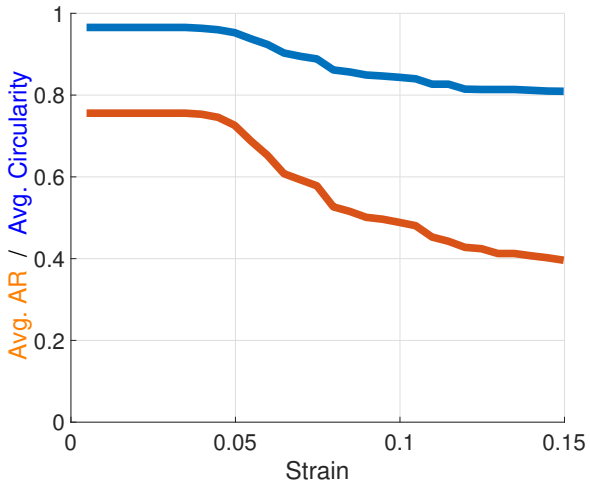

Figure 2.14: Trend in average circularity and average aspect ratio of the particles as the macroscopic strain increased on the specimen.

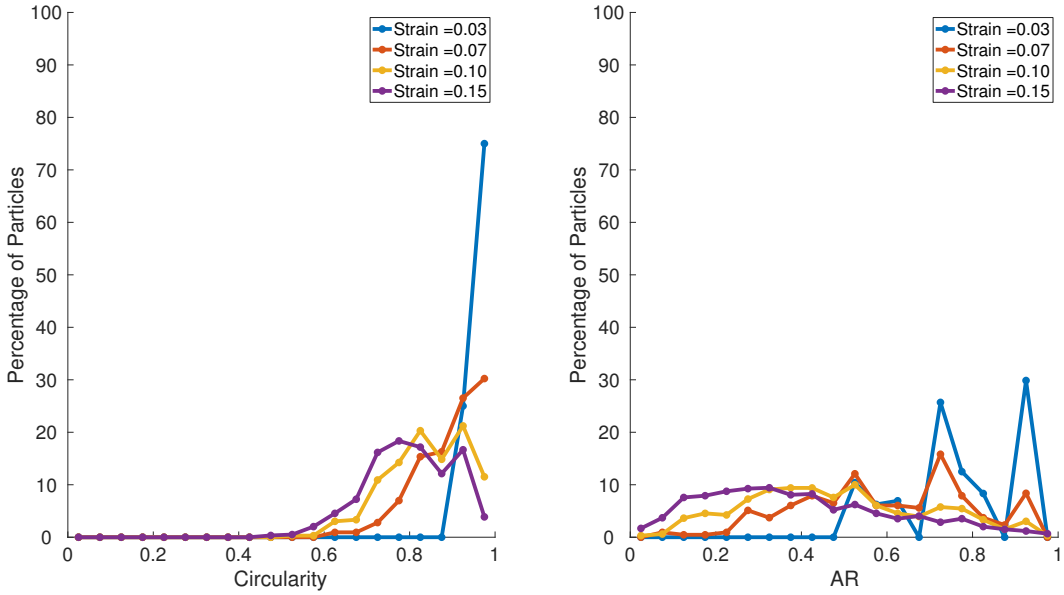

Figure 2.15: Histograms of particle circularity and aspect ratio as a function of strain on the specimen.

Figure 2.15 shows a series of particle sphericity and AR histograms as a function of global strain on the specimen. Bins for the histograms were segmented at 0.5 intervals in a way so that the center of the bins are depicted as dots on the figure. Since only 25 unique particles are used, the initial distribution of particle shapes is

not well varied. Over the course of the experiment, the particles' circularities and ARs become much more varied. This is to be expected since some particles will break much more than others and cause the particle shapes to take a more varied distribution. These results further suggest that the particle shape has a significant effect on both the likelihood of breakage on any single particle and on the nature of breakage as damage increases.

2.7 Conclusion

Modeling breakage in granular materials has always been challenging due to the complexities of the breakage process and capturing arbitrary shape changes. This paper presented a modeling method that provides an avenue for addressing the difficulties in modeling the morphological changes that occur in breakage. In doing so, we demonstrated how the level set splitting method can thrive in various realms where DEM finds a use.

The first example was for comminution modeling for a jaw crusher. We showed how the level set splitting method can make very accurate predictions on the PSD of the jaw crusher output. Abilities for this model to make additional important predictions on performance for both jaw crushers and other crusher types were discussed as possible future work. The second example was a classic oedometric test where we showed that level set splitting can make reasonable comparisons with experiment even with quite small samples. In fact, predictions could be made at both the macroscopic scale, such as for constitutive modeling, and also at the grain scale, such as with predicting changes in particle shape.

Future work with this method will certainly include quantitative validation exercises in three dimensions, using XRCT to capture the true particle shapes of the material. Further work can also be done with using XRCT to determine the exact time and fracture surface of a breakage, allowing for the study of single particle breaks. This could answer questions about how the contact forces are affected during breakage.

While already capable of making good predictions on granular breakage, this method can certainly be improved. For example, three simple breakage criteria were used in this paper. A breakage criterion where the breakage stress is based on a field of intraparticle stress may be more realistic for many materials. Also improvements in fracture surface shape could greatly improve the accuracy at the granular level. This could be done either with calculating a stress distribution or by using the data from tomography to have a data-based method for fracture surface generation. For

possibly a more simple addition, adding available extensions to this method to model more breakage types, such as chipping, may increase accuracy of the method even further as well.

2.8 Appendix: Calculating Material Properties for Particles

For the purposes of building new particles, here we present an explanation on how to determine the material properties using just the information from the discrete level set function. The three key material properties to compute is the mass, center of mass, and the moment of inertia.

First, we define the smoothed Heaviside function, $H(\phi)$, as,

$$H(\phi) = \begin{cases} 0 & \phi < -\epsilon \\ \frac{1}{2}\left(1 + \frac{\phi}{\epsilon} + \frac{sin(\frac{\pi\phi}{\epsilon})}{\pi}\right) & -\epsilon \leq \phi < \epsilon \\ 1 & \epsilon \leq \phi \end{cases} \tag{2.24}$$

where ϵ is a smoothness parameter set to $\epsilon = 1.5$. Assuming the particle has uniform density, ρ, and unitary grid spacing, the mass can be computed in 3D as,

$$m = \rho \sum_{i=1}^{I} \sum_{j=1}^{J} \sum_{k=1}^{K} H(-\phi(x_i, y_j, z_k)) \tag{2.25}$$

and in 2D as,

$$m = \rho \sum_{i=1}^{I} \sum_{j=1}^{J} H(-\phi(x_i, y_j)) \tag{2.26}$$

where I, J, and K are the maximum grid dimensions in each direction. The center of mass can then be computed in 3D,

$$\begin{aligned} \bar{x} &= \frac{\rho}{m} \sum_{i=1}^{I} \sum_{j=1}^{J} \sum_{k=1}^{K} H(-\phi(x_i, y_j, z_k)) x_i \\ \bar{y} &= \frac{\rho}{m} \sum_{i=1}^{I} \sum_{j=1}^{J} \sum_{k=1}^{K} H(-\phi(x_i, y_j, z_k)) y_j \\ \bar{z} &= \frac{\rho}{m} \sum_{i=1}^{I} \sum_{j=1}^{J} \sum_{k=1}^{K} H(-\phi(x_i, y_j, z_k)) z_k \end{aligned} \tag{2.27}$$

and in 2D,

$$\begin{aligned} \bar{x} &= \frac{\rho}{m} \sum_{i=1}^{I} \sum_{j=1}^{J} H(-\phi(x_i, y_j)) x_i \\ \bar{y} &= \frac{\rho}{m} \sum_{i=1}^{I} \sum_{j=1}^{J} H(-\phi(x_i, y_j)) y_j \end{aligned} \tag{2.28}$$

Then, finally the moment of inertia for 3D,

$$I_{xx} = \rho \sum_{i=1}^{I} \sum_{j=1}^{J} \sum_{k=1}^{K} H(-\phi(x_i, y_j, z_k))[(y_j - \bar{y})^2 + (z_k - \bar{z})^2]$$

$$I_{yy} = \rho \sum_{i=1}^{I} \sum_{j=1}^{J} \sum_{k=1}^{K} H(-\phi(x_i, y_j, z_k))[(x_i - \bar{x})^2 + (z_k - \bar{z})^2]$$

$$I_{zz} = \rho \sum_{i=1}^{I} \sum_{j=1}^{J} \sum_{k=1}^{K} H(-\phi(x_i, y_j, z_k))[(x_i - \bar{x})^2 + (y_j - \bar{y})^2]$$

$$I_{yz} = I_{zy} = -\rho \sum_{i=1}^{I} \sum_{j=1}^{J} \sum_{k=1}^{K} H(-\phi(x_i, y_j, z_k))(y_j - \bar{y})(z_k - \bar{z})$$

$$I_{xz} = I_{zx} = -\rho \sum_{i=1}^{I} \sum_{j=1}^{J} \sum_{k=1}^{K} H(-\phi(x_i, y_j, z_k))(x_i - \bar{x})(z_k - \bar{z})$$

$$I_{xy} = I_{yx} = -\rho \sum_{i=1}^{I} \sum_{j=1}^{J} \sum_{k=1}^{K} H(-\phi(x_i, y_j, z_k))(x_i - \bar{x})(y_j - \bar{y}) \tag{2.29}$$

and in 2D,

$$I = \rho \sum_{i=1}^{I} \sum_{j=1}^{J} H(-\phi(x_i, y_j, z_k))[(x_i - \bar{x})^2 + (y_j - \bar{y})^2] \tag{2.30}$$

Chapter 3

PREDICTING CONTACT FORCES AND PARTICLE STRESSES IN CRUSHABLE SAND

Harmon, J.M. et al. (2021). "Predicting contact forces and particle stresses in crushable sand". In: *Geotechnique (submitted)*.

3.1 Abstract

In this paper, we endeavor to predict the evolving statistics of inter-particle contact forces during comminution using grain-scale computational modeling. First, a validation is carried out by creating a one-to-one virtual avatar of an Ottawa sand specimen from 3D X-ray tomography with level sets and comparing the data from an oedometric test to the model's prediction. The predictive capabilities are confirmed from comparing the constitutive response, grain size distribution, and changes in particle shapes in both the experiment and model. Once validated, we delve into the predicted contact forces and particle stresses. We find that the largest particles experience the largest forces. Despite larger particles being weaker on average, many survive due to being on the stronger side of the particle strength distribution and also having a higher coordination number producing a more isotropic stress state in the particle. These highest forces are largely aligned with the specimen axis demonstrating that larger particles provide the strength in the loading direction. Meanwhile forces in the radial direction are more broadly distributed indicating that small particles play a significant part in providing radial stability.

3.2 Introduction

The effects of breakage in granular materials have been an elusive subject due to some inherent difficulties. For one, complete repeatability in experiment is impossible due to the irreversibility of breakage compounded with the fact that there is no uniformity in the microscopic properties of specimens such as individual particle shape or their arrangement. Experiments have also not been able to provide information on the contact forces between particles for real sands in specimens experiencing breakage. This fact limits the insightfulness of experiments and highlights the need for modeling, particularly like the discrete element method (DEM), to provide reproducibility and contact force information. DEM is capable of doing this by

representing every particle individually using rigid bodies that interact with springs and dampers originally shown in ((Cundall et al., 1979). DEM has had its own difficulties as well however, often having to compromise between accuracy and efficiency. Despite these difficulties significant strides have recently been made in both experiment and modeling.

To characterize the response of granular materials in three dimensions, 3D X-ray tomography has been used (Andò et al., 2012; Cil et al., 2014; Wang et al., 2004), and has explored breakage in granular materials over the last decade. For example, (Garcia et al., 2009) used this method to explore the correlation between interfacial area of single particles and grain boundary fracture, and quantitatively analyzed the degree of preferential grain boundary fracture at particle level. (Zhao et al., 2015) showed that the initial particle properties such as morphology, heterogeneity, and mineralogy of single particle breakage influence the particle-level fracture strength. With the benefit of the improved interplay of X-ray tomography scanning and sample size, successive scans of the assembly of sand have enabled capturing the continuous response of granular materials through one-to-one matching of grains. The size-dependent strength of individual particles on yield strength at assembly-scale via 3D X-ray images was examined and it was revealed that the breakage of individual particles affect the macroscopic response of the granular system (Cil et al., 2020). (Karatza et al., 2019) captured breakage by using 3D X-ray tomography in triaxial testing showing significant breakage characteristics in the shear banding region. While those studies present the importance of considering breakage in the granular system, the shape effects, which directly determine the system-level characteristics, have been relatively less explored. Some recent studies have begun to investigate the matter however, such as (Zhao et al., 2015) showing that the evolution of particle morphology and coordination number at the particle scale is dependent on the fragment scale under different assembly densities. (Seo et al., 2020) extracted the variation of shape factors of ongoing fractured agglomerates during an oedometer test with consecutive scans, presenting that all morphological indices converge to a similar range of shape values at high compression. Those recent studies support that the measurement of particle shape evolution for a high breakage density specimen is critical data due to the established importance of particle shape in granular mechanics, e.g. (Murphy et al., 2019).

With the correct validation completed, a predictive DEM model can capitalize on reproducibility by conducting its own experiments via virtual testing. Virtual

testing of this kind is already reliably conducted for granular materials that are not experiencing breakage, providing information experiments cannot achieve e.g. (Karapiperis et al., 2020b). When breakage is added, the most common DEM methods have been largely confined to using geometrically limited particle shapes such as spheres or clumped spheres e.g. (Ben-Nun et al., 2010; McDowell et al., 2013). Some recent developments in breakage modeling have improved the capabilities of modeling particle geometry such as with the use of polyhedrons e.g. (Zhu et al., 2019; Jiménez-Herrera et al., 2018). Polyhedrons however cannot easily handle concavities in the particle shape, and often must use a convex hull of the true particle. Some studies have captured the true particle shape by using a finite element model on every particle, however with a considerable expense in efficiency e.g. (Iliev et al., 2019; Imseeh et al., 2018). Here we are presenting the first three dimensional validation of the level set variant of DEM (LSDEM) that uses the level set splitting technique first introduced in Harmon et al. (Harmon et al., 2020). The level set variant of DEM has no shape limitations and has already been shown to be predictive without breakage and can model macroscopic specimens with >50,000 particles (Kawamoto et al., 2018b). The level set splitting addition allows for breakage and has shown some evidence already of being predictive in two dimensions.

One of the most useful aspects of a validated DEM model is the ability of DEM to uncover the forces between particles. (Daniels et al., 2017) suggested methods to quantify the contact forces of particles in the way of photoelastic measurements. Through the optical stress intensity via birefringence, they provided the estimation of vector contact forces though this method is restricted to two dimensions and photoelastic materials. Recently, (Hurley et al., 2018) used 3D x-ray diffraction methods to measure average particle strain and thereby calculate stress and contact forces in crystalline spheres. (Li et al., 2019) was able to obtain the contact forces by applying Hooke's law to calculate the stress from the strain measured via digital image correlation method (DIC). This study is particularly important here since it found that LSDEM provides similar forces to the measurements.

The organization of this paper is designed to provide a validation of the level set splitting technique followed by an investigation into the contact forces seen in the model. This will be achieved by first conducting an overview of the experimental work that is being used for validation and how a numerical avatar can be developed from it. Then the model will be introduced with a summary of the method, its setup,

and how its parameters are determined. Finally, results for the validation and the contact forces will be shown with discussion on some of the implications of the trends in these results.

3.3 Experiments

Uniaxial Compressions Test with 3D X-Ray Tomography

Ottawa sand was tested for a uniaxial compression test while performing 3D X-ray tomography to understand the ongoing response in the sand assembly. The sand sample was sieved between #20 (840 μm) and #40 (420 μm) in compliance with ASTM standard. After being oven dried at 110°C for 24 hours, the sand was poured into aluminum tubing with a diameter of 4.1 mm through the dry pluviation method and was tamped to achieve the maximum packing density. The prepared specimen had an initial void ratio of 0.60 with a height of 5.0 mm and a median diameter of 600 μm (Fig. 3.1a). The sample was set on the compression device and tested under strain-control conditions at a constant vertical displacement rate of 0.05 mm/min, while radial deformation was prevented by the aluminum tubing. The miniature nature of this customized testing device allowed the system to be mounted in the X-ray tomography beamline while simultaneously acquiring data about the compression response. To generate pervasive breakage, vertical stress beyond the macroscopic yielding point was imposed, thus benefiting from a maximum axial load capacity of the device corresponding to 1112 N, recorded with a resolution of 0.1 N.

The experiment was performed in the GeoSoilEnviroCARS (GSECARS) beamline 13 BM-D of the advanced photon source (APS), Argonne National Laboratory in Lemont, IL, USA, where synchrotron X-ray microtomography (SMT) is available. Specifically pink beam technology was used, which allows rapid high-resolution 3D microtomography (i.e., 4·28 μm/pixel in this study) (Rivers, 2016). The sample under loading was scanned at varying values of normalized vertical stress (σ/σ_y = 0·50, 1·00, 1·33, 1·66, and 2·00, where σ is the applied stress and σ_y is the conventional yield stress (29 MPa) of Ottawa sand determined from preliminary experiments (Fig. 3.1b). Following standard soil mechanics procedures, the yield stress was determined in correspondence with the point of maximum curvature of the compression curve. When the targeted stress, σ, was reached, the sample was stabilized for 10 minutes with a fixed loading piston. Successive X-ray scans acquired through this procedure enabled visual inspection of the developing breakage in the assembly.

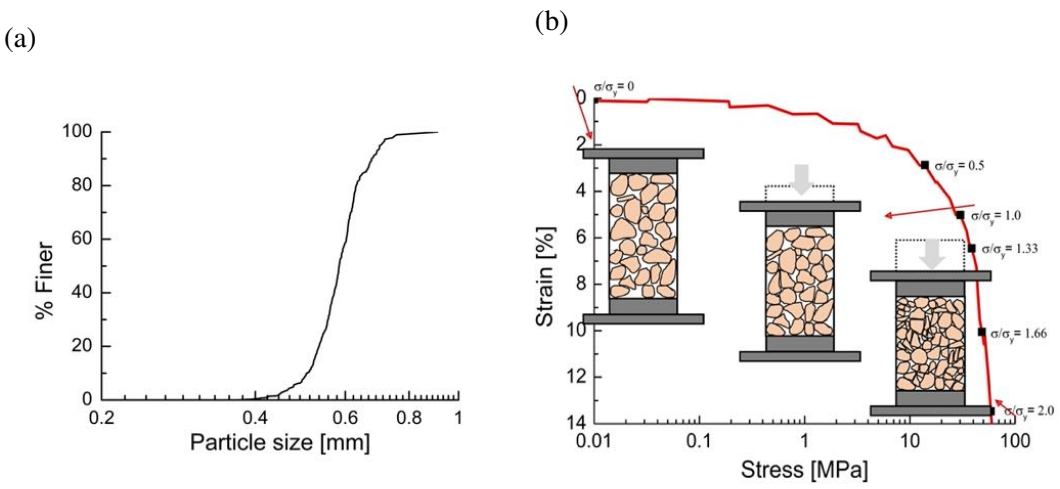

Figure 3.1: PSD used and scan points. (a) Initial particle size distribution of the specimen (b) Schematic of uniaxial compression test and scan points

Image Processing

3D images from SMT allowed quantification of the breakage characteristics at the level of individual grains. For this purpose, corrective procedures were applied, such as the correction of rotations due to inevitable small imperfections of the sample alignment affecting image acquisition during rotation. Hence, to adjust the central point of the acquired raw tomography in accordance with the three-dimensional sample geometry, the image sets were reconstructed through the IDL software available at 13 BM-D (Rivers, 2012), and these reconstructed images were further processed through the commercial software Avizo to isolate individual particles. Figure 3.2 schematically depicts this process with reference to a cropped portion of the original scans. Raw images were filtered to minimize the noise with an anisotropic diffusion algorithm (Kim et al., 1987). The filtered images were then separated into two distinct phases through thresholding criteria based on the lowest value between the solid and void grayscale intensity levels. The remaining local noise from the images were removed by using the remove spot tool. The following step is segmentation of the solid phase into individual particles through a watershed function based on the Chamfer distance (Reynolds, 1883).

The watershed image sets are applicable both to experimental data analysis and preparation of the virtual particles used in LS-DEM. In the image analysis, the watershed particles were labeled, and their geometrical properties were calculated through labeling analysis. Specifically, the volume and the surface of the grains were computed from the voxels allocated to the individual particles in 3D image-wise

and to their boundaries. LS-DEM replicates the particle geometry on the basis of the set of gray and watershed images (Vlahinić et al., 2014). After defining the surface, the level set points are assigned their level set values as the distance from the object surface. To distinguish the level set points belonging to the void and solid phases, it was set to negative values indicated inside the solid and positive values in correspondence with the inter-granular voids. After the level set function is determined, the surface of the particle is discretized into surface points which are important for the leader-follower style contact algorithm.

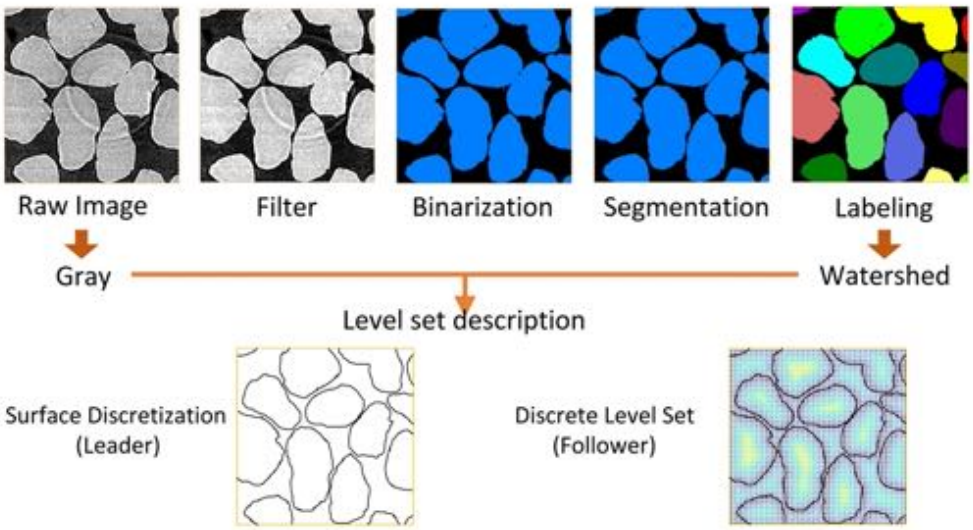

Figure 3.2: Schematics of post-image processing and level set image preparation.

3.4 Modeling Methodology

The level set based DEM variant uses level sets as the geometric descriptor for each particle which describes a geometric surface implicitly through a distance function (Sethian, 1999). From an image, the shape, position, and rotation of every particle is known, enabling the creation of a one-to-one avatar of the experiment. This is the same process that has been done before for a triaxial test that was conducted as a validation of LSDEM (Kawamoto et al., 2016). Readers can refer to (Kawamoto et al., 2016) for the full description of the method without breakage.

Unlike previous three-dimensional comparison studies with LSDEM, this specimen will experience breakage. To enable the level set particles to break, the level set splitting method will be used which was introduced in (Harmon et al., 2020). A summary of this method will be provided here.

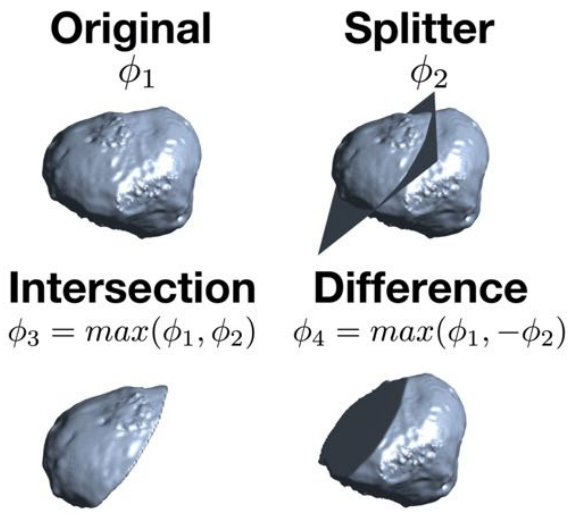

Figure 3.3: Each image shows the zero level isosurface of each level set function. The intersection and difference set operations between the original particle and fracture surface result in a mass conserving split.

Level set splitting uses set operations to separate a single level set into two level sets with a predetermined splitting surface. This operation is done by using the intersection and difference between the original particle level set, ϕ_1, and a proposed splitting surface, ϕ_2, as seen in Figure 3.3 to provide two new particles, ϕ_3 and ϕ_4.

$$\phi_3 = max(\phi_1, \phi_2) \tag{3.1}$$

$$\phi_4 = max(\phi_1, -\phi_2) \tag{3.2}$$

In principle, this surface can be arbitrarily shaped, however for simplicity, we have chosen to only use flat planes as splitting surfaces. To determine when to split a particle, we use breakage criteria calculated from the average stress over each particle. The average stress is determined by its volume, V^p, the contact forces, F_c, and branch vectors, x_c,

$$\bar{\sigma}_p = \frac{1}{V_p} \sum_{c=1}^{N_c} x_c \otimes F_c \tag{3.3}$$

From the average stress, we choose a breakage criterion, which we have chosen to be the maximum principle stress since this is most accurate for brittle materials. This criterion assumes that the breakage will occur due to the tensile internal forces inside the particle. The maximum principal stress is determined from the greatest

eigenvalue of the average stress tensor. The minimum principal stress may also be checked in the case of failure from compression, despite the compressive strength being many times higher than the tensile strength for sand particles, but a failure of this type rarely occurs in this setting. It is well known that particle strength is a function of particle size, famously shown in (Weibull, 1939). These strength differences follow a Weibull distribution.

$$P_f(\sigma \geq \sigma^{max}) = 1 - exp\{-(d/d_0)^3(\sigma/\sigma_{c0})^m\} \tag{3.4}$$

This equation determines the probability of failure from the size and stress state of the particle. Here σ and d is the stress and diameter of a given particle and σ_0 and d_0 is the stress and diameter of a particle that is known to have a 37% survival probability at that state. The parameter m is the Weibull's modulus which is a material property that controls how much the particle strength grows with a given diameter reduction. Smaller values of m result in larger variations of particle strength. Generally values for the Weibull's modulus are in the range of 1-4 (F. L. Nakata et al., 1999).

For implementation, we use inverse transform sampling to determine the critical stresses directly.

$$\sigma_c = \sigma_{c0}\left[-\left(\frac{d_0}{d}\right)^3 ln(1 - P_f)\right]^{m^{-1}} \tag{3.5}$$

Where P_f will be a uniform distribution $U(0, 1)$. After these critical stresses are determined for the initial particles, we determine the critical stresses for child particles from simply relating their critical stresses to their parent particles. We assume that the child particles will have similar internal flaw characteristics as the parent particles and therefore should not have their strength seeded from the distribution again.

$$\frac{\sigma_a}{\sigma_b} = \left(\frac{d_a}{d_b}\right)^{-3/m} \tag{3.6}$$

When a particle breakage event is computed, the splitting surface is created by generating a flat plane from the locations of the three highest contact forces on the particle. In the cases where there are only two contact forces on the particle, the third point used is the particle centroid. The physical properties of volume, center of mass, and moment of inertia of each new particle are recalculated.

3.5 Specimen Preparation and Parameter Determination

The specimen was prepared by taking the level sets developed from the XRCT images and placing them in exactly the same position and rotations as the images. The created particles were slightly smaller than the imaged particles to ensure no particles are initialized in the model in contact, which could cause immediate instability if an initial overlap is significant.

The contact stiffnesses were determined from calibration with experiment in the pre-breakage regime. For this calibration, the breakage was turned off and the stiffness was altered until the model aligned constitutively with the experiment at low stresses. Friction and density have well known values for Ottawa sand (El Ghoraiby et al., 2020). The breakage parameters σ_{c0},d_0, and m were determined from single particle breakage experiments conducted by (Nakata et al., 2001), as well as with further guidance from statistical analysis done by (Zhang et al., 2015). Table 3.1 shows all these values that have been described.

Parameter	Value	Units
k_n	1.5	MN/m
k_s/k_n	0.9	none
μ	0.4	none
ρ	2.65	g/cm^3
σ_{c0}	100 (tensile)	MPa
d_0	0.6	mm
m	3.3	none
P_f	$U[0,1]$	none
Level Set Resolution	8.6	mm/vox

Table 3.1: Parameters used in modeling with values and units.

The level set resolution is usually determined from the resolution of the image. Here the experiment resolution was much higher than what is generally used for LSDEM, so the resolution of the level sets was halved from the experiment to alleviate any memory concerns during simulation.

3.6 Results

Six moments in the experiment will be focused on for comparison in order to provide comparisons at multiple stages. The moments chosen are at strains 0%, 3%, 5%, 6.4%, 9.8%, and 13%. These were chosen because they are the same moments when scans were taken of the experiment and are well spaced for observation of phenomena at many stages of breakage.

Mechanics Validation

First, we will compare experiments and simulations in terms of macroscopic constitutive response. In Figure 3.4(a), these responses are shown for each. Plotting the stress in log space is standard in breakage science e.g. (Nakata et al., 2001) and is helpful for visualizing the large range of stresses the specimen experiences. For the entire range of the imposed axial stress, the model is overlapping or nearly overlapping with the experiment. The plots of the GSD for each previously referenced strain level is shown in Figure 3.4(b). The grain size of the particles for both experiment and simulation was determined by using the diameter of a sphere of the same volume, often called the equivalent diameter. The first few moments have the same GSD due to little to no breakage having occurred yet, however the GSD evolves for the last three moments similarly between model and experiment. This provides confidence that the assumptions of flat breakages and breakages intersecting the highest contact forces produce particles of similar volume as the experiment. The final GSD at 13% axial strain is not necessarily the ultimate GSD, however we can assume that if the model can capture the evolution of grain size, then it can capture the ultimate GSD as well. Both the model and experiment predict the dominant growth of finer particles in the post-yielding region. This observation is emphasized in Figure 3.5 where the model specimen is visualized. It can be easily seen that there are many more particles that have broken 5+ times than particles that have broken 2-4 times at the final stage.

Chipping is an important phenomenon that was observed in experiment however is not seen here. This may be expected since chipping is usually local to a single contact force which is not conducive to the assumption in the model that cracks must intersect multiple contact forces. Despite this, the lack of chipping does not seem to have affected the GSD and constitutive comparisons. The very fine region of the GSD curve, a region where chipping is the dominant mechanism for particle creation, has errors for both model and experiment due to limitations at small particle sizes. For experiment, fines with volumes less than 0.001 mm^3 were removed due to uncertainty in measurement. In the model, small particles cause instability and poor shape representation, so a size limit is implemented at 10 surface points or 15 level set voxels. Particles at these sizes however are small enough to lose confinement and migrate significantly in the void space of the specimen, resulting in those particles producing little effect on the mechanics.

(a) (b)

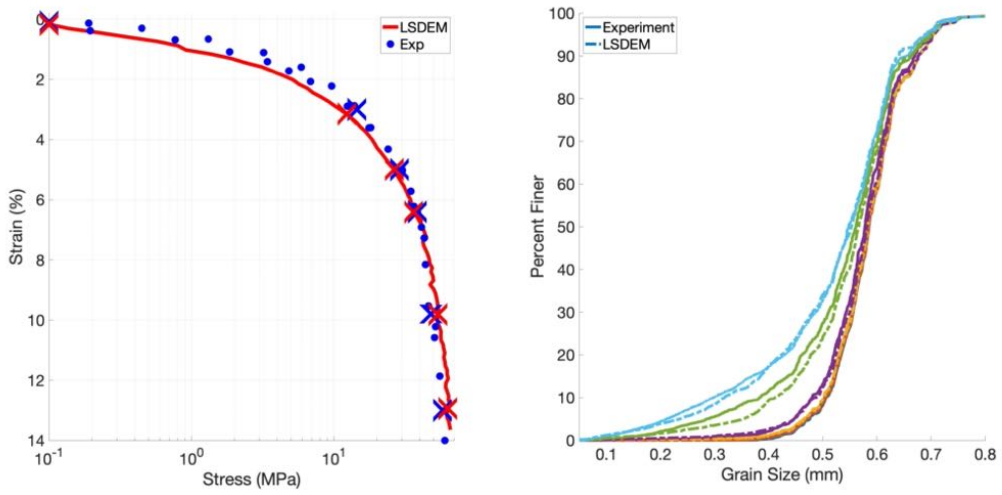

Figure 3.4: Stress-strain and GSD evolution. (a) Constitutive response comparison with markings placed at stresses in which the grain size distribution is plotted on the right. (b) Grain size distribution evolution at 0%, 3%, 5%, 6.4%, 9.8% and 13% strain for both model (dashed lines) and experiment (solid lines).

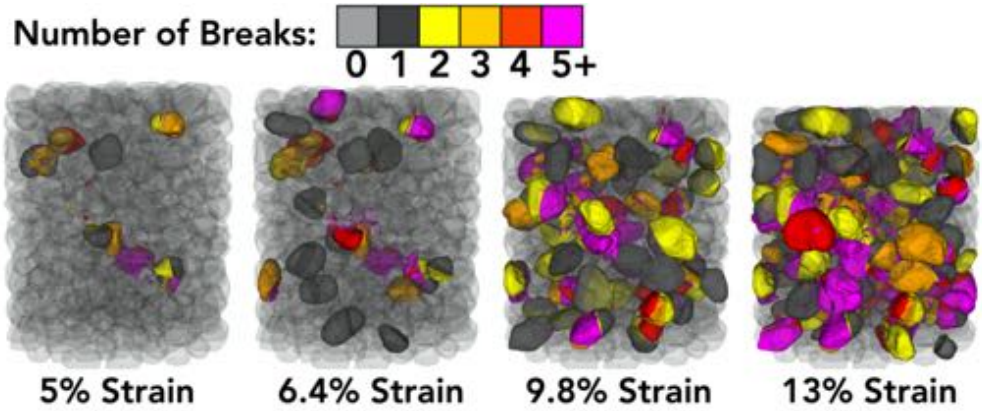

Figure 3.5: Visualizations of the breakage for the last four simulation steps. Opacity is increased for particles that have experienced at least one break.

Particle Shape Validation

When the model is initialized, all the particles have the same shape virtually as they do in the experiment. As the particles break at higher stresses however, the new particles in the model are far from guaranteed to have the same or similar shapes as the experiment. To investigate the extent to which the shapes in the model diverge

from the shapes in experiment, each will be compared quantitatively at multiple stages.

The sphericity of a particle is a measure of how close that particle shape is to a sphere and is used often in microscale analysis of granular matter (Blott et al., 2008; El Ghoraiby et al., 2020). The sphericity of a particle, S, is calculated as the ratio between the surface area of a sphere with the same volume and the surface area of the particle itself. This ratio can be simplified to the following equation,

$$S = \frac{\sqrt[3]{36\pi V_p^2}}{A} \tag{3.7}$$

From the experimental data, Figure 3.6 shows the histogram of sphericity at each scan point. At the initial stage, 50.7% of particles had sphericities between 0.90 and 0.95 indicating a narrow distribution. At yielding (Figure 3.6b) where noticeable amounts of breakage initiate and the portion of fines increases, fragments appear in a lower range of sphericity (0.45-0.80). This range becomes more common for both simulation and experiment at subsequent scan points as well, showing that breakage in the assembly results in producing angular fragments. This is expected since the wide variety of fracture shapes that could happen should result in a wide variety of particle shapes from the child particles. Through the image analysis of experimental data, we conclude that breakage in granular materials triggers a large variation of particle geometry, and this is also captured by the model. This evidence suggests that the assumptions of flat fracture surfaces and breakages connecting the largest contact forces are reasonable. The model does predict sphericities that are lower than experiment, but this could be expected from the nature of flat fractures creating sharp corners at the edges paired with the lack of chipping in the model that could serve to smoothen those edges.

As other variables that describe particle geometry, flatness is a measure of flat form (e.g., oblate) expressed as a ratio of shortest length (S) over intermediate length (I) while elongation is a term to describe elongated grain such as rod or prolate shape, quantified as a ratio between the intermediate length (I) over the longest length (L) (Blott et al., 2008).

$$Flatness = S/I \tag{3.8}$$

$$Elongation = I/L \tag{3.9}$$

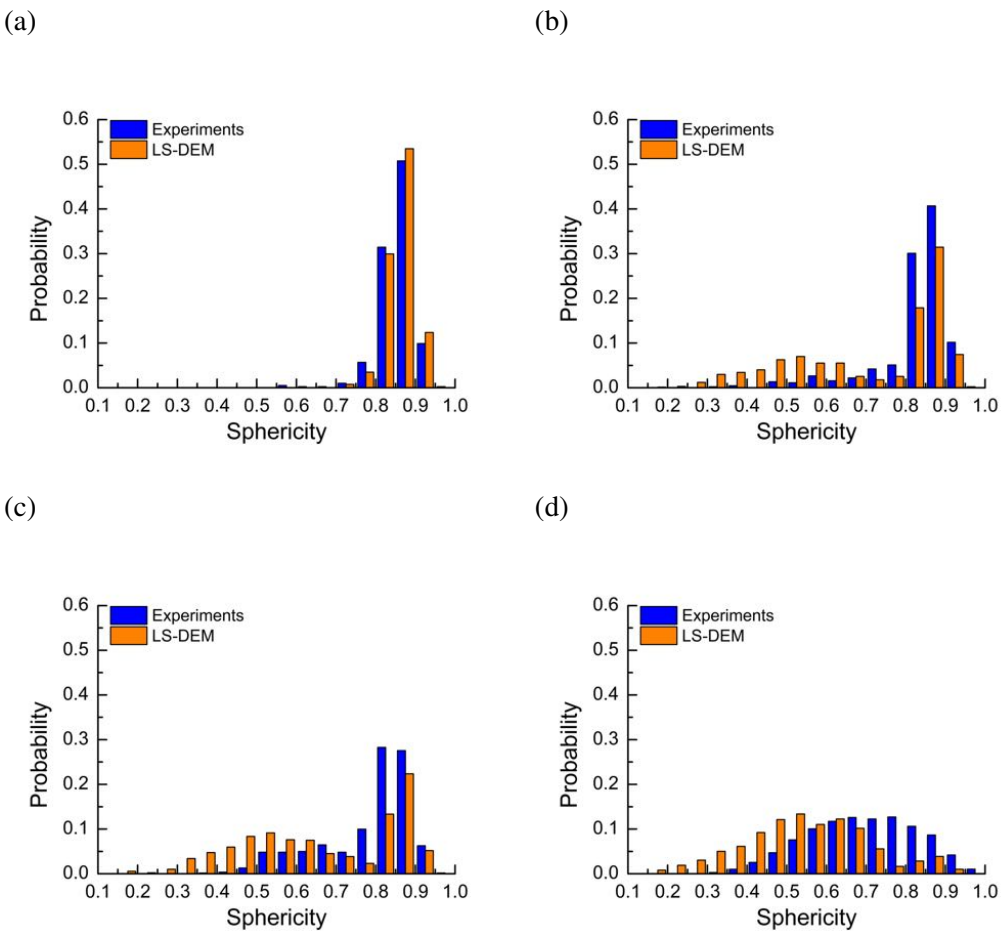

Figure 3.6: Sphericity distribution of entire particles from experiments at strains (a) 0 %, (b) 5%, (c) 6.4%, (d) 13%.

Figure 3.7 shows comparisons of the average flatness and elongation over time of the particles for both experiment and the model. These properties were determined by the ratio between principal lengths fitting to a circumscribing ellipsoid having the minimum volume. In experiments, flatness decreased from 0.80 to 0.61 while the initial value, 0.80 of flatness in LS-DEM dropped to 0.60. The overall Flatness in LS-DEM shows 1.08 % of an average error on the basis of the experimental data. In addition, the Elongation of the particles including fragments in LS-DEM evolved the same as those of experiments by having 0.87 % of an average error. This indicates that LS-DEM can replicate particle shape alterations with a very high level of accuracy.

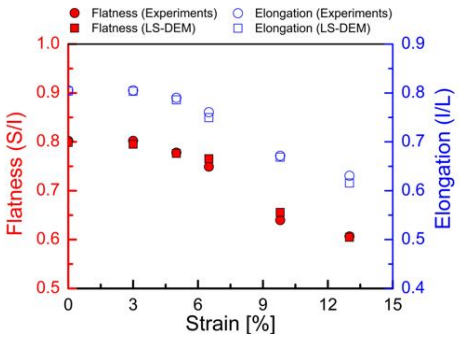

Figure 3.7: Evolution of average Flatness and Elongation for experimental results and LS-DEM data.

Investigation of the Contact Forces

Unlike the experiment, the model can report contact forces experienced by particles in the specimen. In this section, some observations of the reported contact forces from the model will be shown to demonstrate this capability and investigate the microscopic nature of breakage.

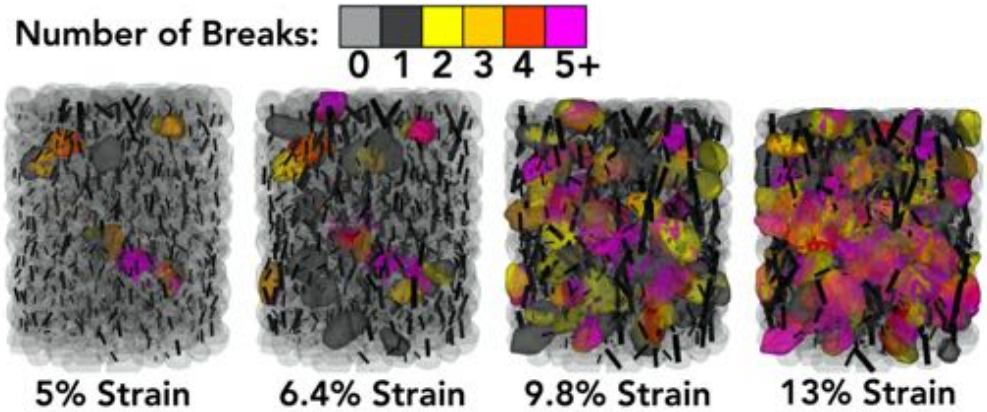

Figure 3.8: Same as Figure 3.6, but with interparticle contact forces added and opacity reduced for all particles to better see the contact forces. Thickness of black lines is proportional to the force magnitude.

Figure 3.8 visualizes the contact forces with the specimen at the same four moments shown in Figure 3.5. The forces are shown as black lines whose thickness is proportional to the magnitude of the contact force and are aligned with the direction of the contact force. As the stress in the specimen increases from left to right, there is a clear increase in higher magnitude contact forces. This is despite an increase in the total number of contacts from the increase in particle numbers indicating that the effect of spreading out the stress over a larger number of contacts does not limit the increase in contact force with increasing compression. Higher forces do not tend

to exist in regions with high levels of breakage which we can observe by noticing a lack of thick black lines in the regions of particles that have experienced 5+ breaks. Another observation of the model is that if a particle is to break many times, it does so rapidly because one break is not often enough to alleviate the stress in the region. In the experiment, it was shown that both "comminution" events where one particle breaks into many particles exist as well as "splitting" events where one particle breaks into only two particles. Despite the model only allowing splitting events, there are many times where there are multiple subsequent splitting events that culminate to what could be described as a comminution event. After these comminution events, the forces in that region significantly decrease and cause a shielding effect on the new particles, disallowing further breakage. So, while most forces in the specimen increase with increasing stress, when particles experience many breakages, the forces in that local region tend to decrease.

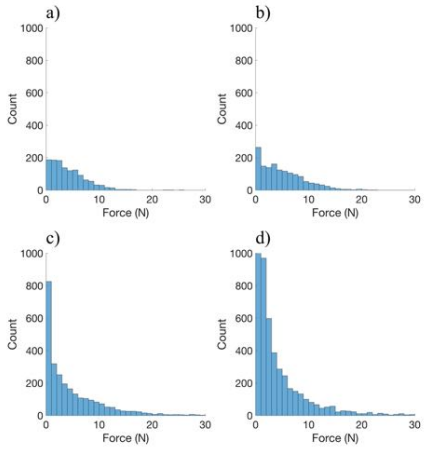

Figure 3.9: Histograms of contact force magnitude at strains (a) 5%, (b) 6.4%, (c) 9.8%, (d) 13%.

Figure 3.9 shows further evidence of this due to the large increase in small forces at higher stresses where significantly more breakage exists. This figure also shows that larger forces in the >20N range only seem to exist at the higher levels of strain. While the number of forces at the extremes increase, the number of forces in a mid-range around 7-12N remain similar. It can more generally be described that the force magnitude distribution is more uniform at lower strains when the PSD is more uniform than later in the experiment when the specimen has a more graded PSD.

There are two effects that enable many large particles that are both statistically weaker and experience high contact forces to resist breakage throughout the experiment.

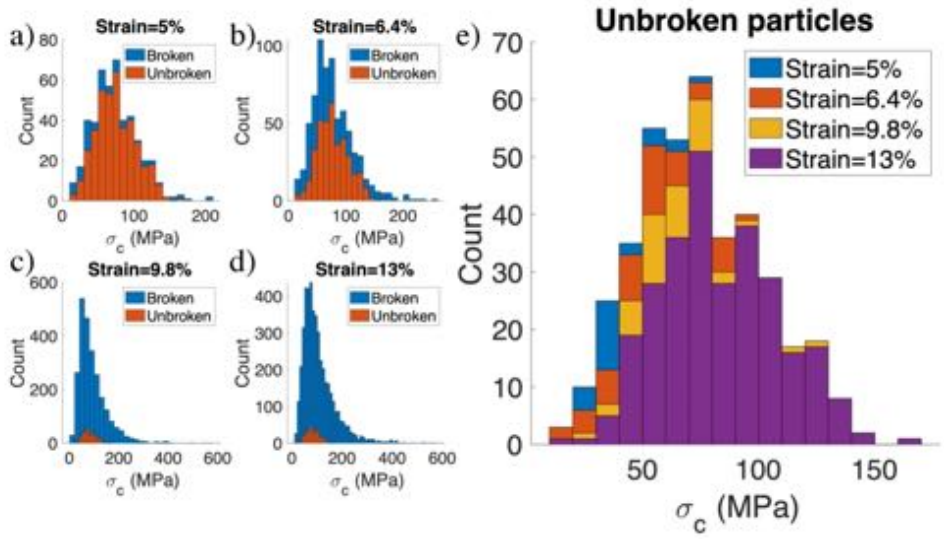

Figure 3.10: (a)-(d) Histograms of breakage stress for both broken and unbroken particles at strains of 5%, 6.4%, 9.8%, and 13%, respectively. (e) Histograms of only the unbroken particles for multiple strains indicating that largely the weakest particles were the ones that broke.

These are a survival of the fittest effect and the cushioning effect. Because the strengths of the initial particles are seeded from a distribution, from the beginning, there is a significant variation in particle strength when the particles all have similar volumes as shown in Figure 3.10 and so naturally the average strength of unbroken particles will increase as the stronger particles survive and the weaker ones break. In Figure 3.10a-d, the histograms of particle strengths of both broken and unbroken particles are shown at various strain levels. While unbroken particles that are generally larger do have lower average strength, there are many broken particles that have the same strength or are weaker meaning that large unbroken particles are not necessarily the weakest. Broken particles are mostly produced by the weakest of the original particles, as seen in Figure 3.10e where the count of unbroken particles of low strength significantly decreases over the course of compression. Because broken particle strength is directly related to the strength of its parent particle, this further explains why many broken particles have lower or similar critical stresses compared to unbroken particles.

The cushioning effect also enables the survival of larger particles due to higher coordination numbers producing more isotropic stress states, allowing large particles to experience higher forces without an increase in maximum principal stress. To quantify the contact force statistics for different particle volumes, Figure 3.11a uses

a concept of average pair volume which is the average volume of the two particles that share a given contact force. In Figure 3.11a, we show the average contact force for each average pair volume bin, in which case there is a clear correlation between average pair volume and contact force. This observation indicates that it is indeed the larger particles that on average experience the large forces that then produce the bulk of the specimen strength. Figure 3.11b uses the same plot in Figure 3.9d but with a color coding that represents the average pair volume of that contact force. For this plot, the average pair volume is compared to the average volume of all particles in the specimen. The plot shows that forces with an average pair volume below 50% of the average particle volume of the specimen are responsible for the bulk of the smallest forces that are <3-4N, but are nearly non-existent for larger forces that are >10N. Forces with average pair volumes that are greater than twice the average particle volume however seem to be equally likely to have the force magnitude to be between 1-15N and are the only average pair volumes to have forces >15N. In Figure 3.11c, the Pearson's correlation coefficient, ρ, between two quantities, A and B, is used and is calculated as,

$$\rho(A,B) = \frac{1}{N-1}\sum_{i=1}^{N}\left(\frac{A_i-\mu_A}{\sigma_A}\right)\left(\frac{B_i-\mu_B}{\sigma_B}\right) \tag{3.10}$$

where μ is the mean and σ is the standard deviation of the respective quantity. Note that this value can be negative for negatively correlated quantities, but in Figure 3.11c, all quantities are positively correlated. Here the correlation between particle volume and contact force magnitude is made completely clear by showing that the correlation between these quantities is very high once significant breakage initiates at around 5% strain. The correlations also show quantitative evidence of the cushioning effect from volume being correlated to both coordination number and isotropic stress, I_1. The volume is also significantly more correlated to I_1 than the deviatoric stress invariant, J_2, a direct result of a higher coordination number creating a cushioning effect. The correlation of volume to the ratio of σ_1 and σ_c shows that larger particles are generally closer to breakage than smaller ones. The polar plot in Figure 3.11d quantifies the directionality of the contact forces. Bins near 90 or 270 degrees are the sum total of force magnitude in the vertical z direction, while bins near 0 or 180 degrees are the sum total of force magnitude in the radial, r, direction.

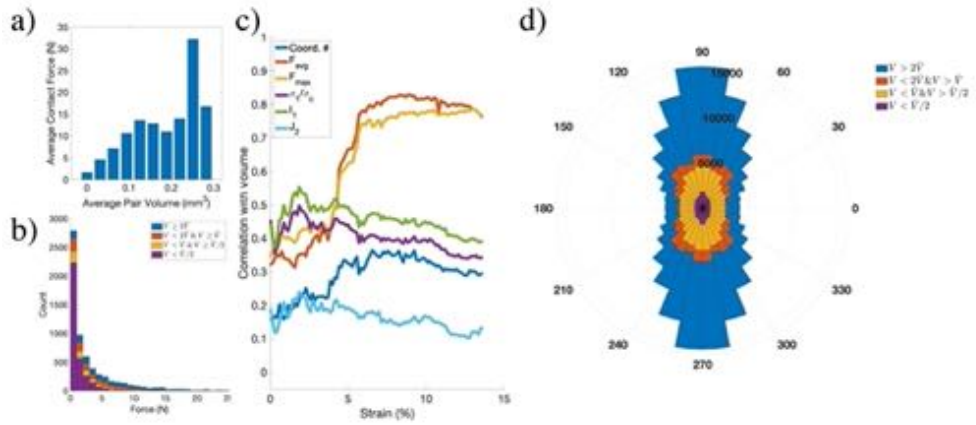

Figure 3.11: Contact force information. (a) Average contact force for each bin of particle volumes. (b) Histogram of all contact force magnitudes separated by volume. (c) Pearson's correlation coefficient for many variables and volume. (d) Polar plot of total force magnitude in each direction. Vertical forces on the plot indicate forces in the z-direction and horizontal indicate forces in the r-direction.

Large amounts of force can be seen in the vertical direction, and significantly less so in the radial direction. The forces are broken up into four bins of average pair volume so it can be observed that the larger particles experience disproportionately more vertical force than radial force. The smaller particles on the other hand, while still experiencing more force in the vertical direction, have a larger relative contribution to the total force in the radial direction than the vertical direction. The small particles then serve as lateral support so that the larger particles can maintain enough confinement to keep the stronger force chains from buckling. The smaller particles still hold significant force near the vertical direction as well however, so these must be the forces that are providing the bulk of the cushioning the larger particles experience.

3.7 Conclusion

The LSDEM with level set splitting in three dimensions has been compared to experiment at multiple scales showing predictive capabilities for both the mechanics and particle shape evolution. The quality of comparisons has provided confidence that investigations into the contact forces and particle stresses using the model can give physically meaningful insight. Observations of the contact forces show the existence of large contact forces on the largest particles. These larger particles were shown to survive due to both a survival of the fittest effect and a cushioning effect, both of which were observed quantitatively. Quantitative analysis of computed contact

forces also pointed out that the emergence of clusters of pervasive crushing leads to a rerouting of major force chains, which in turn shields the affected particles from further breakage. From the directionality of forces for various particle volumes, it was observed that the vertical resistance comes from large forces in the vertical direction on large particles, enabled by the smaller newer particles providing support in the lateral direction. These results, here enabled by DEM simulations allowing realistic particle shape evolution, demonstrate the benefits of integrating full-field measurements and high-fidelity computations to isolate how individual grain properties and collective inter-particle interactions influence the macroscopic crushability of sands.

Chapter 4

MODELING CONNECTED GRANULAR MEDIA: PARTICLE BONDING WITHIN THE LEVEL SET DISCRETE ELEMENT METHOD

Harmon, J.M. et al. (2021). "Modeling connected granular media: Particle bonding within the level set discrete element method". In: *Computer Methods in Applied Mechanics and Engineering* 373, p. 113486. ISSN: 0045-7825. DOI: https://doi.org/10.1016/j.cma.2020.113486. URL: https://www.sciencedirect.com/science/article/pii/S004578252030671X.

4.1 Abstract

Granular materials are made up of particles with complex non-convex shapes that in many cases become connected by cementation, sintering, or other adhesive processes. This paper introduces and describes the methodology behind using the bonded particle method (BPM) with the level set discrete element method (LS-DEM-BPM), in order to model connected granular materials with arbitrary particle shape. The method is thoroughly detailed in both two- and three-dimensions. Examples of use for the method are shown for three distinct contexts. The first is the modeling of a fault gouge, where it is demonstrated that the method has the potential to be predictive of the rate-and-state friction law and have key insights into the micromechanics of the process. Another example is presented where a cone penetrates porous sintered ice showing that bond thickness has a considerable effect on model behavior. The third example is a simulation using many unique bonds for each contact interface, demonstrating the ability to simulate partial fractures. A discussion is also included on how and when this method can be either advantageous or disadvantageous.

4.2 Introduction

Rocks, ices, and metals are among many examples of materials that can be thought of as connected granular materials due to the clear presence of a grain scale that features adhesive mechanisms at grain-to-grain contact locations. For many applications, the physics at the microscale dominate behavior that is observed at the macroscale. To understand the underlying mechanics of these materials, it is important to model the fundamental physics at the grain scale that drives the macroscale observations.

For example, considerable study has been done on the microscale of rock and how it affects the macroscale properties (Grady et al., 1979; Regnet et al., 2019). Small flaws in the rock microstructure can cause large differences in fracture strength. This drives the well-known phenomenon that as rocks get smaller from breakage, their strength increases (Weibull, 1939). The microstructure of ice is also often granular when many ice particles sinter together during formation (Hobbs et al., 1964). The sintering process causes the strength of ice to be dependent on the thickness of the sintered neck, which in itself is dependent on time, temperature, humidity, and initial particle shapes (Christmann et al., 2015).

The bonded particle method (BPM) has been used in discrete element modeling (DEM) extensively since its introduction by Potyondy & Cundall to model connected granular matter (Potyondy et al., 2004). Particle bonding was originally done with spheres that were bonded by beams connecting the centers of the particles that behave linearly. Progress on the model has usually taken the form of enriching the linear bonding mechanics such as with non-local considerations or by improving shape capabilities (Celigueta et al., 2017; M. A. Celigueta et al., 2020). Using spheres assumed that if the spheres were small enough compared to the macrostructure, that their mechanical response would replicate the granular microstructure of a cemented material. This assumption showed to be effective for simulating aspects of crack propagation in rock (Zhang et al., 2011). This principle is also used for simulating breakage in sand where every particle is made of many small spheres bonded together during oedometer testing (Cheng et al., 2003; Cil et al., 2012).

Further developments in both DEM and BPM led to using the bonded particle method in polyheron-shaped particles. This was an important development since many studies have shown the importance of particle shape in granular materials (Kawamoto et al., 2018b; Imseeh et al., 2018). The polyhedron-based method proved effective for simulating the breakage of rock (Galindo-Torres et al., 2012). This also had important implications for masonry as the shape for bricks could be properly represented (Lemos, 2007).

In this paper, the bonded particle model will be implemented with the level set variant of DEM (LS-DEM) for the first time. LS-DEM has key advantages compared to other DEM variants (Kawamoto et al., 2016). The most notable is the ability to capture any arbitrary shape for particles without limitations or special treatments. This has allowed the study of granular specimens through a true one-to-one comparison with experiment by utilizing exact shape for every particle from X-Ray Computed

Tomography (XRCT) imaging (Vlahinić et al., 2014). Validation experiments have provided unique levels of confidence in the method which allows for numerical experimentation beyond what is capable in a lab (Li et al., 2019; Kawamoto et al., 2018b). These advantages could often be of interest to applications for the bonded particle model.

This paper is organized as follows. First the model will be described for both two and three dimensions detailing both LS-DEM and bonding where the simple linear version will be used. Three separate examples will be shown, each highlighting advantages to using the LS-DEM variant of the bonded particle method. Finally, we will conclude with a discussion over both the advantages and disadvantages with the model.

4.3 Modeling Methodology

Level Set Discrete Element Method

LS-DEM is a discrete element modeling variant that utilizes discrete level sets and a surface point discretization for representing particle shape through a leader-follower relationship. Level set functions were developed to define object surfaces implicitly (Sethian, 1999). Discrete level set functions, ϕ, determine the distance, δ, to an object surface given a location, $\vec{x}$, where positive values are outside the surface and negative values are inside the surface. In this way, the morphologies are implicitly defined as the surface can be found through interpolation at the zero level set. Then using a set of surface points, contact is established when the location of a surface point from a leader particle returns a negative level set value from the follower particle (Figure 4.1). Like in other DEM variants, this necessitates a small overlap between particles to occur to determine contact with an assumption made that the overlap is too small to affect results.

The surface normal vector is then determined by taking the gradient of the level set function at that point,

$$\nabla\phi(\mathbf{x}) = \hat{\mathbf{n}} \tag{4.1}$$

Both the overlap and surface normal is used to get contact force through a force-displacement relationship-based contact model. No contact model is specific to LS-DEM, however it is important to consider that contact force is heavily determined by the local curvatures of the contacting surfaces. Hertzian contact is often used in other DEM variants, however this model is only accurate for spheres (Johnson, 1985). Due to the high variety of possible contacting curvatures, a linear model

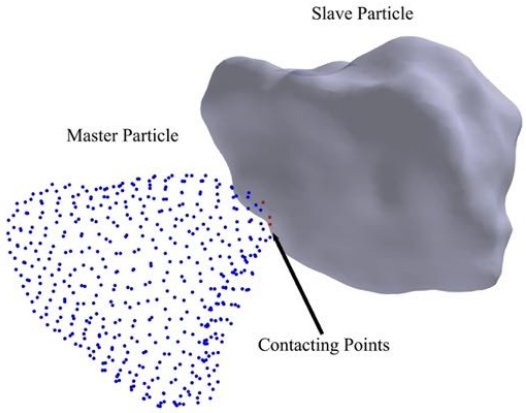

Figure 4.1: Illustration of LS-DEM contact. Red surface points are inside the follower particle and are therefore considered in contact.

will be used with the assumption that having enough contacts will average out the error. The linear model has been shown many times to give reasonable results for LS-DEM (Kawamoto et al., 2016). Both normal and pre-slip shear forces use the linear model,

$$\mathbf{F}_n = k_n \delta_n \hat{\mathbf{n}} \tag{4.2}$$

$$\Delta\mathbf{F}_s = k_s v_s \Delta t \, \hat{\mathbf{s}} \tag{4.3}$$

where k_n and k_s are the normal and shear stiffnesses, respectively, v_s is the relative velocity in the shear direction between contact points, and Δt is the timestep. Using Coulomb friction, the shear force has a maximum value which allows slip,

$$\mathbf{F}_s^{max} = \mu ||F_n|| \tag{4.4}$$

where μ is the static friction coefficient. Due to the frictional aspect being history dependent, shear forces use an incremental approach. Moment is calculated by crossing the total contact force with the vector pointing from the center of mass of the particle to the contact point, $\vec{\mathbf{c}}$,

$$\mathbf{M} = \vec{\mathbf{c}} \times \mathbf{F} \tag{4.5}$$

Once forces and moments are found, the kinematics are calculated using Newton's laws and a global damping formulation. Global damping, which is controlled by the global damping parameter, ξ, is applied as described in Lim et al. (Lim et al., 2014) for both translational motion,

$$v^{n+1/2} = \frac{1}{1 + \xi \Delta t/2} \left[(1 - \xi \Delta t/2) v^{n-1/2} + \frac{\Delta t}{m} F \right] \tag{4.6}$$

and also rotational motion, which uses an iterative predictor-corrector procedure to converge to the correct angular velocities. The algorithm is described in full in Lim et al. and is an integration of Euler's equations of motion with inertia proportional damping,

$$\alpha_1 = [M_1 + \omega_2\omega_3(I_2 - I_3) - \xi I_1\omega_1]/I_1 \tag{4.7}$$

$$\alpha_2 = [M_2 + \omega_3\omega_1(I_3 - I_1) - \xi I_2\omega_1]/I_2 \tag{4.8}$$

$$\alpha_3 = [M_3 + \omega_1\omega_2(I_1 - I_2) - \xi I_3\omega_1]/I_3 \tag{4.9}$$

Global damping is not always added for DEM simulations, but is often useful. The explicit time integration used in DEM often commands the use of small time steps and therefore higher rates of forcing to maintain reasonable simulation durations (Walton et al., 1993; Lim et al., 2014). The global damping alleviates the dynamic errors introduced by maintaining quasi-static conditions.

Bonding Model

Particle bonding models in DEM can usually be described within two different types which have been termed the parallel bonding model and the contact bonding model when introduced (Potyondy et al., 2004). In LS-DEM-BPM, both of these variants may be implemented as shown in Figure 4.2.

The parallel bonding model connects contact points with a bond that resists relative motion and relative rotation. Bonding points are determined at the initialization step of the simulation by searching for nearby particles. In LS-DEM-BPM, this is done in a manner similar to contact where two particles are bonded if a surface point of a leader particle is within a maximum bonding distance of the surface of the follower particle. This is determined by evaluating the follower particle's level set function at the leader particle's surface point location. This maximum bonding distance is set by the user and is termed the cohesive distance, d_c. For the case of parallel bonding, only the surface point that returns the smallest level set value from the follower particle is used.

The contact bonding model is similar to the parallel bonding model except the bonds have infinitesimal thickness and therefore do not resist rotation. A clear use for this in LS-DEM-BPM is by allowing many contact bonds per particle pair that together can resist rotation while simultaneously allowing for the bond to not necessarily break all at once.

While in this paper the linear method will be used for both parallel and contact bonding, neither are limited by this. Non-local methods have shown to provide accurate results and can be implemented by modifying the model similarly to the studies where it was implemented with spheres (Celigueta et al., 2017; M. A. Celigueta et al., 2020).

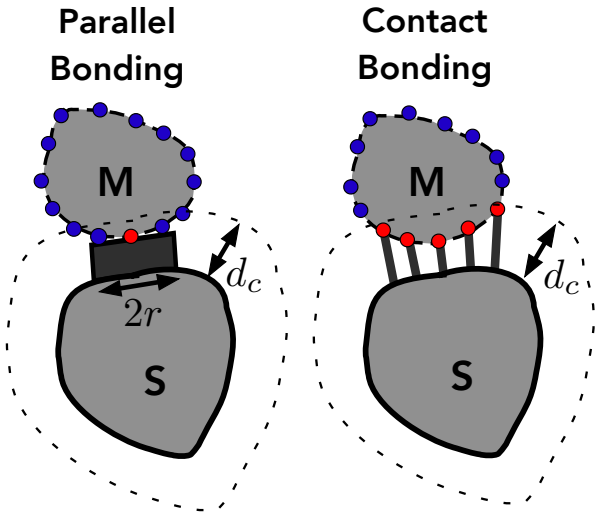

Figure 4.2: Sketch in 2D of each bonding model for a single leader-follower bond pair. Note that for parallel bonding, only the closest point is used to make a bond while for contact bonding, all points closer than d_c are used.

Bonding Mechanics

Each parallel bond is made with a defined radius, r, that defines the cross-section of a cylindrical beam that connects the bond points. Circular cross sections are used because they bear the closest resemblance in shape to a sinter neck, adhesive, or any other bonding agent. This radius is used to compute the bond area, $\bar{A}$, and moment of inertiae for both the rolling, $\bar{I}$, and twisting, $\bar{J}$, axes of motion,

$$\bar{A} = \begin{cases} 2rt, & t = 1, 2D \\ \pi r^2, & 3D \end{cases} \quad \bar{I} = \begin{cases} \frac{2}{3}r^3 t, & t = 1, 2D \\ \frac{1}{4}\pi r^4, & 3D \end{cases} \quad \bar{J} = \begin{cases} \frac{1}{2}\pi r^4, & 3D \end{cases} \tag{4.10}$$

The bar above variables in this section identify variables as pertaining to bonding characteristics, for example $\bar{I}$ is the moment of inertia for the bond and I is the moment of inertia for a particle. Bonds act on particles through a force displacement relationship and a moment angle relationship calculated incrementally in both the

normal and shear directions.

$$\Delta\bar{F}_n = \bar{k}_n\bar{A}\, v^p_{rel,n}\Delta t \tag{4.11}$$

$$\Delta\bar{F}_s = \bar{k}_s\bar{A}\, v^p_{rel,s}\Delta t \tag{4.12}$$

$$\Delta\bar{M}_n = \bar{k}_s\bar{J}\omega_{rel,n}\Delta t \tag{4.13}$$

$$\Delta\bar{M}_s = \bar{k}_n\bar{I}\omega_{rel,s}\Delta t \tag{4.14}$$

where the total force and moment from the bond can be computed by adding the normal and shear components

$$\bar{\mathbf{F}} = \bar{F}_n\hat{\mathbf{n}} + \bar{F}_s\hat{\mathbf{s}} \tag{4.15}$$

$$\bar{\mathbf{M}} = \bar{M}_n\hat{\mathbf{n}} + \bar{M}_s\hat{\mathbf{s}} \tag{4.16}$$

The variables $\bar{k}_n$ and $\bar{k}_s$ are the stiffnesses in both the normal and shear directions for the bond. The normal stiffness can be understood by considering the elasticity of the adhesive agent. Suppose a bonding agent has a Young's modulus, $\bar{E}$, then the stiffness could be calculated from knowledge of the cylindrical geometry of the bond. Here the area we have just determined and the length is approximately the cohesive distance used as our search area to determine bonding,

$$\bar{k}_n = \frac{\bar{E}\bar{A}}{d_c} \tag{4.17}$$

The shear stiffness can be similarly understood with the shear modulus, $\bar{G}$, or more often is set as a ratio between the shear stiffness and the normal stiffness.

The bonds are allowed to break, which is determined by stresses computed using the following beam equations,

$$\bar{\sigma}_c > \bar{\sigma} = \frac{\bar{F}_n}{\bar{A}} + \frac{|\bar{M}_s|r}{\bar{I}} \tag{4.18}$$

$$\bar{\tau}_c > \bar{\tau} = \frac{|\bar{F}_s|}{\bar{A}} + \frac{|\bar{M}_n|r}{\bar{J}} \tag{4.19}$$

Bond breakage occurs when the total stress in the beams exceed a breakage stress. When a bond breaks, the bond is eliminated from the model and therefore does not produce any further forces or moments.

For the case of using contact bonding, there is no concept of bond thickness or moment resistance which simplifies the bond force equations to

$$\Delta\bar{F}_n = \bar{k}_n\, v^p_{rel,n}\Delta t \tag{4.20}$$

$$\Delta \bar{F}_s = \bar{k}_s \, v^p_{rel,s} \Delta t \tag{4.21}$$

Note that the bond stiffness is different here than in parallel bonding. The two definitions of bond stiffness can be related to each other in the following way,

$$\bar{k}_n^{contact} = \frac{\bar{k}_n^{parallel} \bar{A}}{\bar{n}} \tag{4.22}$$

where $\bar{n}$ is the number of contact bonds for the interface. The breakage condition is also simplified to being a critical breakage force rather than a breakage stress.

$$\bar{F}_{n,c} > \bar{F}_n \tag{4.23}$$

$$\bar{F}_{s,c} > \bar{F}_s \tag{4.24}$$

The critical breakage forces can still be determined by breakage stress, however with knowledge of the discretization density of the surface points per unit surface area, ρ_p,

$$\bar{F}_{n,c} = \frac{\bar{n}\bar{\sigma}_c}{\rho_p} \tag{4.25}$$

$$\bar{F}_{s,c} = \frac{\bar{n}\bar{\tau}_c}{\rho_p} \tag{4.26}$$

Bond Damping

Without damping in the model, the bond forces will oscillate which would cause premature breakages and instability. For many applications, particularly for quasi-static tests, global damping is enough to remove these oscillations. Applications with more dynamic interaction prefer to not use global damping however, which requires an ability to dampen bond motion locally. The goal of local bond damping is for both the translational and rotational motion of the bonded contact to be critically damped so that the stress in the bond is equilibrated at the fastest rate.

For translational motion, the normal equation for critical damping in a one degree of freedom system is used,

$$\bar{F}^{damp} = v_n \left[2\sqrt{\bar{k}_n \bar{A} m^{eq}} \right] - v_s \left[2\sqrt{\bar{k}_s \bar{A} m^{eq}} \right] \tag{4.27}$$

where the first term controls the damping in the normal direction to the surface of the particles and the second controls damping in the shear direction. The term m_{eq} is the equivalent mass computed from the masses of each bonded particle,

$$m_{eq} = \frac{m^{(1)} m^{(2)}}{m^{(1)} + m^{(2)}} \tag{4.28}$$

Rotations are considered similarly,

$$\bar{M}^{damp} = \omega_n \left[2\sqrt{\bar{k}_s \bar{J} I_n^{eq}} \right] + \omega_s \left[2\sqrt{\bar{k}_n \bar{I} I_s^{eq}} \right] \tag{4.29}$$

where I_n^{eq} and I_s^{eq} are the normal and shear equivalent moments of inertia calculated from the normal and shear moments of inertia from each particle at the point of bonding. For example in the normal direction, I_n^{eq} can be calculated as,

$$I_n^{eq} = \frac{I_n^{(1)} I_n^{(2)}}{I_n^{(1)} + I_n^{(2)}} \tag{4.30}$$

and the normal moment of inertia can be found from the parallel axis theorem being applied to the scalar moment of inertia about the normal axis which is determined from the particle's moment of inertia tensor,

$$I_n = (\hat{\mathbf{n}} \cdot \mathbf{I})\hat{\mathbf{n}} + m||c||^2 \tag{4.31}$$

In the case of contact damping, the damping moment is unused and the same equation for damping force can be used with just a simple change to the stiffness aspect,

$$\bar{F}^{damp} = v_n \left[2\sqrt{\bar{k}_n m^{eq}} \right] - v_s \left[2\sqrt{\bar{k}_s m^{eq}} \right] \tag{4.32}$$

In general it is recommended that either global damping or bond damping is used since applying both can easily over-damp the system and therefore get inaccurate results from bond forces being unable to reach equilibrium. In cases of low global damping though, the bond damping force can still be applied, but may need to be scaled down for achieving the best results.

By combining this section with the previous two, the mathematics for calculating forces and moments can be understood. To illustrate how all the mechanics come together in implementation, a pseudocode is shown below for calculating contact and bonding for a single particle pair.

Algorithm 1 Calculate forces and moments

for all particle pairs $\{i, j\} \leftarrow \{leader, follower\}$ **do**
  for all surface points of leader particle, p_i **do**
    if surface point and follower particle have intact bond **then**
      {Get Bond Forces and Moments} $\bar{F}_n$,$\bar{F}_s$,$\bar{M}_n$,$\bar{M}_s$ $\leftarrow$ eq. 4.11, 4.12, 4.13, 4.14
      {Check for Breakage} $\bar{\sigma}$, $\bar{\tau}$ $\leftarrow$ eq. 4.18, 4.19
      if eq. 4.18 & 4.19 **false then**
        Set bond to broken
      else
        {Apply Damping} $\bar{F}^{damp}$, $\bar{M}^{damp}$ $\leftarrow$ eq. 4.27, 4.29
      end if
    else if $\phi_j(p_i) < 0$ **then**
      {Get Contact Surface} $\hat{\mathbf{n}}, \hat{\mathbf{s}} \leftarrow$ eq. 4.1, $\mathbf{v}_s/||\mathbf{v}_s||$
      {Get Forces and Moments} $F_n, F_s, M \leftarrow$ eq. 4.2, 4.3, 4.4, 4.5
    end if
  end for
end for

4.4 Model Behavior for Fault Rupture Tests

In this first application of the proposed methodology, we model the rupture of a fault subjected to compression and shear, and the ensuing formation of a granular gouge. In particular, we focus on modeling the fracture of surface asperities and the deterioration of cementation at the grain scale, and we identify their effect on the macroscopic friction. A plethora of experimental studies have focused on delineating this macroscopic frictional behavior for a natural or model fault (Morrow et al., 1989; Marone et al., 1990; Rubino V. et al., 2017), which have inspired a series of theories (Scholz et al., 1972; Ida, 1972) culminating in the development of the rate-and-state framework (Dieterich, 1979; Ruina, 1983). However, these theories remain largely phenomenological given the relative sparsity of micromechanical modeling of these complex grain-scale processes. DEM enhanced with contact aging was employed in (Morgan, 2004) to investigate the frictional behavior of gouge and reproduce several characteristics observed in the laboratory. Further, DEM with bonding was used in (Guo et al., 2008) to study gouge formation under constant-velocity shearing of two surfaces, and in (Fournier et al., 2012), to study the effect of the heterogeneity of the slip surface on the overall characteristics of the slip behavior. In the following, we will present how LS-DEM-BPM can be used to gain further insight into the frictional response of a fault, and we will discuss its implications to rate-and-state theory.

Setup

Figure 4.3a shows an SEM micrograph of a natural gouge, which has been subjected to chemical healing processes, inducing cementation between aggregates (Smith et al., 2015; Keulen et al., 2008). Figure 4.3b shows the idealization of that system within the proposed framework. In particular, we consider a 2D cell comprised of 10,000 angular particles modeled after a quartz sand (Karapiperis et al., 2020a) bonded together. The process of cementation is modeled by parallel bonding neighboring particle surface points that lie within a threshold distance as described in Section 2.2. The properties of particles and cement bonds are reported in Table 4.4. We will further assume that the grains themselves cannot experience fracture, although such an extension is possible within the LS-DEM framework (Harmon et al., 2020).

The cell is first vertically compressed to a pressure σ, allowing for periodic boundary conditions in the x-direction. To impose shear, the upper wall is displaced horizontally, while keeping a constant vertical stress. A preimposed weak interface is introduced in the middle of the specimen, in order to control the initiation of the rupture (Figure 4.3b). The velocity of the upper wall is first kept constant at a value $v_0 = 1$ mm/s until steady state is achieved, and is then instantaneously increased to a value $v_f = 10$ mm/s, until the new steady state is reached (Figure 4.5a). During this process, we measure the evolving population of interparticle bonds as well as the shear stress at the upper boundary, yielding the transient macroscopic friction angle $\mu = \tau/\sigma$.

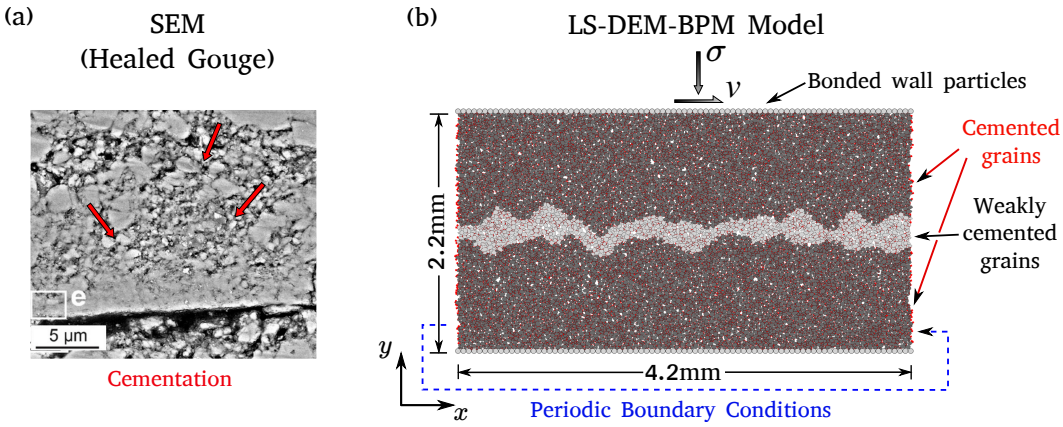

Figure 4.3: Fault gouge. (a) SEM micrograph of a healed gouge adopted from (Smith et al., 2015). Arrows show cohesive bridges (bonds) forming between aggregates, (b) Idealized numerical model of the fault.

Parameter	Value	Units
Density (ρ)	2500	Kg/m^3
Grain Young's modulus (E_g)	70	GPa
Contact stiffness ratio (k_n/k_t)	2	-
Friction coefficient (μ)	0.3	-
Coefficient of restitution (c_r)	0.6	-
Cement Young's modulus ($\bar{E}_c$)	3	GPa
Bond stiffness ratio ($\bar{k}_n/\bar{k}_t$)	2	-
Cement compressive strength ($\bar{\sigma}_c$)	100	MPa
Cement shear modulus ($\bar{\tau}_c$)	100	MPa

Figure 4.4: Particle and cement properties for the LS-DEM-BPM model of the gouge.

Rate-and-state friction law

Before delving into the results of the numerical experiments, we briefly review the standard rate-and-state friction law used to describe these systems. The law relies on the Coulomb assumption with a rate and state dependent friction coefficient $\tau = \mu(v, \theta)\,\sigma$, where v is the slip rate and θ is an internal variable (state) representing history dependence, typically interpreted as the contact lifetime:

$$\mu = \mu_0 + a \log \frac{v}{v_0} + b \log \frac{v_0 \theta}{L} \tag{4.33}$$

where μ_0, v_0 are the reference friction coefficient and reference velocity, respectively, L is a length scale, and a, b are parameters of the model. The evolution of state is described by the aging law (Dieterich, 1979):

$$\dot{\theta} = 1 - \frac{v\theta}{L} \tag{4.34}$$

and can give rise to either velocity strengthening ($a - b > 0$) or velocity weakening ($a - b < 0$). Figure 4.5 demonstrates the evolution of friction in these two cases. For bare slipping surfaces, experimental evidence suggest velocity weakening behavior (Marone et al., 1990). In the presence of gouge, most evidence points to velocity strengthening (Marone et al., 1990), while velocity weakening has also been reported in the literature (Beeler et al., 1996; Ikari et al., 2017), depending on the inertial number (Kuwano et al., 2013; DeGiuli et al., 2017).

Results

Figure 4.6a shows the evolution of macroscopic friction against the fault slip for the same experiment carried out at two different pressures: $\sigma_1 = 1\,\text{MPa}$ and $\sigma_2 = 2\,\text{MPa}$, respectively. Following the initial rupture at the weak interface, both systems arrive

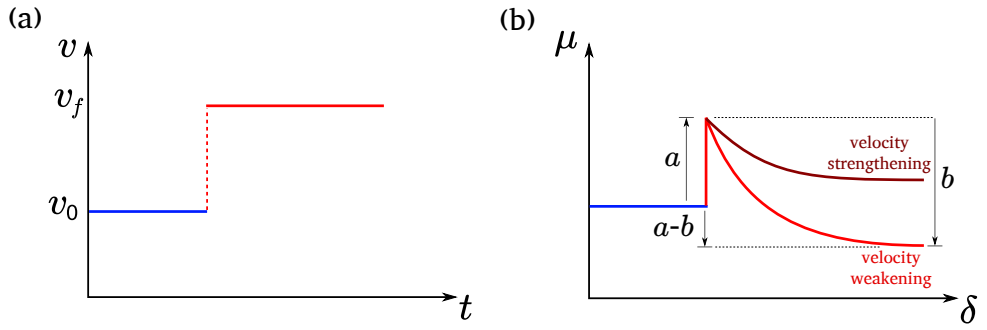

Figure 4.5: Velocity and rate-and-state. (a) Velocity history (b) Rate-and-state friction law.

at a steady state as witnessed by the small fluctuations in friction. These fluctuations represent stick-slip events arising from the repeating formation and collapse of force chains. This is evident in Figure 4.7a, which shows the heterogeneous contact force and bond force chains at that state for the higher pressure experiment. Figure 4.6b shows the rate of bond breaking for the two experiments. After an initially pronounced bond breaking phase, we observe a decrease in the rate of bond breaking towards the first steady state, at a slip of approximately 2 mm.

Upon the imposed sudden increase in the velocity in the second stage of the experiments, we observe a spontaneous increase in friction in line with experimental evidence and rate-and-state theory. This so-called "direct effect" is the signature of an increase in the number of activated contacts. Gradually, the contact network rearranges itself, and force chains appear to localize at the asperities (Figure 4.7a). We observe local fractures at the asperities as a result of these dynamic stress concentrations. This leads to widening of the gouge, and in turn to reduced particle interlocking which reduces macroscopic friction. In Figure 4.6b, we observe that the rate of bond breaking indeed increases in both systems at a slip $>$ 2 mm, only to eventually decay towards a new steady state at a slip $>$ 3 mm. At that point, only a few bonds continue to experience fracture. The widened fault at the final steady state is shown in Figure 4.7b for the lower pressure experiment. The final steady state friction coefficient depends on the pressure, which affects the accumulated damage to the asperities and alters the dynamics of the contacting particles within the weakened zone. In this experiment, we observe that lower pressure leads to rate-strengthening behavior, while a higher pressure leads to minor rate-weakening behavior which is likely due to greater damage at the asperities.

Although no direct comparison with experiments is attempted in this study, this framework exhibits great potential in reproducing the range of behaviors observed in the laboratory. The incorporation of particle morphology ensures that we can accurately account for particle interlocking and rolling, which has been shown to be important for fault gouge modeling (Morgan, 1999). This completely avoids the need for numerical proxies, when approximating the system by idealized shapes such as disks (Morgan, 2004). Further, the incorporation of local (particle surface) bonding ensures an accurate representation of contact scale cementation. Uncovering the complex interplay between the inertial properties of the gouge, and the evolving surface roughness and gouge width (Scholz, 1987), would clearly require a systematic investigation of the parameters of the system. The latter could then shed light on the parameters of the rate-and-state theory, such as the length scale L. The above lie beyond the scope of this application.

(a) (b)

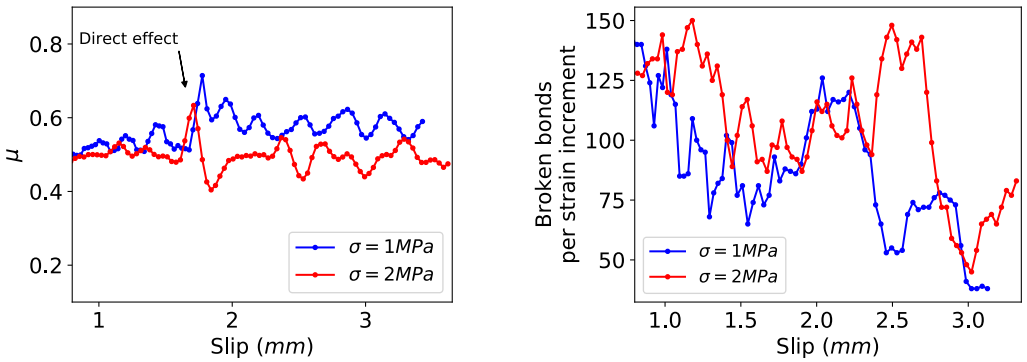

Figure 4.6: Friciton and breakage over slip. (a) Friction as a function of slip (b) Rate of bond breakage (averaged over 1% shear strain increments) as a function of slip.

4.5 Model Behavior for Cone Penetration Tests

This application will study the model behavior during a cone penetration test. Particularly we will look at the effect of sintering neck size on strength. The sintering process is an important aspect for many classes of materials such as metals and ices. Being able to predict the changes in strength with increasing amounts of sintering is highly desirable.

An example of an application where understanding the strength of a sinter network in a granular material is sample acquisition on space missions to icy worlds. NASA has made it a priority to send missions to moons in the solar system with global oceans

(a) (b)

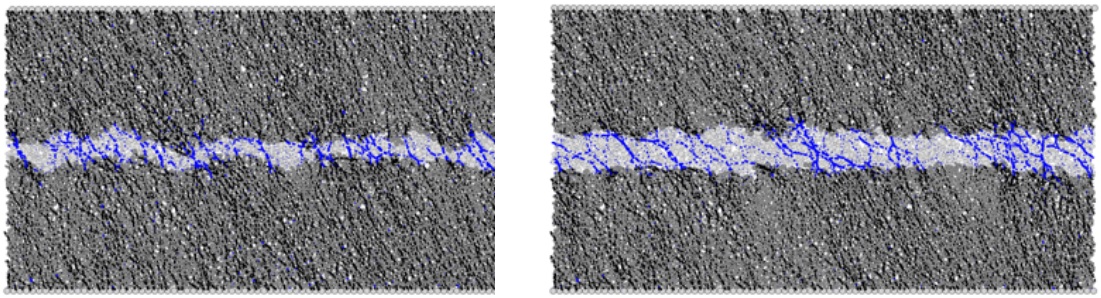

Figure 4.7: Particle configuration with bond force chains (in black) and contact force chains (in blue) for the low pressure experiment for states (a) right before the velocity jump and (b) at the final steady state. Darker particles represent those connected by cement bonds; Lighter particles represented unbonded particles.

such as Europa and Enceladus due to the relatively high probability of finding life (McKay et al., 2014). Due to the very low temperatures and near vacuum conditions, porous ice solidifies at a very slow rate, meaning the planetary surface likely remains quite porous (Molaro et al., 2019). Due to this, large amounts of the surface would correctly be described as a connected granular material. This is particularly true for the most geologically active areas, which are often of highest interest, such as the south pole region of Enceladus. This region has geysers emitting ice particles from the subsurface that either eject into Saturn's E-ring or fall back onto the nearby surface (Tsou et al., 2012). This section is built to be a first attempt at mimicking a metal cone penetrating an icy surface such as Enceladus in this region where ice is granular.

Specimen Preparation

The specimen was prepared by pluviation of particles into a cylindrical container. A set of 100 unique granular geometries were used as particles taken from an XRCT image of Hostun sand. During pluviation, the particles were made slightly larger so that when the specimen is complete, there is empty space where the sintered necks will be. Instead of all the particles being dropped from the beginning, particles were only added when previous particles had settled. Each new set of added particles were placed directly above the specimen, resulting in the particles depositing at a low velocity. This created a loose specimen with a porosity of 46%. Particle parameters used during the pluviation process were the same as during testing and

are shown in Figure 4.8. When bonding the particles, a cohesive distance of $0.5mm$ was used with several neck sizes.

Parameter	Value	Units
Density (ρ)	900	Kg/m^3
Grain Young's modulus (E_g)	9	GPa
Contact stiffness ratio (k_n/k_t)	2	-
Friction coefficient (μ)	0.2	-
Coefficient of restitution (c_r)	0.6	-
Cement Young's modulus ($\bar{E}_c$)	9	GPa
Bond stiffness ratio ($\bar{k}_n/\bar{k}_t$)	2	-
Cement compressive strength ($\bar{\sigma}_c$)	1	MPa
Cement shear modulus ($\bar{\tau}_c$)	1	MPa

Figure 4.8: Particle and cement properties for the LS-DEM-BPM model of the ice specimen.

Cone Penetration Test

The cone penetration test was conducted by descending a cone with a diameter of $1cm$ at a rate of $0.2m/s$ into the ice specimen. Considerable global damping was used to ensure quasi-static conditions despite the relatively high penetration rate. Due to this, no bond damping was necessary for this case. The stress was calculated by adding up the vertical forces on the cone tip and dividing by the cross sectional area of the cone. The test is conducted three times to investigate the effect of the thickness of the sintered neck being represented as bonds. The thickness is set by a ratio between the radius of the sintered neck, r, and the radius of the circumscribed sphere of each particle, R. The three thicknesses tested are $r/R = 0.01$, $r/R = 0.25$ and $r/R = 0.5$. Figure 4.9 shows a visualization of the cone penetrating the ice specimen at various stages of loading for $r/R = 0.5$. During the early stages of the loading, such as in Figures 4.9c and 4.9d where the cone displacement is at $1.5cm$, small cracks near the tip can easily be observed with these cracks causing only local deformation in the area of the cracking. In Figure 4.9d, it can be observed that cracking propagates laterally as the particles are pushed away from the cone center, however the bonds remain intact directly below the tip providing continued resistance. At this time of loading, stress is continuing to build with occasional minor cracks causing only minimal reductions in strength as seen in Figure 4.10. Above a displacement of a little over $2cm$, the specimen experiences heavy brittle fracture for both $r/R = 0.25$ and $r/R = 0.5$. In the visualization in Figure 4.9b, large

displacements and heavy breakage can be easily observed in most of the specimen corresponding to the large stress drop measured.

For the test where $r/R = 0.01$, the very low sintering results in very little resistance which is expected. For this case, the specimen does not experience the same reductions in strength from heavy breakage, but instead has a much more consistent level of resistance as what may be expected from a specimen with no bonding at all.

This model behavior is consistent with trends seen for ice that experiences brittle breakage with the advantage of being able to investigate the micromechanics of the sintered bonds (Schulson, 1999). In future work with modeling strength of sintered particles, it would be advantageous to utilize the shape morphing aspects of the level set method to better represent particles morphologies and different stages of sintering. Level sets are extensively used for tracking shape changes from physical processes (Sethian, 1999). Implementing the many theoretical models that predict sinter growth with the level set evolution methods is a promising avenue for more accurate modeling in the future.

The results for the cone penetration test show the considerable effect the thickness of particle bonds have on the behavior of the model, and therefore the importance of understanding how particles adhere together. A common assumption in BPM is to take the thickness of the bond as the minimum of the thicknesses of the two particles being bonded. This is likely a good assumption for non-porous materials such as rock where the cementation completely surrounds each particle, but probably an insufficient assumption for more porous substances such as ice or metal that has not been fully sintered together.

4.6 Model Behavior for Adhesive Failure

There are many instances where an adhesive agent that is wished to be modeled between particles may not break all at once. In these cases, modeling with a single breakable bond is not ideal since relative rolling between particles should cause failure in only the tensile region of the bond. In order to model these cases, this section proposes to have multiple contact bonds at each contact pair instead of a single parallel bond. Here, an example of this idea is presented with a simple constructed material built to absorb energy. The construction of periodic and lattice structures to tune viscoelastic behavior is common in applications from the nanoscale (Portela et al., 2020) to the macroscale (Maskery et al., 2017). In this study, the choice of structure is a lattice of very stiff spheres bonded with a compliant adhesive.

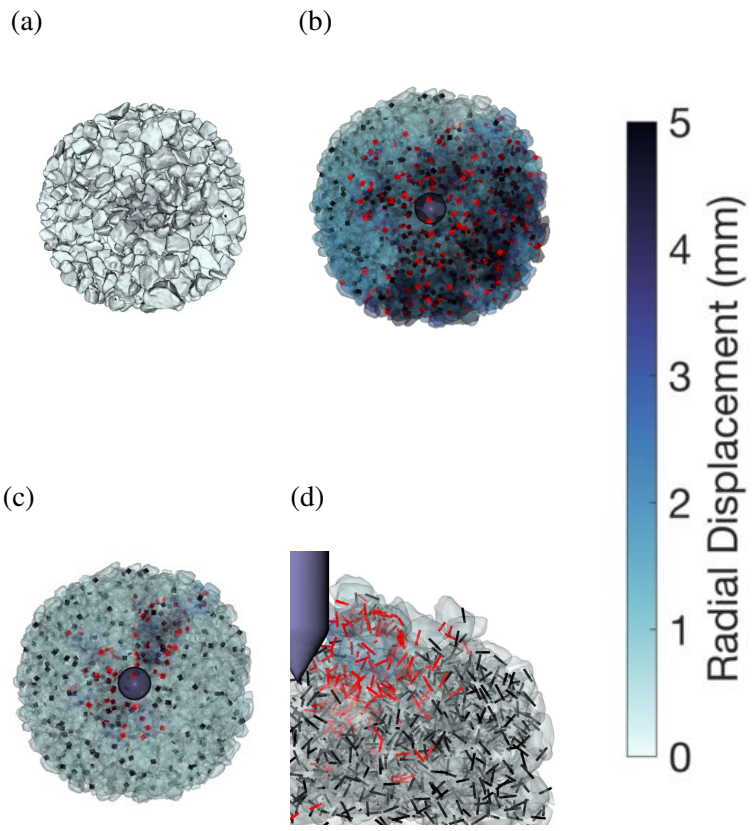

Figure 4.9: Visualization of ice specimen with $r/R = 0.5$. Color indicates the displacement of the particle away from the center of the specimen with darkest color being a displacement of one cone radius. Black lines indicate intact bonds and red lines are broken bonds. (a) Top view of initial specimen. (b) Specimen after complete fracture. (c) Top view at 1.5cm cone displacement. (d) Profile of specimen at 1.5cm cone displacement.

While LS-DEM-BPM could handle any other geometry just as well, spheres show that for this case the utilization of surface points for bonding delivers the advantage of having multiple bonds per particle pair that may be useful enough even for sphere based applications.

Model Setup

A cubical lattice specimen was prepared by placing spheres in a five-by-five grid. Each sphere was allowed to bond only vertically, allowing spheres to move laterally. This was done so that the structure could buckle more easily, therefore increasing its potential for dissipation. Spheres were ordered so that leader particles were placed below follower particles, so therefore bonds are centered at the surface of the bottom particles and directed toward the top particle. The surface points for each sphere

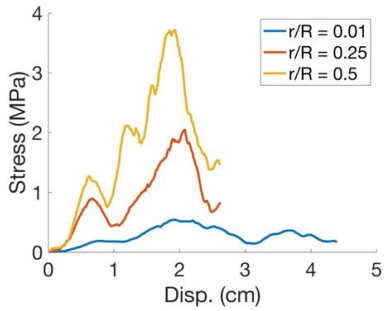

Figure 4.10: Relationship between stress on cone and cone displacement into the specimen for various sinter neck thicknesses. Due to the brittle nature of ice, the cone stress on specimens with thicker bonds falls abruptly at a critical level.

were seeded so that each bond is made of 14 separate and evenly spaced contact bonds. Walls were added to the top and bottom of the specimen with equal stiffness and friction to the spheres. The specimen is shown in Figure 4.12a in the initial state before compression. Whereas normally in LS-DEM a linear contact model is used, for this case a Hertzian contact model is used due to the spherical shapes, changing the force displacement relationship to,

$$F_n = \frac{4}{3} E^* \sqrt{R\delta_n^3} \tag{4.35}$$

Where R is the effective radius which for uniform spherical contact is equal to half the sphere radius and for sphere to wall contact is the equivalent to the sphere radius. The material parameter E^* is defined in the usual way for contact of identical materials,

$$E^* = \frac{E}{2(1-\nu^2)} \tag{4.36}$$

Exact model parameters used are shown in Table 4.11. The value of breakage stress for the bonds in this example was normal distributed across the interfaces which will provide some heterogeneity to the otherwise identical sphere columns.

Model Results

The specimen underwent one full loading and unloading cycle with a peak strain of 20% for each test conducted. Stresses were calculated by dividing the total force on the top wall by the maximum cross sectional area of the structure defined as $A_{struc} = 10R_{sph}$ where R_{sph} is the radius of the spheres. Visualizations of the simulations were rendered to observe bulk behavior in the specimen shown in Figure 4.12. It can first be observed that breakages generally occur in the middle row of bonds, which is sensible since that is the area where the highest stress will naturally

Parameter	Value	Units
Density (ρ)	2650	Kg/m^3
Grain Young's modulus (E^*)	66	GPa
Contact stiffness ratio (k_n/k_t)	2	-
Friction coefficient (μ)	0.1	-
Coefficient of restitution (c_r)	0.6	-
Cement Young's modulus ($\bar{E}_c$)	0.2	MPa
Bond stiffness ratio ($\bar{k}_n/\bar{k}_t$)	2	-
Cement compressive strength ($\bar{\sigma}_c$)	11	MPa
Cement shear modulus ($\bar{\tau}_c$)	11	MPa

Figure 4.11: Particle and cement properties for the LS-DEM-BPM model of the sphere specimen.

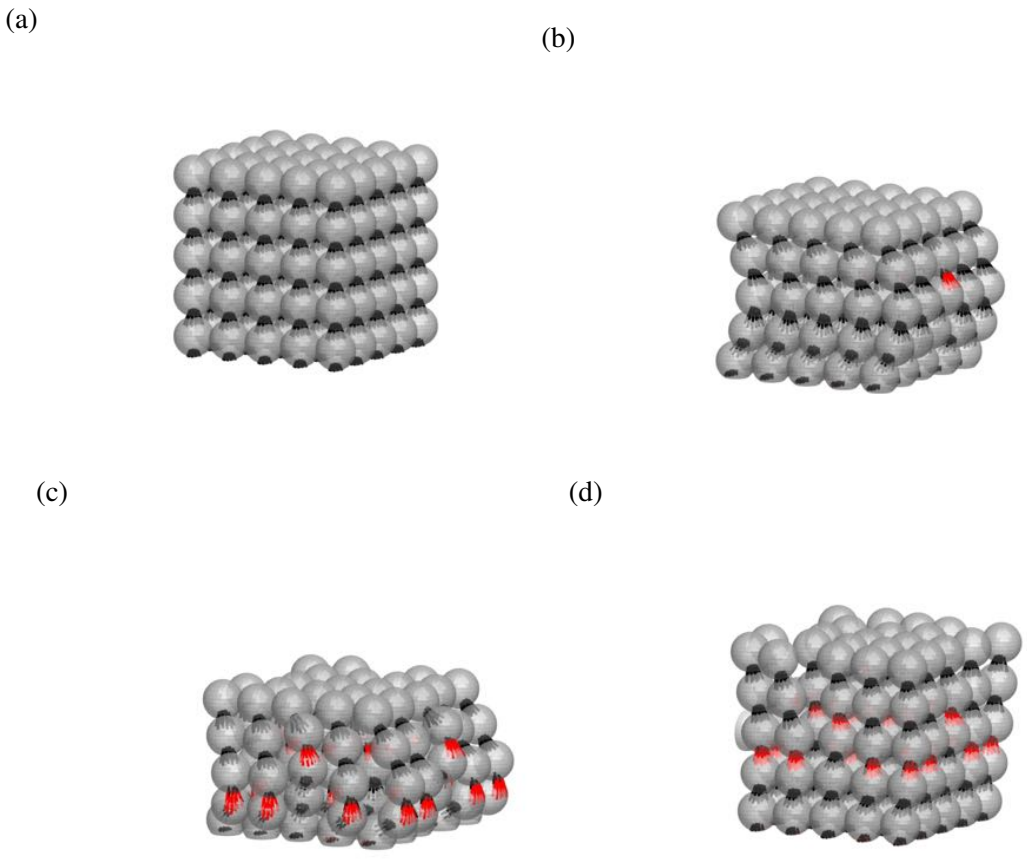

Figure 4.12: Visualization of the compression of spheres bonded with the contact bonding model. (a) Initial state (b) 10% strain (c) 20% strain (d) Fully unloaded.

occur. Bond breakage does however occur outside of the middle row as well to a lesser degree. After unloading, most columns appear to come back to full height,

showing evidence that very high levels of deformation do not injure the ability of the bonding method to recover the initial state.

Constitutive behavior of the specimen can be seen in Figure 4.13. During loading, three distinct phases of behavior can be easily seen for all cases tested. First is the pre-buckling phase where the structure behaves closely to the material behavior of the spheres. The structure then buckles, resulting in nearly constant stress with limited evidence of bond breakages. Finally, considerable bond breakages occur while simulataneously the densification of the spheres create new sphere-to-sphere contacts resulting in higher strength.

Upon unloading, significant hysteresis is observed, the magnitude of which being inversely proportional to the average bond strength as shown in Figure 4.13. Interestingly, the variance of the bond strength has a minor effect as well, where a higher variance in bond strength causes more hysteresis. This can be explained by the fact that higher variance of bond strengths results in more bonds being broken if stresses in the bonds on average remain lower than the average critical stress.

(a) (b)

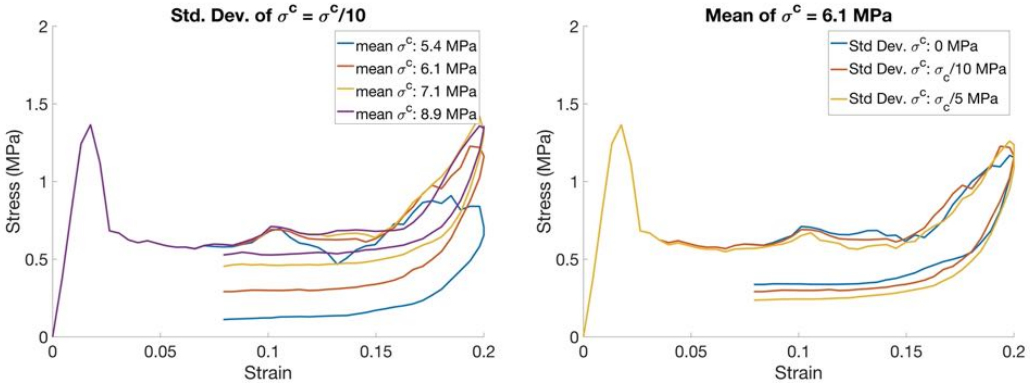

Figure 4.13: The stress vs. strain relationship for various levels of bond strength. Figure (a) shows plot for various mean values for critical stress. Figure (b) shows plot for various standard deviations of critical stress.

4.7 Discussion

The most considerable advantage to using LS-DEM-BPM is the ability to use any arbitrary shape. For a fully bonded granular material, particle shape will affect the fabric of the bonds as it does the fabric of contact forces for an un-bonded granular material. For cases where there are very few fully debonded particles, the polyhedron method could be sufficient since the interlocking effect of concave features may not

play as large of a role as it would for an un-bonded granular material. However, an interesting direction of future work with using level sets will be utilizing images of the microscale for materials such as rock or sintered materials to investigate the importance of grain shape in the material behavior. XRCT and SEM images of the grain-scale for these materials allow access to the true shape characteristics of the grains and grain boundaries. With plenty of research confirming that fractures generally occur along grain boundaries, representing the correct shape for the grains will likely prove to be a key aspect for using BPM for such applications (Eberhardt et al., 1999).

The advantage of arbitrary shape becomes even more pronounced in applications such as the fault gouge where the material behavior beyond the breakage of bonds is important. Once particles have broken all of their bonds, those particles will behave as an unbonded granular material. The importance of particle shape in an unbonded granular material is well documented (Guo et al., 2015) and has been the driving reason for many DEM variants attempting to define shape in general ways (Mollon et al., 2014). Especially for the fault gouge where shear is the driving mechanism for deformation, the correct particle shape is critical as it has the largest effects on the predictions for shear (Herbst et al., 2004).

The most significant disadvantage with LS-DEM-BPM continues to be the efficiency of the method. Some applications ask for the simulation of millions of particles, and while this is certainly possible with LS-DEM-BPM, it is unfeasible without large computational resources. New developments in efficiency with LS-DEM such as using octree methods may prove to alleviate though not completely solve this issue (Duriez et al., 2020). Until the new generations of computer processors or the implementation of LS-DEM with GPU parallelization, LS-DEM is limited to particle numbers on the order of $< 10^6$ particles. This limitation is important for applications where a granular specimen must interact with large objects, however studies for even these cases will often show that there are diminishing returns for using smaller and smaller particles (Catanoso et al., 2020). For cases where the goal of the modeling is to investigate the material behavior by using a representative volume element, this limitation is less important as many studies have shown success at replicating experiments with much fewer particles (Froiio et al., 2010).

4.8 Conclusion

The implementation of the bonded particle method with the level set discrete element method has been introduced. This allows the bonded particle method to be utilized with a DEM method that allows for arbitrary particle shape. Examples of possible applications of this method have been shown. The fault gouge example demonstrated the capability of the method to model a fault gauge and the rate-state friction model. This example highlighted the potential for this model in applications where the unbonded granular materials plays a significant role. Further, an example of a cone penetrometer fracturing ice demonstrated the effects of bond thickness on the model behavior and showed that it is significant. The third example showed the potential for a modeling strategy where each particle pair may have many bonds that do not necessarily break all at once. This strategy allows for crack growth within each particle bond and correctly weakens only the bonding region where tensile forces were present. Finally a discussion highlighted the advantages of particle shape despite drawbacks in efficiency. This procedure could open doors to new knowledge of materials that can be defined as a connected granular material.

Chapter 5

MODELING BREAKAGE MECHANICS OF GRANULAR ICE ANALOGS FOR ICY BODY SPACECRAFT INTERACTIONS

Harmon, J.M. et al. (2021). "Modeling breakage mechanics of granular ice analogs for icy body spacecraft interactions". In: *Journal of Terramechanics (submitted)*.

5.1 Abstract

For successful surface operations on planetary bodies where granular sintered ice is present, the mechanics of the ice must be understood for spacecraft engineering and the formulation of a mission's science objectives. In this paper, granular sintered ice is modeled as interconnected ice particles with particle shapes determined from a laboratory ice simulant imaged by a 3D x-ray computed tomography. The shapes are numerically modeled using individual level set functions for each particle, and the mechanics are modeled with the discrete element method. The sintered structure is modeled using an interparticle bonding method that allows for breakage. Cone penetration testing is modeled and compared to physical experiments. Comparisons show that the model can produce similar stresses and qualitative features observed in the experiment. A sensitivity analysis is conducted and shows that the most important controlling parameters are the ice's critical strength and the sinter neck thickness. The relation of the bond characteristics to the sintering process is discussed.

5.2 Introduction

Icy bodies in the solar system such as Enceladus and Europa are scientific targets of interest (Howell et al., 2020) due to the potential of finding life in these locations (Chyba, 2000; Postberg et al., 2018). As such, there is a desire to understand more about the mechanics of the ice the bodies are made of. The mechanics of any surface materials, particularly its stiffness and strength, are a key factor in the surface and subsurface acquisition of samples since the sampler must be designed with certain mechanical properties of the surface in mind. This lesson was learned acutely when the Insight lander mole, HP3, was designed for largely unknown mechanical properties of the regolith at its landing site (Spohn et al., 2018). In another recent mission, the sample acquisition expectations on Bennu were largely dependent on

the previously unknown cohesive strength of the soil, which needed to be weak enough to be gathered with nitrogen gas (Bierhaus et al., 2021).

The surface of icy bodies present a unique challenge when the ice is porous due to the ability of ice particles to sinter over time, creating large changes in strength (Choukroun et al., 2020). The ice on these bodies can be thought of as a connected granular material where individual ice particles are connected through sintering (Molaro et al., 2019). This type of ice is far from uncommon in the solar system. For example, on Enceladus the plumes on the south pole eject ice particles that deposit on the surface and sinter over time (Verbiscer et al., 2018). A highly porous but cohesive granular microstructure exists due to the low sintering rates (Choukroun et al., 2020). On Europa and Triton, recent image analysis points to a high probability of porous granular ice (Eluszkiewicz, 1991; Carlson et al., 2009). Many smaller bodies have a mixture of ice and regolith which can result in similar densification as from pure ice (Campins et al., 2010).

Due to the connected granular nature, it is expected that the mechanics at the particle scale drives the behavior at the macroscale. Figure 5.1a shows an image of an ice microstructure similar to what is expected on icy bodies and an image of a concrete microstructure that is currently used as a simulant for ice (Badescu et al., 2019). At this scale, distinct particles can be easily distinguished with clearly visible sinters that are likely locations of stress concentration under loading. Treating these materials as a collection of connected discrete elements provides an ability to understand the mechanics from the microscale. This has been true for many other connected granular materials such as concrete, rock, and metals in additive manufacturing (Suchorzewski et al., 2018; Kazerani et al., 2010; Xiang et al., 2016). For this reason, it is desirable to use discrete element modeling (DEM) with particle bonding so the micromechanics can be modeled directly as in other materials (Lisjak et al., 2014; Cundall et al., 1979).

DEM is a modeling technique that directly simulates the motion of individual particles in a granular material. The level set variant (LS-DEM) will be used since it can efficiently model any arbitrary particle shape, something that other methods are unable to do. An important innovation in DEM is the addition of the Bonded Particle Method (BPM) (Potyondy et al., 2004). BPM models adhering mechanisms, such as cementation or sintering, with a stiff beam that connects the bonded interfaces. This enables the modeling of sintered ice by creating the ability to physically represent the sinter connection between ice particles. (Harmon et al., 2021) recently developed an

implementation of BPM in LS-DEM, which is what is used in this paper. This study will be the first comparison of the pairing of LS-DEM and BPM (LS-DEM-BPM) with experimental results.

5.3 Relevant Ice Microstructure

The type of ice we aim to understand with this model is porous ice composed of identifiable particles. We define the micro-scale of this ice as where the identifiable ice particles interact, such as in Figure 5.1a. The microstructure of this ice may range from a collection of discrete particles connected only through friction and contact forces to more consolidated ice aggregates that have undergone considerable modification from sintering. The sintering process is a frost metamorphism that is driven by surface and volume diffusion resulting in the growth of the ice particle contact area and densification. The contact area growth is what is referred to as the sinter neck. While this paper only looks at ice that has undergone some level of sintering, for cases where sintering has yet to occur this can be understood as a special case of an infinitely small sinter. The mechanics of porous, sintered ice heavily depend on microscale features such as particle shape, size, and sinter neck growth (Christmann et al., 2015). At later stages of densification, individual ice particles become less identifiable as the ice approaches a continuous solid. While many versions of the bonded particle method have been proven to be effective for continuous solids such as rock (Lisjak et al., 2014), the nature of solidified microstructures are not as analogous to the mechanics of the model.

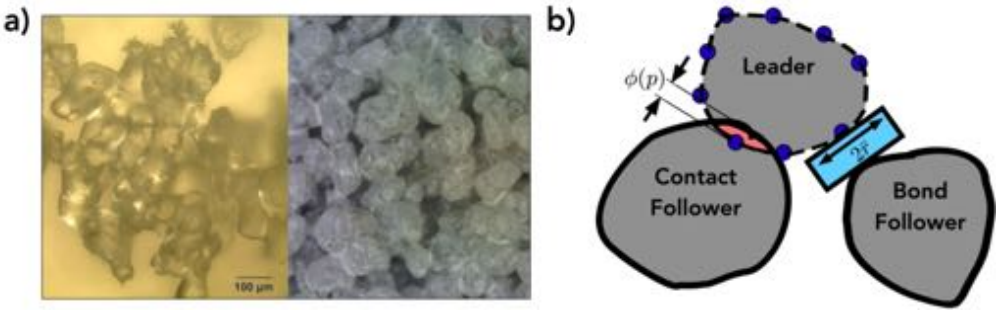

Figure 5.1: (a) Image of laboratory sintered ice (left) and concrete ice simulant (right) taken from (Badescu et al., 2019). (b) Sketch for both contact and bonding model.

5.4 Model Description

The sinters between ice particles are modeled using beams connecting the surfaces that sinter together. The intention of representing ice particle sinters with bonds

can be directly visualized between Figure 5.1a and Figure 5.1b where the bond connecting the leader particle and bond follower particle is meant to directly model the visible connections between the imaged particles. LS-DEM uses a leader-follower algorithm for detecting contact and enabling bonding as shown in Figure 5.1b. The complete and detailed description of the method is described in Harmon et al. ((Harmon et al., 2021) and a summary will be provided here.

For this algorithm, a leader particle may be connected to follower particles via either a contact or a bond. While at the initial state, all interparticle interactions are bonds, as bonds break, their subsequent interactions are frictional contacts. For a contact follower, the leader particle checks whether each surface point is either inside or outside the follower particle's surface. Level set functions, $\phi(x)$, for a given particle take a location in space as input then output the distance of that location, d, to the particle surface where positive values are outside the particle and negative values are inside.

$$\phi(x) = \pm d \tag{5.1}$$

The contact normal force, F_n, is calculated by using a linear relation determined by the level set, ϕ, and the surface point, p_i, where k_n is the stiffness of the spring and $\hat{n}$ is the contact normal unit vector.

$$F_n = k_n \phi(p_i)\hat{n} \tag{5.2}$$

The contact shear force uses an incremental approach where the shear force increment, ΔF_s, is determined from the relative velocities of the particles in the shear direction at the point of contact, v_s, where k_s is the shear stiffness, Δt is the time step, and $\hat{s}$ is the shear unit vector.

$$\Delta F_s = k_s v_s \Delta t \hat{s} \tag{5.3}$$

Coulomb friction is used and is implemented by setting a maximum value for the shear force, F_s^max, where μ is the friction coefficient.

$$F_s^{max} = \mu F_n \tag{5.4}$$

If the surface point contains a bond such as the representation of a sintering neck, then the bonding algorithm and bonding equations are used instead of the contact equations. Particles that are bonded are allowed relative motion, but that motion is resisted by a linear relation.

$$\Delta\bar{F}_n = \bar{k}_n\bar{A}v_n\Delta t \tag{5.5}$$

$$\Delta\bar{F}_s = \bar{k}_s\bar{A}v_s\Delta t \tag{5.6}$$

$$\Delta\bar{M}_n = \bar{k}_s\bar{J}\omega_n\Delta t \tag{5.7}$$

$$\Delta\bar{M}_s = \bar{k}_n\bar{I}\omega_s\Delta t \tag{5.8}$$

The bar above the variables denotes that the variable is bonding specific, for example the bonding stiffnesses, $\bar{k}_n$ and $\bar{k}_s$, are distinct from the contact stiffnesses. Unlike contacts which act as point loads, bonds act over a circular cross-sectional area to resemble ice sintering necks. This area can be defined with neck radius, $\bar{r}$, which allows for the calculation of the area, $\bar{A}$, rolling moment of inertia, $\bar{I}$, and twisting moment of inertia, $\bar{J}$, which are the same as a beam with a circular cross section as an idealized representation of a sinter neck cross sectional area. The stresses inside the bond are evaluated every time step using beam equations where $\bar{\sigma}$ is the normal stress and $\bar{\tau}$ is the shear stress.

$$\bar{\sigma} = \frac{\bar{F}_n}{\bar{A}} + \frac{|\bar{M}_s|\bar{r}}{\bar{I}} \tag{5.9}$$

$$\bar{\tau} = \frac{\bar{F}_s}{\bar{A}} + \frac{|\bar{M}_n|\bar{r}}{\bar{J}} \tag{5.10}$$

If either the normal or shear stress exceed a critical value, which is set to the tensile strength of non-porous ice, then the bond breaks and the bond forces no longer act on either particle.

With forces calculated for both contact and bonding, motion can then be determined from Newton's Laws and kinematics. The model uses an explicit integration scheme in time described in (Lim et al., 2014) where motion is determined directly from spring forces as opposed to using an optimization strategy. The explicit method encourages the use of some damping to remove oscillations. Damping is also helpful to allow for faster loading rates and therefore lower compute times while maintaining quasi-static conditions. The damping strategy used is to apply dampers in parallel to the springs used for both contact and bonding. A complete description of the damping method is also described in (Harmon et al., 2021).

5.5 Particle Characterization

LS-DEM uses the complex shape of real particles that can be determined either from x-ray CT imaging, CAD modeling, or through level set evolution algorithms (Vlahinić et al., 2014; Osher et al., 2006). For missions to icy planetary bodies, performing 3D imaging in situ is infeasible and samples are still unavailable, therefore simulants are used to model the material. A material analog that has been used for planetary surface sampling development to simulate sintered granular ice is highly porous concrete, sometimes referred to as pervious concrete (Badescu et al., 2019). Concrete is also granular in nature where the paste that holds concrete together can be thought of as mechanically similar to the sintered connections that hold porous ice together. Concrete has the added benefit of already being studied extensively with BPM e.g.(Nitka et al., 2015).

The concrete imaged is Ordinary Portland Cement (OPC), ASTM C150 Type I/II. The mixture has a water-to-cement ratio of 0.6 and is 60% voids. The aggregate is Minex 3 and the concrete is 15% paste to aggregate. The imaging was in three dimensions using an x-ray CT scan at a resolution of 22.2 μm. Once imaged, the concrete particles were made into level set functions by using a watershed segmentation and level set evolution procedure as described by (Vlahinić et al., 2014). Figure 5.2 shows details of the size and shape of the concrete particles. The concrete particles are statistically somewhat irregular with an average sphericity of 0.77. Such sphericity values correspond to fairly oblate particles which is consistent with qualitative observation.

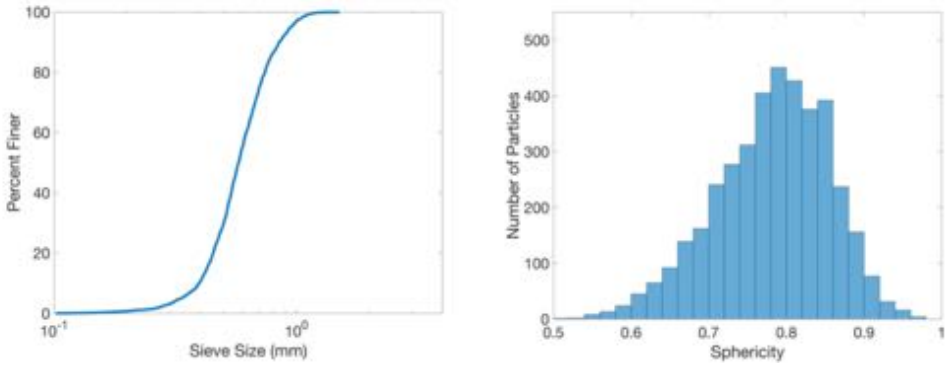

Figure 5.2: Ice simulant particles. (a) Particle size distribution of ice simulant particles. (b) Histogram of particles' sphericity.

This may be of benefit to more heavily sintered specimens where significant shape changes from sintering and the irregular fracture surfaces that arise from loading

would lead to broken ice particles reflecting these kinds of shapes. On the other hand, if the experimental ice specimens start with nearly spherical shapes, then results may be imperfect at early sintering times before significant shape changes from sintering morph particles to a more irregular shape. This concern will likely be alleviated in proposed future work when coupling LS-DEM-BPM to soon to be developed sintering models where the particle shape can be computationally determined by factors such as sinter time and temperature.

5.6 Cone Penetration Testing

In this section, the model is used to predict the mechanics of a cone penetration test and is compared to cone penetration tests conducted on sintered ice samples by (Choukroun et al., 2020) with predictions from the LS-DEM-BPM model. These experiments evaluated the mechanical strength evolution of the plume deposit ice analogs left to sinter at four different temperatures (193 K, 223 K, 233 K, and 243 K) for a period of time up to 14 months.

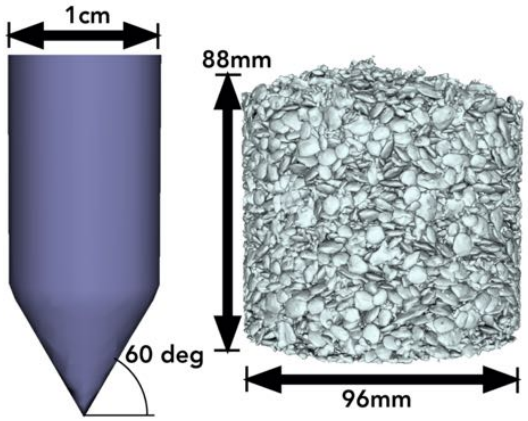

Figure 5.3: Visualization of Numerical Specimen after pluviation and the cone penetrator.

Specimen Preparation

In order to numerically model the cone penetration experiments, first a numerical specimen must be made. The specimen is made with particles larger than in the experiments to allow for reasonable compute times. Particles are pluviated by being dropped into a cylindrical container one layer at a time until the desired height for the specimen is established, a process known as pluviation. Particle volumes are slightly expanded during the pluviation process, then brought back to the intended size for the cone penetration. This is done so that when conducting the cone

penetration experiments, the particles would initiate out of contact which allows space for bonding. A table of the properties and parameters used for the final specimen are shown in Table 5.1. Preliminary cone penetration testing was done to ensure semi-infinite conditions. The specimens porosity is 47% which qualifies as a loose specimen, comparable to the 51(±2)% porosity in the experiments.

To get stiffnesses from the elasticity parameters, we use the suggested conversion shown in (Potyondy et al., 2004). In (Schulson, 1999), the strength is shown to be dependent on both strain rate and temperature where the strength could range from 2-10 MPa at 263 K and increase 25% at 248 K. Since the experiments are conducted at temperatures ranging from 193 K to 243 K, the peak value of 10 MPa is chosen as a standard, though other values are tested in the sensitivity analysis section. The table also reports the level set resolution, surface point density, and cone dimensions. The level set resolution differs from the imaging resolution so that particles have a more manageable size for the cone testing.

The cone itself is made analytically and is represented in the simulation as a level set. Visualizations of both the cone and the pluviated specimen are shown in Figure 5.3. Due to the cone only interacting with the particles as a level set, only the surface points of the particles interact with the cone. This is the same as for the walls which also only interact with particles through the particle's surface points. Walls for this study are given the same mechanical properties as the ice, so the boundaries better represent a semi-infinite condition. In order to speed up the simulations, the cone is initialized with the tip already inserted into the specimen. For this reason, in the results we look to only compare with experiments the region after full cone tip insertion.

Model Results

Results from the model provide insight for both the macroscale and the microscale. On the macroscale, the stress experienced by the cone is evaluated by dividing the total vertical force on the cone by its cross-sectional area. The results for the cone stress versus cone displacement shown in Figure 5.4 show similar trends to the experiment. Three simulation results are shown for various relative neck sizes which is defined as the ratio between the radius of the bond to the radius of the smallest circumscribed sphere of the bonded particle pair. Plots such as these provide insight to the degree of sintering that is likely present in the specimen since more sintering causes larger sinter necks. The stress for the numerical model seems

Property	Value	Units	Source
E	9	GPa	(Schulson, 1999)
G	6.7	GPa	(Schulson, 1999)
μ	0.2	none	(Schulson et al., 2012)
$\bar{\sigma}_c$	10	MPa	(Schulson, 1999)
Level Set Resolution	0.2	mm	
Surface Point Density	6.75	pts/mm^2	
Cylinder Height	88	mm	
Cylinder Radius	48	mm	
Cone Radius	5	mm	
Cone Angle	60	Degrees	
Porosity	47%	none	
Number of Particles	8000	none	

Table 5.1: Properties and dimensions of the particles, specimen, and cone.

to fluctuate more than experiment, which is likely due to the particles being larger than experiment. This is consistent with other studies where larger particles caused results that were less smooth, but each would have a similar average value (Catanoso et al., 2020). The stress rises faster in simulation due to the cone in the numerical model being initialized with the tip inserted.

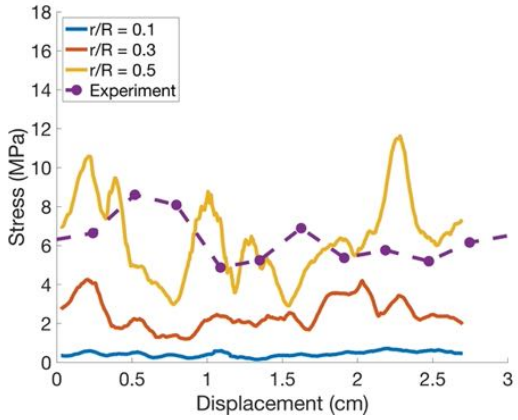

Figure 5.4: Stress versus displacement profile for simulations with three different relative neck sizes with experimental results overlayed. Displacement is zeroed at the depth where the cone tip is fully inserted and the stress on the cone reaches a steady-state. Experimental data is from (Choukroun et al., 2020) for ice allowed to sinter for 13 days at -30 C.

A quantity we will call the cone penetration resistance (CP Resistance) will be defined as the average stress experienced by the cone after the tip is fully inserted. This quantity matches well with experiment when using a relative neck size that is

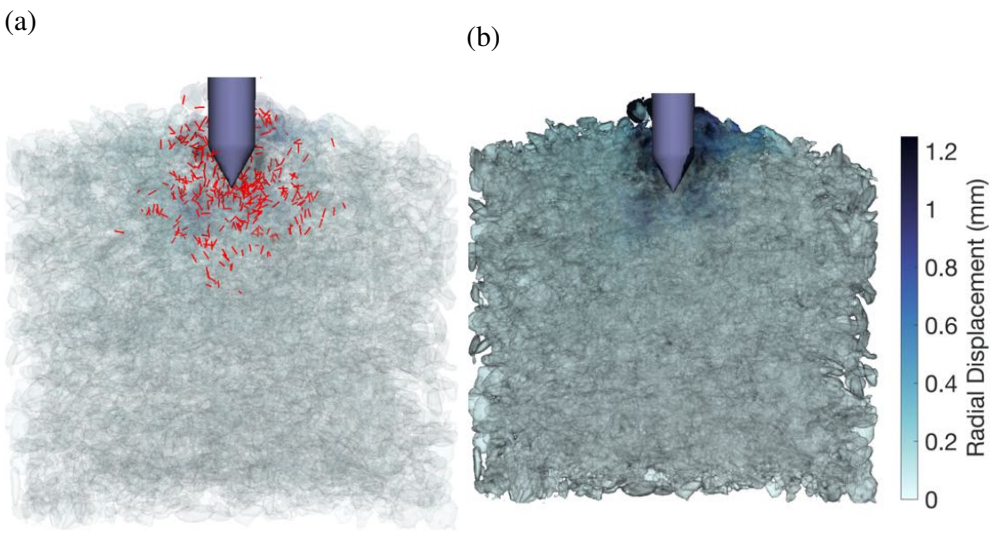

Figure 5.5: Specimen Visualization. (a) Broken bonds are shown in red and are concentrated in the local area around the cone. (b) Particles displacing radially away from the cone.

indicative of the sinter phase the ice particles are in. The calibration for relative neck size is shown in Section 4.4.

For a look at the microscale, Figure 5.5 shows visualizations of the specimen during penetration with individual broken bonds (a) and particle displacements shown (b). It can be seen that both bonds and particle displacement are confined to the local area around the cone, confirming that the specimen is effectively semi-infinite. We can understand the region of visible displacement as the region where particles are fully broken, since particles that still have even a single bond to the greater structure are still inhibited from motion. Since the area where broken bonds are seen is nearly the same as the displacement area, it suggests that most particles that experience breakage completely break free of all other particles. Quantitatively this confirmed that around 80% of particles that experience breakage have all their bonds broken. Whether or not this is a feature of the model or of the cone penetration experiment is unclear, however we can surmise that this is due to the fact that any particle in the path of the cone must completely break to be able to move and allow the cone to pass. Particles that experience only partial breakage from the sinter network must be in the vicinity but not in the direct path of the cone which must be composed of a much smaller set of particles from the ones in the cone path. Also, the irregular particle shapes increase the interlocking between particles and therefore deviatoric stress in a local region. These facts would be true for both experiment and model.

This phenomenon is well known and could encourage more complete breakage in a local area (Kawamoto et al., 2018b).

Sensitivity Analysis

To better understand the model limitations, we investigated the local sensitivity of the CP Resistance to four parameters: penetration rate, bond stiffness, critical strength, and relative neck size. In each case, we varied the value of one parameter and quantified the change in the resulting CP Resistance value. A sensitivity measure denoted S is defined as the absolute value of the percent change in CP Resistance over the percent change in the tested quantity. Figure 5.6 shows that penetration rate and bond stiffness have little effect on the result. For bond stiffness, this is not surprising since it has been shown before that macroscopic response to the stiffness parameter in LS-DEM is fairly insensitive (Kawamoto et al., 2016) and would be expected to be even less sensitive in an application with an unconfined boundary. The fact that the cone penetration rate has little effect on CP Resistance shows that inertial effects are not significantly affecting the bonding mechanics. This can be seen as a verification that the damping strategy for the model is effective since the penetration rate is quite fast for the purpose of computational efficiency at a velocity of 0.5 m/s. On the other hand, both the bond critical strength and the relative neck size affect the CP Resistance significantly. This is expected since it is natural that stronger non-porous ice and thicker, heavier sintering leads to stronger porous ice.

Connection to Sintering Models

In LS-DEM-BPM, the radius of the sintered neck is the mechanical representation of the degree of sintering that has taken place. In reality, there are additional changes in the structure and geometry of sintering ice particles that will affect their bulk mechanical strength, and therefore the relative neck size we use in the model must account for their contribution as well. For this reason, it is of great importance to understand how the strength changes due to relative neck size in the model and how that correlates to the strength changes in porous ice experiments. Key controlling variables of the sintering process in experiment are temperature and sinter time. (Molaro et al., 2019) model the geometric changes of spherical ice particles during the sintering process as a function of temperature and sinter time. They break down the sintering process into three distinct stages, the first of which is dominated by neck growth. Their model quantifies the change in neck size with temperature and particle size during stage 1, though it does not fully describe how the ice evolves

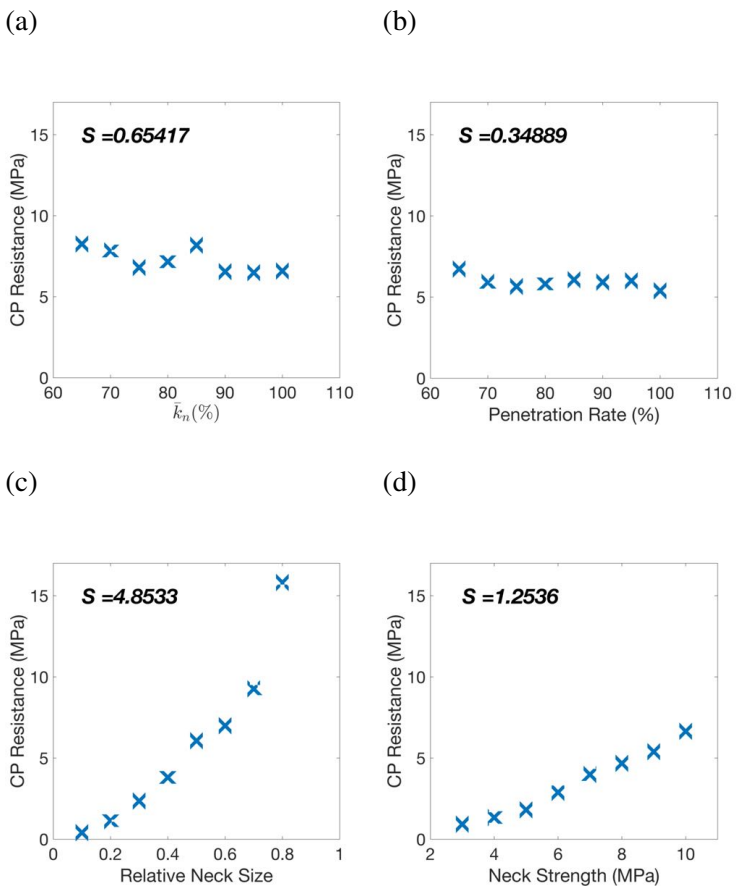

Figure 5.6: CP Resistance versus (a) bond stiffness, (b) penetration rate, (c) relative neck size, and (d) critical strength. The sensitivity is quantified as the percent change in CP Resistance divided by the percent change in the tested quantity and shown in each plot.

during stages 2 and 3 when the microstructure becomes morphologically complex due to particle growth, development of agglomerate particles, and other effects. As a result, they can only quantify the effects of sintering during part of the duration of the experiments of (Choukroun et al., 2020), which followed the ice into stage 2. However, using their predicted neck growth times with our LS-DEM-BPM model can still provide important insight into stage 1 sintering. We can use the relationship between neck growth, temperature, and time in the Molaro et al. model to determine what neck radius we use in this model when given these environmental parameters within stage 1.

Figure 5.7a shows the experimental results for CP Resistance versus sinter time and temperature (Choukroun et al., 2020), the longest of which was carried out for nearly 400 days. According to (Molaro et al., 2019), stage 1 for ice under the

same conditions finishes as quickly as within the first day, highlighting the need for further development of the sintering model to quantify changes in the ice during later stages of sintering. When using their predicted neck size at the end of stage 1, the strength simulated by the LS-DEM-BPM is consistent with the CP Resistance values coinciding with the y-axis intercept of the best fit lines in Figure 5.7a. That is, per the CP Resistance profiles from Choukroun et al., the strength of the ice samples at time zero has a non-zero value which corresponds to the simulated strength of the ice at the end of stage 1. This supports the prediction by Molaro et al. that rapid modification occurs over short timescales in stage 1, resulting in the early rise in ice strength as seen in the experiments. This shows a remarkable consistency between the experiments and the two models and suggests that the linear profiles measured by Choukroun et al. characterize the behavior of the ice following the completion of stage 1.

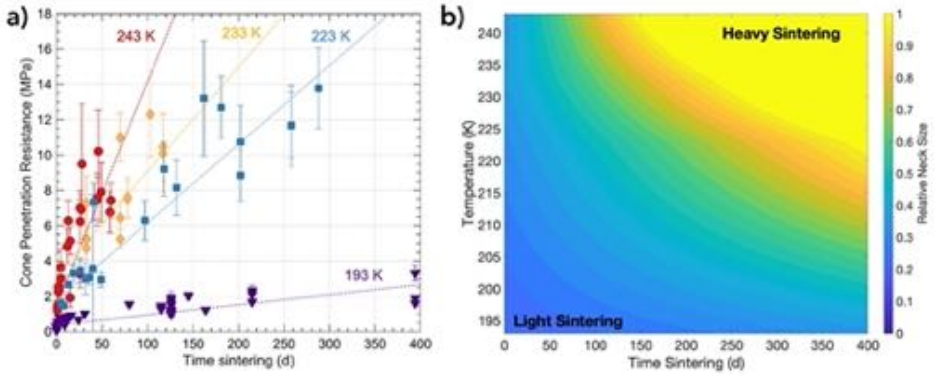

Figure 5.7: Relative neck size calibration. (a) Cone penetration strength results, figure from (Choukroun et al., 2020). (b) Calibrated relative neck size in the LS-DEM-BPM model to sinter time and temperature by matching CP Resistance.

Since the model of Molaro et al. cannot be used to provide a neck size for the LS-DEM-BPM model over the entire experiment duration, we must calibrate the simulation results using the experiments for the time beyond stage 1. To do this, we determine an effective relative neck size parameter by looking at what relative neck size will produce the same CP Resistance in the simulation as in the experiment for a given temperature and sinter time. Figure 5.7b shows this calibration, where the x and y axes are sinter time and temperature, respectively, during the experiment that produced the same CP Resistance value as the simulation with the corresponding relative neck size shown in the colorbar. This effective relative neck size can be thought of as a proxy for the total amount of modification that has occurred from the combined neck growth and additional effects that occur during stage 2 of the

sintering process. Since both stages 1 and 2 are controlled by the same primary diffusion mechanisms (Choukroun et al., 2020), relative neck size also provides an estimate of the total amount of diffusion that has occurred. Future studies aimed at further developing the model of Molaro et al. (2019) can leverage predictions of strength from relative neck size to link to the experiments. Future work on this model will include comparisons to different types of experiments to show that this calibration honors the physics and not just one type of specimen loading. For now, however, this graph should be used as reference for future use of LS-DEM-BPM for cone penetration in sintered ice.

5.7 Conclusions

LS-DEM-BPM is an effective method for modeling the mechanics of sintered ice by directly modeling the sintering mechanics through the bonded particle method. The outcome for this model provides understanding of not only the macroscale phenomena of cone penetration resistance, but also the microscale details of the kinematics and kinetics of each ice particle and sintered bond respectively. The addition of shape to the particles allows higher fidelity, an understanding of the role particle shape plays in ice mechanics, and a window for future work to enable particle shape deformation using sintering models. Both the mechanics of the model and an example of determining particle shape from CT scans were shown. The cone penetration testing showed that the model predicts reasonable strength displacement profiles and with a calibrated relative neck size can correctly predict the CP Resistance.

Chapter 6

PREDICTING THE LANDER SURFACE INTERACTION WHEN LANDING ON ENCELADUS

Harmon, J.M. et al. (n.d.). "Predicting the lander-surface interaction when landing on Enceladus". In: *(in preparation)*.

6.1 Introduction

This chapter will show results from modeling a landing on the Enceladus surface. Enceladus presents unique problems to landing due the confluence of microgravity, extreme cold, and a constant resurfacing from the tiger stripe plumes. The plume deposition has been modeled and it shows that the amount of resurfacing can be very significant, with some deposition maps predicting as much as 0.1 mm/yr in certain areas (Southworth et al., 2019). This is good news for scientific return since the material depositing from the plume is the most interesting. However, for landing it can produce problems because at 80K, the surface temperature of Enceladus, it would take longer than the age of the solar system for this ice to reach even moderate amounts of sintering according to current models (Molaro et al., 2019). As seen in Chapter 5, sintering will greatly increase the strength of ice, so without it there is worry that the surface is not strong enough to support a lander. Regions near the tiger stripes feature hot spots, which opens up the possibility of significant sintering to occur (Spitale et al., 2007). The full range of sintering level will be tested here in order to more completely understand the necessity of sintering for a successful landing.

The modeling technique used here will be the same as in Chapter 5 with the same parameters for the ice, unless otherwise stated. There is one aspect of the modeling method that is critical to understand for this chapter, and should be reintroduced and that is relative neck size, r_{rel}. Relative neck size is the model parameter describing the amount of sintering that has occurred and manifests itself as the ratio between the radius of the bond that represents the sinter to the radius of the smallest circumscribed sphere between the two bonded particles. In Chapter 5, experiment and sinter growth models were used to approximate what relative neck sizes coincide with the three sintering stages mechanically. The first stage, where sinter necks become visible and individual particles are clearly distinct, the relative

neck size ranges from 0 to about 0.4. The second stage is where the sintering begins to cause significant morphological change in the particles; in this stage, neck sizes range from about 0.4 to 0.8-0.9. In the final stage, individual ice particles are difficult to distinguish, and it is often easier to describe the microstructure by the voids rather than particles. Here the relative neck size ranges from 0.8-0.9 to 1, where at $r_{rel} = 1$, we consider the ice to be fully solid. Outside of this important note on relative neck size, this chapter will skip the modeling method section and instead start with model setup. The model setup will describe both the lander and surface specimen setup. Then the results will be shown over two sections, one for landing on a flat surface and another for sloped surfaces. The flat surface subsection will be focusing mostly on surface properties such as ice sintering and particle size distribution (PSD). The sloped surface subsection will mostly be focused on what can be done to minimize the downslope sliding displacement. Finally, a conclusion will summarize the results and give some suggestions for future work.

6.2 Modeling Setup

Lander

The lander was modeled as a single rigid footpad with a simple shape. It was assumed that the lander would have four footpads and that the weight would be distributed evenly across each footpad such that the single footpad modeled would weigh one fourth the weight of the entire lander. The mass of the lander was set to 1000 kg. Three simple shaped footpad geometries were chosen and will be referred to as the cone, disk, and hemisphere, as shown in Figure 6.1. All three geometries have a 13 cm radius at the base making the ultimate impact surface area the same. In all simulations, we are assuming that the other footpads of the lander will provide the necessary stability, so the simulated footpad's rotation is negligible. In implementation, this assumption is manifested by the rotation of the footpads being disabled. The mechanical properties of the footpad were kept the same as the cone in Chapter 5, including the friction coefficient which is $\mu = 0.2$. The footpads will start each simulation with an initial downward velocity of 1 m/s and placed immediately above the surface.

Surface

The surface was modeled as a cylindrical granular specimen of 20000 particles. The cylinder was made much wider than tall, so the footpads had room to slide significantly when modeling landing on a sloped surface. Specimen preparation was

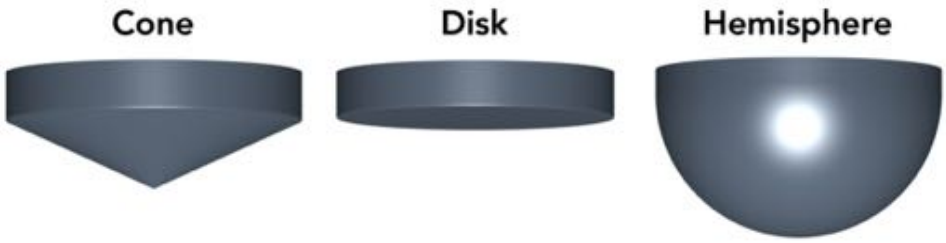

Figure 6.1: Three footpad geometries were chosen, each with a base radius of 13cm.

conducted by dropping particles into the specimen with gravity until equilibrium, a process known as pluviation. Because the gravity of Enceladus is so low, attempts at pluviating the particles at Enceladus gravity were unsuccessful, so instead the specimen was pluviated at Earth gravity. After equilibrium was reached at Earth gravity, the particles were slightly shrunk to remove contact, then bonded together at a prescribed sintering level. Once sintered, time was given for the sample to re-establish equilibrium at Enceladus gravity. Properties for the ice were kept the same as in Chapter 5.

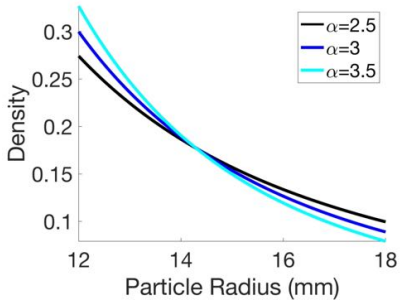

Figure 6.2: The three PSDs for the surface specimens have power law slopes that span the range of power law slopes seen in the particles captured by Cassini. The size range was not changed between specimens and span significantly larger particles than predicted on Enceladus to produce feasible computation times.

To have reasonable compute times, the particles had to be much larger than what is actually expected on the surface. Particle sizes in all the specimens ranged in size from 12mm to 18mm. The distribution of sizes were defined using a power law with slope α,

$$p(r) \sim r^{-\alpha} \tag{6.1}$$

In Southworth et al. (2019), the PSD slope, α, seen from particles ejecting from the plumes is reported to be between $[2.5, 3.5]$ so three surface specimens were made with α values at 2.5, 3, and 3.5 as shown in Figure 6.2. Low values of α correspond

to a more uniform distribution of sizes, while higher values correspond to more graded samples.

6.3 Results

Penetration Depth

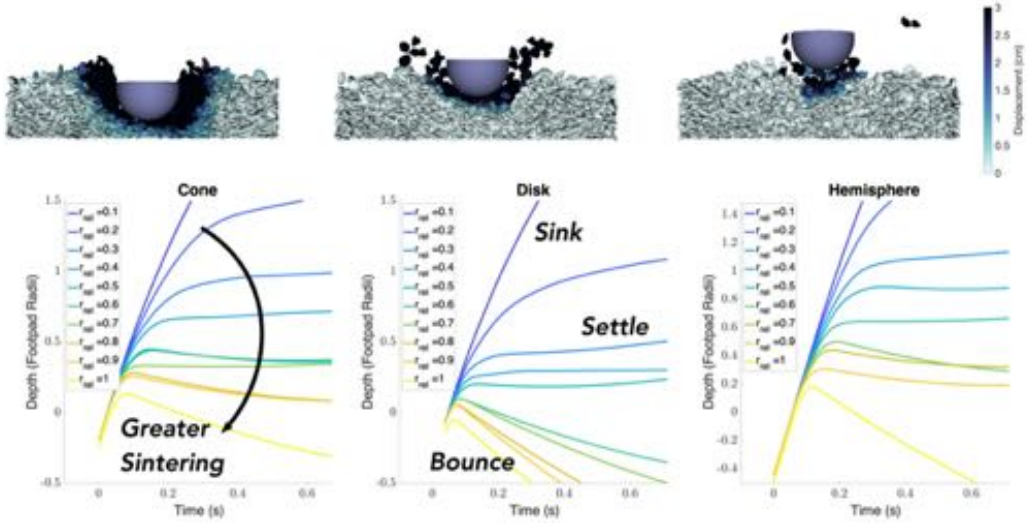

Figure 6.3: The visualizations on top from left to right have relative neck sizes of 0.1, 0.5, and 1.0, respectively, and are good examples of a footpad uncontrollably sinking, settling or bouncing. The plots show the depth of the tip of the footpad over time for the three footpad geometries. Each geometry performs similarly, however the disk is noticeably less likely to sink and more likely to bounce.

First, we will look at the results when the footpads land on a flat surface at various levels of ice sintering. In Figure 6.3, we can see from the visualizations that the outcome can be broadly categorized in three ways: large amount of sinking, a reasonable settle, or a bounce. All three footpad geometries experience each of these at different stages of sintering, however the transition between these categories is at different sintering levels for each one. For the disk, a little less sintering is required compared to the other footpads for the lander not to sink, however, the disk will bounce at much earlier sintering levels as well. For both the hemisphere and the cone, any relative neck size between $r_{rel} = [0.3, 0.9]$ produces a landing that neither sinks nor shows significant bouncing. From the analysis in Chapter 5, these relative neck sizes reflect late stage 1 to late stage 2 sintering, which, from a lander stabilization point of view, are the most successful from model predictions.

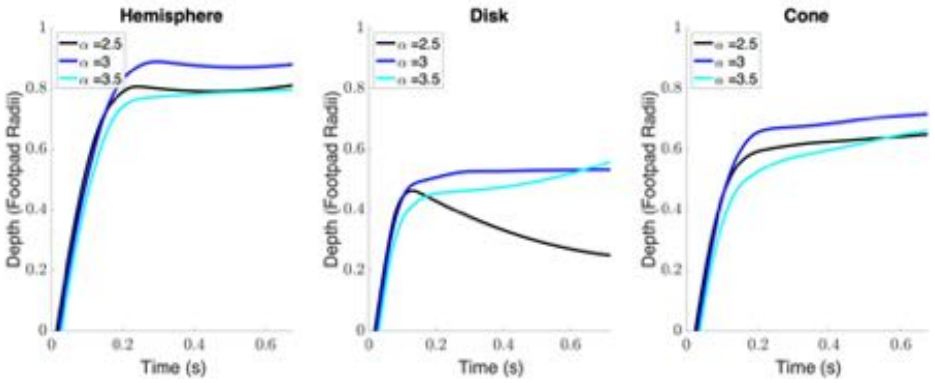

Figure 6.4: Each footpad geometry was tested on specimens with three different PSDs. The PSDs only differ in power law slope, not in size range. Depth is relatively similar across all PSDs for each footpad. Some bounce occured for the disk at $\alpha = 2.5$, but the maximum depth still matches the others.

Samples with each of the PSD candidates produced relatively the same amount of sinking for a given footpad geometry and ice sintering. Figure 6.4 shows the depth of footpad penetration for all three footpads at all three PSDs at an ice sintering level of $r_{rel} = 0.4$. This sintering level was chosen because the lander for each footpad geometry settles at a significant depth, so the effect of differing PSDs should be maximized. Depth of penetration for each of the PSD specimens are relatively equal for each footpad with only minor changes that could be explained by local porosity variations that are generated naturally during pluvation. Because it is well known that the PSD does affect the bearing capacity of a surface (Das, 2010), we can conclude that, in this case, it is the range of particle sizes that make the difference and not the slope of the PSD power law.

Sloped Surfaces

The surface of Enceladus is known to not be flat (Schenk et al., 2009), therefore any lander will likely be landing on a sloped surface. To model this, the specimen and footpad are kept the same and the gravity and initial footpad velocity are rotated to a prescribed slope angle. In this way, the x, y, and z directions are now transformed into the surface normal, downhill, and transverse directions. Because of the lack of difference in penetration depth from each PSD sample, the one with $\alpha = 3.0$ was the only one used for this section and was chosen because it is in the middle of the tested range.

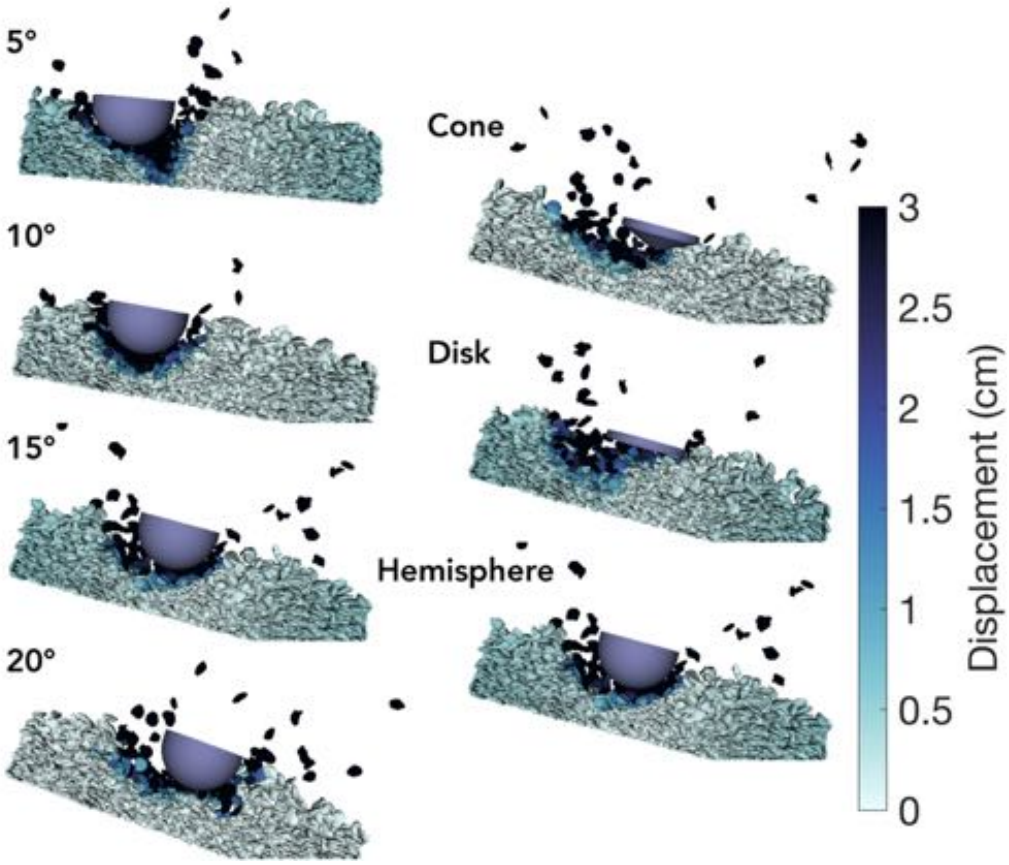

Figure 6.5: Visualizations on the left show the hemisphere footpad landing on increasingly sloped surfaces resulting in increasing lateral displacement. On the right, the visualizations are all at 15^o and demonstrate the extent to which footpad geometry plays a role. All visualizations are at $t = 2$ seconds after impact.

Figure 6.5 shows visualizations for many landings on various slopes and footpad geometries at a sintering level of $r_{rel} = 0.4$. On the left, the hemisphere lands on slope angles ranging from 5^o to 20^o successfully with only slightly larger downslope displacement at higher angles. Figure 6.6 quantitatively shows that the hemisphere landing on a surface with a 20^o slope and $r_{rel} = 0.4$ displaces downhill less than 2 footpad radii. Among all the simulations, this was the best case scenario for a 20^o slope angle.

On the right of Figure 6.5, each lander footpad lands on a slope of 15^o, showing the differences in footpad geometry qualitatively, and the quantitative data on downhill displacement is shown in 6.6. What is immediately noticable is that changing the footpad geometry does not change the results as much as a change of 5^o of slope angle does. However, it is still noticeable in the visualizations and plots that the

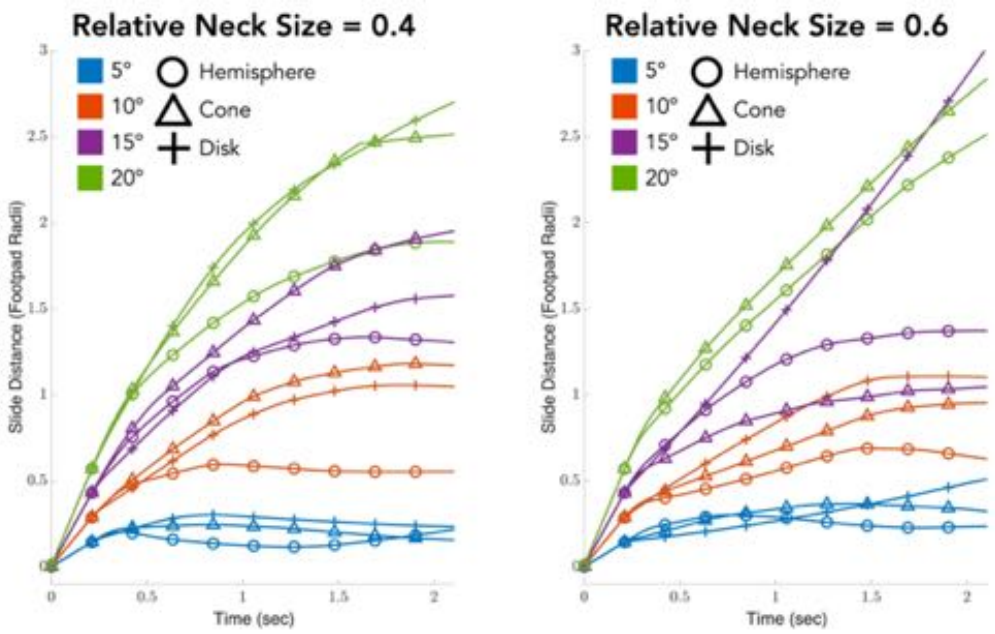

Figure 6.6: Downhill slide displacement versus time plots for relative neck sizes of 0.4 and 0.6 for all slopes and geometries tested. The disk was not tested at 20^o and $r_{rel} = 0.6$ because it slid critically far at 15^o.

hemisphere does minimize the sliding downhill compared to the cone and disk. This is expected for the disk geometry because its blunt face produces less penetration and, therefore, inhibits its ability to "lock in" to the ground. For the cone, however, it was thought that it might perform well on slopes due to its pointed tip, but it is possible that this cone's height to radius ratio is too small to grip enough to slide less than the hemisphere. In fact, there is only one scenario where the hemisphere does not outperform the cone which is at a slope of 15^o and $r_{rel} = 0.6$.

To get a better understanding for this one instance where the cone performed better than the hemisphere, we will look closely at how the cone performs with various relative neck sizes. In Figure 6.7, both visualizations and plots are shown for the landing of the cone geometry at three relative neck sizes. At $r_{rel} = 0.6$, the cone lands with almost twice as little sliding as $r_{rel} = 0.4$ and $r_{rel} = 0.8$, both of which slide about the same. The visualizations illuminate that at lower sintering, the cone is blunt enough and the ice is weak enough to produce large amounts of breakage surrounding the landing spot. The extra breakage removes and/or weakens the surrounding area which leaves space for the cone to slide despite a larger penetration depth. At higher sintering, the opposite occurs, the breakage is relatively minimal

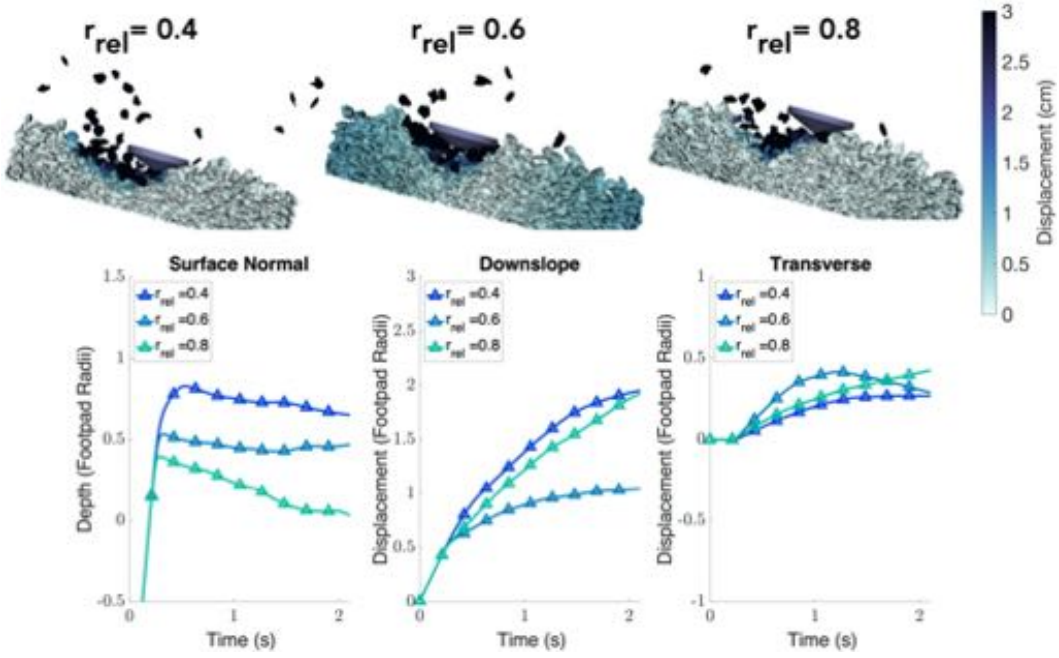

Figure 6.7: Visualizations and plots show the movement of the cone footpad for three relative neck sizes. For both visualizations and plots, the surface slope is 15^o.

and not enough for the cone tip to properly grip the surface. Therefore, there exists a "Goldilocks" zone for optimum sintering level for minimizing downslope displacement where the surface is weak enough to allow significant penetration, but strong enough to not break further. This zone also exists for the hemisphere, but is not as pronounced as with the cone.

6.4 Conclusion

The landing on the surface of Enceladus was modeled for many footpad geometries, ice sintering levels, PSDs, and surface slope angles. Through this study, we found that while the footpad geometries do make a difference, factors such as sintering level and slope angle affect the success of landing much more significantly. Based on this model, when choosing a landing location, it is safest to land in areas at stage 2 sintering, where slope angles of 15^o can be comfortably landed on. Areas in late stage 2 and early stage 3 can be landed on, but some bouncing may occur and it would be recommended to land on a shallower angle to avoid too much sliding.

While not every landing that was simulated would be considered successful, the model did show that landing is very plausible for many of the tested conditions. Some further study could improve the success rate by testing more realistic footpad

geometries that have better grip than the simple shapes tested here. Moreover, in the entire study, only one friction coefficient was tested for both ice-ice and footpad-ice sliding, and a simple Coulomb model was used. Ice has been shown to have a range of friction coefficients that are significantly dependent on temperature and velocity. Further study into friction with this model would better predict what is possible.

Chapter 7

CONCLUSION AND FUTURE OUTLOOK

There are many unknowns when interacting with an extraterrestrial body's surface, however the risk can be dramatically reduced with reliable predictive models. This thesis extended the state of the art such that modeling can now capture key features at the microscale of granular materials at destinations of interest.

In Chapters2 and 3, a novel method for modeling crushable granular materials was validated for predicting both the mechanics and particle shape evolution. Importantly, the model made impressive predictions for three separate shape descriptors: sphericity, elongation and flatness. Further, correlations were found between volume and contact force showing that larger particles provide much of the resistance to deformation in the vertical direction. This is counter-intuitive because large particles are generally weaker, but two explanations were found in the data. First was a survival of the fittest effect where the large particles on the weak side of the strength distribution were the ones that broke, raising the average strength of the larger particles. The second was a cushioning effect whose evidence came from the combined correlation of volume and coordination number, volume and isotropic stress, and volume and deviatoric stress. Because the volume correlation with coordination number is significant, along with the volume correlation with isotropic stress being higher than the correlation with deviatoric stress, the data shows a direct indication of the cushioning effect occurring. Due to the abundance of brittle, irregularly shaped particles composing regolith, this work will enable the proper modeling of those surfaces.

Chapters 4 and 5 developed and demonstrated a bonding technique that can be used to model sintered ice, among other adhesive mechanisms. Using this to model a cone penetration test in ice enables an intimate look into the effect of sintering on the strength of the ice. Important connections were made between the science of sinter growth and model parameters that illuminated some understanding for how to further use the method for space applications. In Chapter 6, the model was then indeed used directly for the space application of landing on the surface of Enceladus. The model predicted that some sintering must be present for the lander to not sink too deep, however complete sintering would cause the lander to bounce.

When landing on an inclined surface, the model predicted that successful landing is possible at angles of 20 degrees. Between the three footpad geometries tested, the disk slid significantly more for all cases, but no footpad geometry made as big of a difference in downslope displacement as a 5 degree change in inclination.

7.1 Future Outlook

There is a significant amount of future work to be done with both modeling methods. With the splitting method developed and validated, it can now be used for the modeling of engineering implements for mission design considerations. It would be particularly useful for the design of base-type structures on bodies like the Moon or Mars. These heavy structures will greatly benefit from the increased predictability in regards to particle shape, because they will more severely test the limits of the surface strength. This method could also be used to study the effects of impacts on these surfaces. Impacts produce heavy amounts of breakage and particle morphology change that result in large changes in the surface properties, all of which could be captured by the level set splitting method.

Further work in porous ice could include repeating the work done on the Enceladus landing for other bodies with different properties. Also, level sets have the ability to efficiently morphologically change. Level sets could be used with sinter growth models to make microscale geometry predictions. If the sinter growth could be captured by the level sets, then those level sets could be used for the mechanics modeling, which would be made significantly more accurate by an improved initial condition.

Some bodies in the solar system have surfaces that are a mix of rock and ice, such as comets, or dwarf planets, such as Ceres (McCord et al., 2019). For these bodies a combination of the methods would be ideal. Combining these methods could be done in two ways. The first would be to enable splitting only when a particle has broken all of its bonds with other particles. This method is quite simple and very little modification of algorithms would be required. However, it caries an assumption that the ice is so much weaker than the rock that the icy sinters will always break before the rock does. This assumption breaks down if there exist ice connections that are not stressed due to the loading direction and if the rock is on the much weaker side of the strength distribution. Therefore the first method is not the most complete way to marry the splitting and bonding model. The second would be to enable splitting on particles that are still bonded. Here, the bonds must be communicated to the new

particles when splitting occurs, which would require special care for large specimens in which distributed memory parallelization is required. Moreover, because in the current splitting method fracture surfaces connect the highest forces, this may occur at locations where bonds are present, making it unclear which child particle should inherit the bond. Likely the best answer will be to alter the method for determining the fracture shape so that this issue is rare.

With the splitting and bonding methods, the door is open for the study of the surface strength on planetary bodies throughout the solar system. This thesis has outlined the ways in which these models are prepared to inform such work.

BIBLIOGRAPHY

Afshar, Tabassom et al. (2017). "Changes to Grain Properties due to Breakage in a Sand Assembly using Synchrotron Tomography". In: *EPJ Web of Conferences* 140, p. 07004. DOI: 10.1051/epjconf/201714007004.

Aldrin, B. and W. Warga (1973). *Return to Earth*. Random House. ISBN: 0394488326.

Altuhafi, F.N. and M.R. Coop (2011). "Changes to particle characteristics associated with the compression of sands". In: *Géotechnique* 61.6, pp. 459–471. DOI: 10.1680/geot.9.P.114. eprint: https://doi.org/10.1680/geot.9.P.114. URL: https://doi.org/10.1680/geot.9.P.114.

Andò, Edward et al. (2012). "Grain-scale experimental investigation of localised deformation in sand: a discrete particle tracking approach". In: *Acta Geotechnica* 7.1, pp. 1–13. ISSN: 1861-1133. DOI: 10.1007/s11440-011-0151-6.

Armstrong, N. (1969). *Moon Landing Broadcast*.

Atkinson, J. (2007). *The Mechanics of Soils and Foundations, Second Edition*. Spon text. Taylor & Francis. ISBN: 9780203012888. URL: https://books.google.com/books?id=KRR34SOOUNAC.

Badescu, Mircea et al. (2019). "Sampling Tool Concepts for Enceladus Lander In-Situ Analysis". In: *2019 IEEE Aerospace Conference*. DOI: 10.1109/aero.2019.8741568. URL: http://dx.doi.org/10.1109/aero.2019.8741568.

Beeler, N. M. et al. (1996). "Frictional behavior of large displacement experimental faults". In: *Journal of Geophysical Research: Solid Earth* 101.B4, pp. 8697–8715. DOI: 10.1029/96jb00411. eprint: https://agupubs.onlinelibrary.wiley.com/doi/pdf/10.1029/96JB00411. URL: https://agupubs.onlinelibrary.wiley.com/doi/abs/10.1029/96JB00411.

Ben-Nun, Oded and Itai Einav (2010). "The role of self-organization during confined comminution of granular materials". In: *Philosophical Transactions of the Royal Society of London A: Mathematical, Physical and Engineering Sciences* 368.1910, pp. 231–247. ISSN: 1364-503x. DOI: 10.1098/rsta.2009.0205.

Bierhaus, E. B. et al. (2021). "Bennu regolith mobilized by TAGSAM: Expectations for the OSIRIS-REx sample collection event and application to understanding naturally ejected particles". In: *Icarus* 355, p. 114142. ISSN: 0019-1035. DOI: https://doi.org/10.1016/j.icarus.2020.114142.

Billi, Andrea (2005). "Grain size distribution and thickness of breccia and gouge zones from thin ($<$1m) strike-slip fault cores in limestone". In: *Journal of Structural Geology* 27.10, pp. 1823–1837. ISSN: 0191-8141. DOI: https://doi.org/10.1016/j.jsg.2005.05.013. URL: http://www.sciencedirect.com/science/article/pii/S0191814105001045.

Blott, Simon J. and Kenneth Pye (2008). "Particle shape: a review and new methods of characterization and classification". In: *Sedimentology* 55.1, pp. 31–63. DOI: https://doi.org/10.1111/j.1365-3091.2007.00892.x.

Campins, Humberto et al. (2010). "Water ice and organics on the surface of the asteroid 24 Themis". In: *Nature* 464, pp. 1320–1. DOI: 10.1038/nature09029.

Carlson, R W et al. (2009). "Europa's Surface Composition". In: *Europa*, pp. 283–328. DOI: 10.2307/j.ctt1xp3wdw.18.

Catanoso, Damiana et al. (2020). "Analysis of Sample Acquisition Dynamics Using Discrete Element Method". In:

Celigueta, Miguel et al. (2017). "Accurate modelling of the elastic behavior of a continuum with the Discrete Element Method". In: *Computational Mechanics*. DOI: 10.1007/s00466-017-1453-9.

Cheng, Y. P., Y. Nakata, and M. D. Bolton (2003). "Discrete element simulation of crushable soil". In: *Géotechnique* 53.7, pp. 633–641. DOI: 10.1680/geot.2003.53.7.633. eprint: https://doi.org/10.1680/geot.2003.53.7.633. URL: https://doi.org/10.1680/geot.2003.53.7.633.

Choukroun, Mathieu et al. (2020). "Strength evolution of ice plume deposit analogs of Enceladus and Europa". In: *Geophysical Research Letters* 47.15. DOI: 10.1002/essoar.10503169.1. URL: http://dx.doi.org/10.1002/essoar.10503169.1.

Christmann, J. et al. (2015). "Measurement of the fracture toughness of polycrystalline bubbly ice from an Antarctic ice core". In: *Earth System Science Data* 7.1, pp. 87–92. DOI: 10.5194/essd-7-87-2015. URL: https://www.earth-syst-sci-data.net/7/87/2015/.

Chyba, C F (2000). "Energy for microbial life on Europa". In: *Nature* 403.6768, pp. 381–382. ISSN: 0028-0836. DOI: 10.1038/35000281.

Cil, M. B. and K. A. Alshibli (2012). "3D assessment of fracture of sand particles using discrete element method". In: *Géotechnique Letters* 2.3, pp. 161–166. DOI: 10.1680/geolett.12.00024.

Cil, M.B. and K.A. Alshibli (2014). "3D evolution of sand fracture under 1D compression". In: *Géotechnique* 64.5, pp. 351–364. DOI: 10.1680/geot.13.P.119.

Cil, Mehmet B, Changbum Sohn, and Giuseppe Buscarnera (2020). "DEM modeling of grain size effect in brittle granular soils". In: *Journal of Engineering Mechanics* 146.3.

Coco, Armando and Giovanni Russo (2013). "Finite-difference ghost-point multigrid methods on Cartesian grids for elliptic problems in arbitrary domains". In: *Journal of Computational Physics* 241, pp. 464–501. ISSN: 0021-9991. DOI: https://doi.org/10.1016/j.jcp.2012.11.047. URL: http://www.sciencedirect.com/science/article/pii/S0021999112007292.

Cundall, P. A. and O. D. L. Strack (1979). "A discrete numerical model for granular assemblies". In: *Géotechnique* 29.1, pp. 47–65. DOI: 10.1680/geot.1979.29.1.47.

Daniels, Karen E., Jonathan E. Kollmer, and James G. Puckett (2017). "Photoelastic force measurements in granular materials." In: *Review of Scientific Instruments* 88.5.

Das, Braja M. (2010). *Principles of Foundation Engineering*. 7th. CL-Engineering. ISBN: 0495668109.

DeGiuli, E. and M. Wyart (2017). "Friction law and hysteresis in granular materials". In: *Proceedings of the National Academy of Sciences*. ISSN: 0027-8424. DOI: 10.1073/pnas.1706105114. eprint: https://www.pnas.org/content/early/2017/08/14/1706105114.full.pdf. URL: https://www.pnas.org/content/early/2017/08/14/1706105114.

Dieterich, James H. (1979). "Modeling of rock friction: 1. Experimental results and constitutive equations". In: *Journal of Geophysical Research: Solid Earth* 84.B5, pp. 2161–2168. DOI: 10.1029/JB084iB05p02161. eprint: https://agupubs.onlinelibrary.wiley.com/doi/pdf/10.1029/JB084iB05p02161. URL: https://agupubs.onlinelibrary.wiley.com/doi/abs/10.1029/JB084iB05p02161.

Duriez, J. and C. Galusinsky (2020). "Level Set Representation on Octree for Granular Material with Arbitrary Grain Shape". In: pp. 64–71. DOI: 10.14311/tpfm.2020.009.

Eberhardt, Erik, B. Stimpson, and Doug Stead (1999). "Effects of Grain Size on the Initiation and Propagation Thresholds of Stress-Induced Brittle Fracture". In: *Rock Mechanics and Rock Engineering* 32, pp. 81–99. DOI: 10.1007/s006030050026.

Einav, Itai (2007). "Breakage mechanics - Part 1: Theory". In: *Journal of the Mechanics and Physics of Solids* 55.6, pp. 1274–1297. ISSN: 0022-5096. DOI: https://doi.org/10.1016/j.jmps.2006.11.003. URL: http://www.sciencedirect.com/science/article/pii/S0022509606001827.

El Ghoraiby, Mohamed, Hanna Park, and Majid T. Manzari (2020). "Physical and Mechanical Properties of Ottawa F65 Sand". In: ed. by Bruce L. Kutter, Majid T. Manzari, and Mourad Zeghal. Cham: Springer International Publishing, pp. 45–67. ISBN: 978-3-030-22818-7.

Eluszkiewicz, Janusz (1991). "On the microphysical state of the surface of Triton". In: *Journal of Geophysical Research: Space Physics* 96.S01. publisher: John Wiley & Sons, Ltd, pp. 19217–19229. ISSN: 0148-0227. DOI: 10.1029/91ja01858.

Evans, A.M. (1993). *Ore Geology and Industrial Minerals: An Introduction*. Geoscience Texts. Wiley. ISBN: 9780632029532. URL: https://books.google.com/books?id=VbTyfOjMpRgC.

F. L. Nakata, A et al. (1999). "A probabilistic approach to sand particle crushing in the triaxial test". In: *Geotechnique* 49, pp. 567–583. DOI: 10.1680/geot.1999.49.5.567.

Fournier, Thomas and Julia Morgan (2012). "Insights to slip behavior on rough faults using discrete element modeling". In: *Geophysical Research Letters* 39.12. DOI: 10.1029/2012gl051899. eprint: https://agupubs.onlinelibrary.wiley.com/doi/pdf/10.1029/2012GL051899. URL: https://agupubs.onlinelibrary.wiley.com/doi/abs/10.1029/2012GL051899.

Froiio, F. and J.-N. Roux (2010). "Incremental response of a model granular material by stress probing with DEM simulations". In: *AIP Conference Proceedings* 1227.1, pp. 183–197. DOI: 10.1063/1.3435388. eprint: https://aip.scitation.org/doi/pdf/10.1063/1.3435388. URL: https://aip.scitation.org/doi/abs/10.1063/1.3435388.

Galindo-Torres, S.A. et al. (2012). "Breaking processes in three-dimensional bonded granular materials with general shapes". In: *Computer Physics Communications* 183.2, pp. 266–277. ISSN: 0010-4655. DOI: https://doi.org/10.1016/j.cpc.2011.10.001. URL: http://www.sciencedirect.com/science/article/pii/S0010465511003298.

Garcia, D., C.L. Lin, and J.D. Miller (2009). "Quantitative analysis of grain boundary fracture in the breakage of single multiphase particles using X-ray microtomography procedures". In: *Minerals Engineering* 22.3, pp. 236–243. ISSN: 0892-6875. DOI: 10.1016/j.mineng.2008.07.005.

Gelino, Nathan J. et al. (n.d.). "Off Earth Landing and Launch Pad Construction—A Critical Technology for Establishing a Long-Term Presence on Extraterrestrial Surfaces". In: *Earth and Space 2021*, pp. 855–869. DOI: 10.1061/9780784483374.079. eprint: https://ascelibrary.org/doi/pdf/10.1061/9780784483374.079. URL: https://ascelibrary.org/doi/abs/10.1061/9780784483374.079.

Good, A. and A. Johnson (2021). "NASA InSight's 'Mole' Ends Its Journey on Mars". In: *NASA*.

Grady, D.E. and M.E. Kipp (1979). "The micromechanics of impact fracture of rock". In: *International Journal of Rock Mechanics and Mining Sciences and Geomechanics Abstracts* 16.5, pp. 293–302. ISSN: 0148-9062. DOI: https://doi.org/10.1016/0148-9062(79)90240-7. URL: http://www.sciencedirect.com/science/article/pii/0148906279902407.

Guo, Yonggui and Julia K. Morgan (2008). "Fault gouge evolution and its dependence on normal stress and rock strength: Results of discrete element simulations: Gouge zone micromechanics". In: *Journal of Geophysical Research: Solid Earth* 113.B8. DOI: 10.1029/2006jb004525. eprint: https://agupubs.onlinelibrary.wiley.com/doi/pdf/10.1029/2006JB004525. URL:

https://agupubs.onlinelibrary.wiley.com/doi/abs/10.1029/2006JB004525.

Guo, Yu and Jennifer Sinclair Curtis (2015). "Discrete Element Method Simulations for Complex Granular Flows". In: *Annual Review of Fluid Mechanics* 47.1, pp. 21–46. DOI: 10.1146/annurev-fluid-010814-014644. eprint: https://doi.org/10.1146/annurev-fluid-010814-014644. URL: https://doi.org/10.1146/annurev-fluid-010814-014644.

Harmon, John M., Daniel Arthur, and José E. Andrade (2020). "Level set splitting in DEM for modeling breakage mechanics". In: *Computer Methods in Applied Mechanics and Engineering* 365, p. 112961. ISSN: 0045-7825. DOI: https://doi.org/10.1016/j.cma.2020.112961. URL: http://www.sciencedirect.com/science/article/pii/S0045782520301444.

Harmon, John M. et al. (2021). "Modeling connected granular media: Particle bonding within the level set discrete element method". In: *Computer Methods in Applied Mechanics and Engineering* 373, p. 113486. ISSN: 0045-7825. DOI: 10.1016/j.cma.2020.113486.

Heiken, Grant H., David T. Vaniman, and Bevan M. French (1991). *Lunar Sourcebook, A User's Guide to the Moon*.

Herbst, John A and Alexander V Potapov (2004). "Making a Discrete Grain Breakage model practical for comminution equipment performance simulation". In: *Powder Technology* 143-144, pp. 144–150. ISSN: 0032-5910. DOI: https://doi.org/10.1016/j.powtec.2004.04.036. URL: http://www.sciencedirect.com/science/article/pii/S0032591004001639.

Hobbs, P. V. and B. J. Mason (1964). "The sintering and adhesion of Ice". In: *The Philosophical Magazine: A Journal of Theoretical Experimental and Applied Physics* 9.98, pp. 181–197. DOI: 10.1080/14786436408229184. eprint: https://doi.org/10.1080/14786436408229184. URL: https://doi.org/10.1080/14786436408229184.

Holtz, R.D. and W.D. Kovacs (1981). *An Introduction to Geotechnical Engineering*. Prentice-Hall civil engineering and engineering mechanics series. Prentice-Hall. ISBN: 9780134843940. URL: https://books.google.com/books?id=s%5C_ZRAAAAMAAJ.

Howell, Samuel et al. (2020). "Ocean Worlds Exploration and the Search for Life". In:

Hurley, R. C. et al. (2018). "In situ grain fracture mechanics during uniaxial compaction of granular solids". In: *Journal of the Mechanics and Physics of Solids* 112, pp. 273–290. ISSN: 0022-5096. DOI: https://doi.org/10.1016/j.jmps.2017.12.007. URL: http://www.sciencedirect.com/science/article/pii/S0022509617308967.

Ida, Yoshiaki (1972). "Cohesive force across the tip of a longitudinal-shear crack and Griffith's specific surface energy". In: *Journal of Geophysical Research (1896-1977)* 77.20, pp. 3796–3805. DOI: 10.1029/JB077i020p03796. eprint: https://agupubs.onlinelibrary.wiley.com/doi/pdf/10.1029/JB077i020p03796. URL: https://agupubs.onlinelibrary.wiley.com/doi/abs/10.1029/JB077i020p03796.

Ikari, Matt J. and Achim J. Kopf (2017). "Seismic potential of weak, near-surface faults revealed at plate tectonic slip rates". In: *Science Advances* 3.11. DOI: 10.1126/sciadv.1701269. eprint: https://advances.sciencemag.org/content/3/11/e1701269.full.pdf. URL: https://advances.sciencemag.org/content/3/11/e1701269.

Iliev, Pavel, Falk Wittel, and Hans J. Herrmann (2019). "Evolution of fragment size distributions from the crushing of granular materials". In: *Physical Review E* 99. DOI: 10.1103/PhysRevE.99.012904.

Imseeh, Wadi H. and Khalid A. Alshibli (2018). "3D finite element modelling of force transmission and particle fracture of sand". In: *Computers and Geotechnics* 94, pp. 184–195. ISSN: 0266-352x. DOI: https://doi.org/10.1016/j.compgeo.2017.09.008. URL: http://www.sciencedirect.com/science/article/pii/S0266352X17302537.

Jean, M. (1999). "The non-smooth contact dynamics method". In: *Computer Methods in Applied Mechanics and Engineering* 177.3, pp. 235–257. ISSN: 0045-7825. DOI: https://doi.org/10.1016/S0045-7825(98)00383-1. URL: http://www.sciencedirect.com/science/article/pii/S0045782598003831.

Jiang, Yupeng, Hans J. Herrmann, and Fernando Alonso-Marroquin (2019). "A boundary-spherogon element method for modelling sub-particle stress and particle breakage". In: *Computers and Geotechnics* 113, p. 103087. ISSN: 0266-352x. DOI: https://doi.org/10.1016/j.compgeo.2019.05.002.

Jiménez-Herrera, Narcés, Gabriel K.P. Barrios, and Luis Marcelo Tavares (2018). "Comparison of breakage models in DEM in simulating impact on particle beds". In: *Advanced Powder Technology* 29.3, pp. 692–706. ISSN: 0921-8831. DOI: https://doi.org/10.1016/j.apt.2017.12.006. URL: http://www.sciencedirect.com/science/article/pii/S0921883117305009.

Johansson, Marcus et al. (2017). "A fundamental model of an industrial-scale jaw crusher". In: *Minerals Engineering* 105, pp. 69–78. ISSN: 0892-6875. DOI: https://doi.org/10.1016/j.mineng.2017.01.012. URL: http://www.sciencedirect.com/science/article/pii/S0892687517300249.

Johnson, K. L. (1985). *Contact Mechanics*. Cambridge University Press. DOI: 10.1017/cbo9781139171731.

Johnson, Kenneth Langstreth and Kenneth Langstreth Johnson (1987). *Contact mechanics*. Cambridge university press.

Karapiperis, Konstantinos, Jason P. Marshall, and José E. Andrade (2020a). "Reduced Gravity Effects on the Strength of Granular Matter: DEM Simulations versus Experiments". In: *Journal of Geotechnical and Geoenvironmental Engineering* 146.5, p. 06020005. DOI: 10.1061/(asce)gt.1943-5606.0002232. eprint: https://ascelibrary.org/doi/pdf/10.1061/\%28ASCE\%29GT.1943-5606.0002232. URL: https://ascelibrary.org/doi/abs/10.1061/%5C%28ASCE%5C%29GT.1943-5606.0002232.

Karapiperis, Konstantinos et al. (2020b). "Investigating the incremental behavior of granular materials with the level-set discrete element method". In: *Journal of the Mechanics and Physics of Solids* 144, p. 104103. ISSN: 0022-5096. DOI: https://doi.org/10.1016/j.jmps.2020.104103.

Karatza, Zeynep et al. (2019). "Effect of particle morphology and contacts on particle breakage in a granular assembly studied using X-ray tomography". In: *Granular Matter* 21.3, p. 44. ISSN: 1434-7636. DOI: 10.1007/s10035-019-0898-2. URL: https://doi.org/10.1007/s10035-019-0898-2.

Kawamoto, Reid, José Andrade, and Takashi Matsushima (2018a). "A 3-D mechanics-based particle shape index for granular materials". In: *Mechanics Research Communications* 92, pp. 67–73. ISSN: 0093-6413. DOI: https://doi.org/10.1016/j.mechrescom.2018.07.002. URL: http://www.sciencedirect.com/science/article/pii/S0093641318300673.

Kawamoto, Reid et al. (2016). "Level set discrete element method for three-dimensional computations with triaxial case study". In: *Journal of the Mechanics and Physics of Solids* 91, pp. 1–13. ISSN: 0022-5096. DOI: https://doi.org/10.1016/j.jmps.2016.02.021. URL: http://www.sciencedirect.com/science/article/pii/S002250961530154X.

Kawamoto, Reid et al. (2018b). "All you need is shape: Predicting shear banding in sand with LS-DEM". In: *Journal of the Mechanics and Physics of Solids* 111, pp. 375–392. ISSN: 0022-5096. DOI: https://doi.org/10.1016/j.jmps.2017.10.003. URL: http://www.sciencedirect.com/science/article/pii/S0022509617306580.

Kazerani, T and J Zhao (2010). "Micromechanical parameters in bonded particle method for modelling of brittle material failure". In: *International Journal for Numerical and Analytical Methods in Geomechanics* 34.18, pp. 1877–1895. DOI: 10.1002/nag.884.

Keulen, Nynke, Holger Stünitz, and Renée Heilbronner (2008). "Healing microstructures of experimental and natural fault gouge". In: *Journal of Geophysical Research: Solid Earth* 113.B6. DOI: 10.1029/2007jb005039. eprint: https://agupubs.onlinelibrary.wiley.com/doi/pdf/10.1029/2007JB005039. URL: https://agupubs.onlinelibrary.wiley.com/doi/abs/10.1029/2007JB005039.

Kim, Jin-Hwan, J. Alberto Ochoa, and Stephen Whitaker (1987). "Diffusion in anisotropic porous media". In: *Transport in Porous Media* 2.4, pp. 327–356. ISSN: 1573-1634. DOI: 10.1007/bf00136440.

Kuwano, Osamu, Ryosuke Ando, and Takahiro Hatano (2013). "Crossover from negative to positive shear rate dependence in granular friction". In: *Geophysical Research Letters* 40.7, pp. 1295–1299. DOI: 10.1002/grl.50311. eprint: https://agupubs.onlinelibrary.wiley.com/doi/pdf/10.1002/grl.50311. URL: https://agupubs.onlinelibrary.wiley.com/doi/abs/10.1002/grl.50311.

Lemos, José V. (2007). "Discrete Element Modeling of Masonry Structures". In: *International Journal of Architectural Heritage* 1.2, pp. 190–213. DOI: 10.1080/15583050601176868. eprint: https://doi.org/10.1080/15583050601176868. URL: https://doi.org/10.1080/15583050601176868.

Li, Liuchi, Eloise Marteau, and José Andrade (2019). "Capturing the inter-particle force distribution in granular material using LS-DEM". In: *Granular Matter* 21. DOI: 10.1007/s10035-019-0893-7.

Lim, Keng-Wit and José E. Andrade (2014). "Granular element method for three-dimensional discrete element calculations". In: *International Journal for Numerical and Analytical Methods in Geomechanics* 38.2, pp. 167–188. DOI: 10.1002/nag.2203.

Lisjak, A. and G. Grasselli (2014). "A review of discrete modeling techniques for fracturing processes in discontinuous rock masses". In: *Journal of Rock Mechanics and Geotechnical Engineering* 6.4, pp. 301–314. ISSN: 1674-7755. DOI: https://doi.org/10.1016/j.jrmge.2013.12.007. URL: http://www.sciencedirect.com/science/article/pii/S1674775514000213.

M. A. Celigueta S. Latorre, F. Arrufat and E. Oñate (2020). "An accurate nonlocal bonded discrete element method for nonlinear analysis of solids: application to concrete fracture tests." In: *Computational Particle Mechanics* 7, pp. 543–553. DOI: https://doi.org/10.1007/s40571-019-00278-5.

Marone, Chris, C. Barry Raleigh, and C. H. Scholz (1990). "Frictional behavior and constitutive modeling of simulated fault gouge". In: *Journal of Geophysical Research: Solid Earth* 95.B5, pp. 7007–7025. DOI: 10.1029/JB095iB05p07007. eprint: https://agupubs.onlinelibrary.wiley.com/doi/pdf/10.1029/JB095iB05p07007. URL: https://agupubs.onlinelibrary.wiley.com/doi/abs/10.1029/JB095iB05p07007.

Maskery, I. et al. (2017). "Compressive failure modes and energy absorption in additively manufactured double gyroid lattices". In: *Additive Manufacturing* 16, pp. 24–29. ISSN: 2214-8604. DOI: https://doi.org/10.1016/j.addma.2017.04.003. URL: http://www.sciencedirect.com/science/article/pii/S2214860417301203.

McCord, Thomas B. and Francesca Zambon (2019). "The surface composition of Ceres from the Dawn mission". In: *Icarus* 318. The Composition of Ceres, pp. 2–13. ISSN: 0019-1035. DOI: https://doi.org/10.1016/j.icarus.2018.03.004. URL: https://www.sciencedirect.com/science/article/pii/S0019103517303342.

McDowell, G. R. (2002). "On The Yielding And Plastic Compression Of Sand". In: *Soils and Foundations* 42.1, pp. 139–145. DOI: 10.3208/sandf.42.139.

McDowell, G.R. and J.P. de Bono (2013). "On the micro mechanics of one-dimensional normal compression". In: *Géotechnique* 63.11, pp. 895–908. DOI: 10.1680/geot.12.P.041. URL: https://doi.org/10.1680/geot.12.P.041.

McKay, Christopher P. et al. (2014). "Follow the plume: The habitability of enceladus". English (US). In: *Astrobiology* 14.4, pp. 352–355. ISSN: 1531-1074. DOI: 10.1089/ast.2014.1158.

Minh, N.H. and Y.P. Cheng (2013). "A DEM investigation of the effect of particle-size distribution on one-dimensional compression". In: *Géotechnique* 63.1, pp. 44–53. DOI: 10.1680/geot.10.P.058.

Molaro, J. L. et al. (2019). "The Microstructural Evolution of Water Ice in the Solar System Through Sintering". In: *Journal of Geophysical Research: Planets* 124.2. publisher: American Geophysical Union (AGU), pp. 243–277. ISSN: 2169-9100. DOI: 10.1029/2018je005773. URL: http://dx.doi.org/10.1029/2018JE005773.

Mollon, Guilhem and Jidong Zhao (2014). "3D generation of realistic granular samples based on random fields theory and Fourier shape descriptors". In: *Computer Methods in Applied Mechanics and Engineering* 279, pp. 46–65. ISSN: 0045-7825. DOI: https://doi.org/10.1016/j.cma.2014.06.022. URL: http://www.sciencedirect.com/science/article/pii/S0045782514002084.

Morgan, Julia K. (1999). "Numerical simulations of granular shear zones using the distinct element method: 2. Effects of particle size distribution and interparticle friction on mechanical behavior". In: *Journal of Geophysical Research: Solid Earth* 104.B2, pp. 2721–2732. DOI: 10.1029/1998jb900055. eprint: https://agupubs.onlinelibrary.wiley.com/doi/pdf/10.1029/1998JB900055. URL: https://agupubs.onlinelibrary.wiley.com/doi/abs/10.1029/1998JB900055.

– (2004). "Particle Dynamics Simulations of Rate- and State-dependent Frictional Sliding of Granular Fault Gouge". In: *Pure and Applied Geophysics* 161.9, pp. 1877–1891. ISSN: 1420-9136. DOI: 10.1007/s00024-004-2537-y. URL: https://doi.org/10.1007/s00024-004-2537-y.

Morrow, Carolyn A. and James D. Byerlee (1989). "Experimental studies of compaction and dilatancy during frictional sliding on faults containing gouge". In: *Journal of Structural Geology* 11.7. Friction phenomena in rock, pp. 815–825.

ISSN: 0191-8141. DOI: https://doi.org/10.1016/0191-8141(89)90100-4. URL: http://www.sciencedirect.com/science/article/pii/0191814189901004.

Murphy, Kieran A., Karin A. Dahmen, and Heinrich M. Jaeger (2019). "Transforming Mesoscale Granular Plasticity Through Particle Shape". In: *Phys. Rev. X* 9.1. publisher: American Physical Society, p. 011014. DOI: 10.1103/PhysRevX.9.011014.

Nakata, Yukio et al. (2001). "Microscopic Particle Crushing of Sand Subjected to High Pressure One-Dimensional Compression". In: *Soils and Foundations* 41.1, pp. 69–82. DOI: 10.3208/sandf.41.69.

Nitka, M and J Tejchman (2015). "Modelling of concrete behaviour in uniaxial compression and tension with DEM". In: *Granular Matter* 17.1, pp. 145–164. DOI: 10.1007/s10035-015-0546-4.

Osher, Stanley and Ronald Fedkiw (2006). *Level Set Methods and Dynamic Implicit Surfaces*. Springer Science & Business Media. ISBN: 978-0-387-22746-7. URL: https://play.google.com/store/books/details?id=i4bfBwAAQBAJ.

Portela, Carlos M. et al. (2020). "Extreme mechanical resilience of self-assembled nanolabyrinthine materials". In: *Proceedings of the National Academy of Sciences* 117.11, pp. 5686–5693. ISSN: 0027-8424. DOI: 10.1073/pnas.1916817117. eprint: https://www.pnas.org/content/117/11/5686.full.pdf. URL: https://www.pnas.org/content/117/11/5686.

Postberg, Frank et al. (2018). "Macromolecular organic compounds from the depths of Enceladus". In: *Nature* 558.7711, pp. 564–568. ISSN: 0028-0836. DOI: 10.1038/s41586-018-0246-4.

Potapov, Alexander and Charles Campbell (1996). "a Three-Dimensional Simulation of Brittle Solid Fracture". In: *International Journal of Modern Physics C* 7, pp. 717–729. DOI: 10.1142/s0129183196000594.

Potyondy, D.O. and P.A. Cundall (2004). "A bonded-particle model for rock". In: *International Journal of Rock Mechanics and Mining Sciences* 41.8. Rock Mechanics Results from the Underground Research Laboratory, Canada, pp. 1329–1364. ISSN: 1365-1609. DOI: https://doi.org/10.1016/j.ijrmms.2004.09.011. URL: http://www.sciencedirect.com/science/article/pii/S1365160904002874.

Regnet, J.B. et al. (2019). "Microstructures and physical properties in carbonate rocks: A comprehensive review". In: *Marine and Petroleum Geology* 103. DOI: 10.1016/j.marpetgeo.2019.02.022.

Reynolds, Osborne (1883). "XXIX. An experimental investigation of the circumstances which determine whether the motion of water shall be direct or sinuous, and of the law of resistance in parallel channels". In: *Philosophical Transactions of the Royal Society of London* 174. publisher: Royal Society, pp. 935–982. DOI: 10.1098/rstl.1883.0029.

Riccobono, Dario et al. (2021). "Granular Flow Characterization during Sampling Operation for Enceladus Surface Acquisition". In: *Earth and Space 2021*, pp. 564–576. DOI: 10.1061/9780784483374.053. eprint: https://ascelibrary.org/doi/pdf/10.1061/9780784483374.053. URL: https://ascelibrary.org/doi/abs/10.1061/9780784483374.053.

Rivers, Mark L. (2012). "tomoRecon: High-speed tomography reconstruction on workstations using multi-threading". In: ed. by Stuart R. Stock. Vol. 8506. Backup Publisher: International Society for Optics and Photonics. Spie, pp. 169–181. DOI: 10.1117/12.930022. URL: https://doi.org/10.1117/12.930022.

– (2016). "High-speed tomography using pink beam at GeoSoilEnviroCARS." In: vol. 9967. Backup Publisher: International Society for Optics and Photonics. Spie.

Rubino V., Rosakis A.J. and N. Lapusta (2017). "Understanding dynamic friction through spontaneously evolving laboratory earthquakes". In: *Nature Communications* 8.1. DOI: 1038/ncomms15991. URL: https://doi.org/10.1038/ncomms15991.

Ruina, Andy (1983). "Slip instability and state variable friction laws". In: *Journal of Geophysical Research: Solid Earth* 88.B12, pp. 10359–10370. DOI: 10.1029/JB088iB12p10359. eprint: https://agupubs.onlinelibrary.wiley.com/doi/pdf/10.1029/JB088iB12p10359. URL: https://agupubs.onlinelibrary.wiley.com/doi/abs/10.1029/JB088iB12p10359.

Sapozhnikov, Oleg A. et al. (2007). "A mechanistic analysis of stone fracture in lithotripsy". In: *The Journal of the Acoustical Society of America* 121.2, pp. 1190–1202. DOI: 10.1121/1.2404894.

Schenk, Paul M. and William B. McKinnon (2009). "One-hundred-km-scale basins on Enceladus: Evidence for an active ice shell". In: *Geophysical Research Letters* 36.16. DOI: https://doi.org/10.1029/2009GL039916. eprint: https://agupubs.onlinelibrary.wiley.com/doi/pdf/10.1029/2009GL039916. URL: https://agupubs.onlinelibrary.wiley.com/doi/abs/10.1029/2009GL039916.

Scholz, Christopher H. (1987). "Wear and gouge formation in brittle faulting". In: *Geology* 15.6, pp. 493–495. ISSN: 0091-7613. DOI: 10.1130/0091-7613(1987)15<493:wagfib>2.0.co;2. eprint: https://pubs.geoscienceworld.org/geology/article-pdf/15/6/493/3509770/i0091-7613-15-6-493.pdf. URL: https://doi.org/10.1130/0091-7613(1987)15%3C493:WAGFIB%3E2.0.CO;2.

Scholz, Christopher, Peter Molnar, and Tracy Johnson (1972). "Detailed studies of frictional sliding of granite and implications for the earthquake mechanism". In: *Journal of Geophysical Research (1896-1977)* 77.32, pp. 6392–6406. DOI: 10.1029/JB077i032p06392. eprint: https://agupubs.onlinelibrary.wiley.com/doi/pdf/10.1029/JB077i032p06392. URL: https://agupubs.onlinelibrary.wiley.com/doi/abs/10.1029/JB077i032p06392.

Schulson, Erland M (1999). "The structure and mechanical behavior of ice". In: *Jom* 51, pp. 21–27.

Schulson, Erland M and Andrew L Fortt (2012). "Friction of ice on ice". In: *J. Geophys. Res.* 117.B12. ISSN: 0148-0227. DOI: 10.1029/2012jb009219. URL: http://doi.wiley.com/10.1029/2012JB009219.

Seo, Dawa et al. (2020). "Evolution of particle morphology and mode of fracture during the oedometric compression of sand". In: *Géotechnique* 0.0. _eprint: https://doi.org/10.1680/jgeot.18.P.300, pp. 1–13. DOI: 10.1680/jgeot.18.P.300.

Sethian, J.A. (1999). *Level Set Methods and Fast Marching Methods: Evolving Interfaces in Computational Geometry, Fluid Mechanics, Computer Vision, and Materials Science*. Cambridge Monographs on Applied and Computational Mathematics. Lccn: 98040859. Cambridge University Press. ISBN: 9780521645577. URL: https://books.google.com/books?id=ErpOoynE4dIC.

Smith, S.A.F., S. Nielsen, and G. Di Toro (2015). "Strain localization and the onset of dynamic weakening in calcite fault gouge". In: *Earth and Planetary Science Letters* 413, pp. 25–36. ISSN: 0012-821X. DOI: https://doi.org/10.1016/j.epsl.2014.12.043. URL: http://www.sciencedirect.com/science/article/pii/S0012821X14008048.

Southworth, Ben S., Sascha Kempf, and Joe Spitale (2019). "Surface deposition of the Enceladus plume and the zenith angle of emissions". In: *Icarus* 319, pp. 33–42. ISSN: 0019-1035. DOI: 10.1016/j.icarus.2018.08.024. URL: https://dx.doi.org/10.1016/j.icarus.2018.08.024.

Spitale, Joseph N. and Carolyn C. Porco (2007). "Association of the jets of Enceladus with the warmest regions on its south-polar fractures". In: *Nature* 449.7163, pp. 695–697. DOI: 10.1038/nature06217. URL: https://doi.org/10.1038/nature06217.

Spohn, T. et al. (2018). "The Heat Flow and Physical Properties Package (HP3) for the InSight Mission". In: *Space Science Reviews* 214.5, p. 96. ISSN: 1572-9672. DOI: 10.1007/s11214-018-0531-4.

Suchorzewski, Jan, Jacek Tejchman, and Michał Nitka (2018). "Discrete element method simulations of fracture in concrete under uniaxial compression based on its real internal structure". In: *International Journal of Damage Mechanics* 27.4, pp. 578–607. DOI: 10.1177/1056789517690915.

Sun, Y., B. Indraratna, and S. Nimbalkar (2014). "Three-dimensional characterisation of particle size and shape for ballast". In: *Géotechnique Letters* 4.3, pp. 197–202. DOI: 10.1680/geolett.14.00036. eprint: https://doi.org/10.1680/geolett.14.00036. URL: https://doi.org/10.1680/geolett.14.00036.

Sussman, Mark, Peter Smereka, and Stanley Osher (1994). "A Level Set Approach for Computing Solutions to Incompressible Two-Phase Flow". In: *Journal of Computational Physics* 114.1, pp. 146–159. ISSN: 0021-9991. DOI: https://doi.org/10.1006/jcph.1994.1155. URL: http://www.sciencedirect.com/science/article/pii/S0021999184711557.

Takei, Masataka, Osamu Kusakabe, and Taketo Hayashi (2001). "Time-Dependent Behavior of Crushable Materials in One-Dimensional Compression Tests". In: *Soils and Foundations* 41.1, pp. 97–121. DOI: 10.3208/sandf.41.97.

Tsou, Peter et al. (2012). "LIFE: Life Investigation For Enceladus A Sample Return Mission Concept in Search for Evidence of Life." English (US). In: *Astrobiology* 12.8, pp. 730–742. ISSN: 1531-1074. DOI: 10.1089/ast.2011.0813.

Verbiscer, A J et al. (2018). "Surface Properties of Saturn's Icy Moons from Optical Remote Sensing". In: *Enceladus and the Icy Moons of Saturn*. DOI: 10.2458/azu_uapress_9780816537075-ch016. URL: http://dx.doi.org/10.2458/azu%5C_uapress%5C_9780816537075-ch016.

Vlahinić, Ivan et al. (2014). "Towards a more accurate characterization of granular media: extracting quantitative descriptors from tomographic images". In: *Granular Matter* 16.1, 9–21".

Wadell, Hakon (1932). "Volume, Shape, and Roundness of Rock Particles". In: *The Journal of Geology* 40.5, pp. 443–451. ISSN: 00221376, 15375269. URL: http://www.jstor.org/stable/30058012.

Walton, O.R. and R.L. Braun (1993). "Simulation of rotary-drum and repose tests for frictional spheres and rigid sphere clusters". In: *joint Department of Energy/National Science Foundation (DOE/NSF) workshop on flow of particulates*.

Wang, Jianfeng and Haibin Yan (2013). "On the role of particle breakage in the shear failure behavior of granular soils by DEM". In: *International Journal for Numerical and Analytical Methods in Geomechanics* 37.8, pp. 832–854. DOI: 10.1002/nag.1124. eprint: https://onlinelibrary.wiley.com/doi/pdf/10.1002/nag.1124. URL: https://onlinelibrary.wiley.com/doi/abs/10.1002/nag.1124.

Wang, L. B., J. D. Frost, and J. S. Lai (2004). "Three-Dimensional Digital Representation of Granular Material Microstructure from X-Ray Tomography Imaging". In: *Journal of Computing in Civil Engineering* 18.1, pp. 28–35. DOI: 10.1061/(asce)0887-3801(2004)18:1(28).

Wang, Zhijie et al. (2014). "A new suggestion for determining 2D porosities in DEM studies". In: *Geomechanics and Engineering* 7, pp. 665–678. DOI: 10.12989/gae.2014.7.6.665.

Weerasekara, N.S. et al. (2013). "The contribution of DEM to the science of comminution". In: *Powder Technology* 248. Discrete Element Modelling, pp. 3–24. ISSN: 0032-5910. DOI: https://doi.org/10.1016/j.powtec.2013.05.

032. URL: http://www.sciencedirect.com/science/article/pii/S0032591013003902.

Weibull, W. (1939). *A Statistical Theory of the Strength of Materials*. Handlingar / Ingeniörsvetenskapsakademien. LCCN: ac39002528. Generalstabens litografiska anstalts förlag. URL: https://books.google.com/books?id=otVRAQAAIAAJ.

Witze, A. (2021). "Why NASA's Mars rover failed to collect its first rock core". In: *Nature*. DOI: https://doi.org/10.1038/d41586-021-02208-z.

Xiang, Zhaowei et al. (2016). "Simulation of Forming Process of Powder Bed for Additive Manufacturing". In: *Journal of Manufacturing Science and Engineering* 138.8. DOI: 10.1115/1.4032970. URL: http://dx.doi.org/10.1115/1.4032970.

Zhang, Xiao-Ping Steven and Louis Ngai Yuen Wong (2011). "Cracking Processes in Rock-Like Material Containing a Single Flaw Under Uniaxial Compression: A Numerical Study Based on Parallel Bonded-Particle Model Approach". In: *Rock Mechanics and Rock Engineering* 45, pp. 711–737.

Zhang, Yida, Giuseppe Buscarnera, and Itai Einav (2015). "Grain size dependence of yielding in granular soils interpreted using fracture mechanics, breakage mechanics and Weibull statistics". In: *Géotechnique* 66, pp. 1–12. DOI: 10.1680/jgeot.15.P.119.

Zhao, B. et al. (2015). "An investigation of single sand particle fracture using X-ray micro-tomography". In: *Géotechnique* 65.8, pp. 625–641. DOI: 10.1680/geot.4.P.157. URL: https://doi.org/10.1680/geot.4.P.157.

Zhu, Fan and Jidong Zhao (2019). "Modeling continuous grain crushing in granular media: A hybrid peridynamics and physics engine approach". In: *Computer Methods in Applied Mechanics and Engineering* 348, pp. 334–355. DOI: 10.1016/j.cma.2019.01.017.